Mechanistic Descriptions of Calcite Dissolution in Seawater

Thesis by

Holly Ann Barnhart

In Partial Fulfillment of the Requirements for

the degree of

Doctor of Philosophy in Geochemistry



CALIFORNIA INSTITUTE OF TECHNOLOGY

Pasadena, California

2027

Defended August 17, 2026

© 2027

Holly Ann Barnhart

ORCID: 0000-0002-0842-9464

All rights reserved

Acknowledgements

I feel very lucky to have such a beautiful hodge-podge of a community both at Caltech and in Los Angeles. I owe that partly to Jess, who convinced me that calcite dissolution is way more exciting than calcite precipitation and that I should come to Caltech. He has taught me so much about oceanography, geochemistry and (despite my efforts to the contrary) box modelling. More importantly, he helped teach me how to approach problems that feel intractable. I am grateful for the opportunities and support he's provided throughout my PhD.

He also brings together a hell of a group. Frankie and Grace were the best officemates a girl could ask for. There's no one I'd rather sit next to all day than Grace, even if it means frequent breaks to gab. I learned so much from Frankie. In particular, that it's okay to eat lunch at 10:30am. And a little bit about chemical oceanography. Ted is an all-star scientist and an even better hype-man.

In compiling this thesis I've spent a lot of time thinking about Sijia. Sijia was a thoughtful scientist and funny in the most understated way. I am grateful that I got to overlap with her in my time at Caltech.

I'm also forever grateful that Jess did not purchase a Picarro in my time at Caltech. This meant that I got to spend many hours at USC running the Picarro and generally being ridiculous with the Berelson squad. I can't think of any group I'd rather go to sea with than Jaclyn, Nick, Matt and Rucha. I would like to thank Will for letting me interlope with his group. In the depths of box model hell, he was very helpful at reminding me of the larger scientific questions we were trying to answer.

The Calcarea crew also deserve kudos. Pierre and Melissa were very kind to let me eat all the start-up snacks on the days I visited the Calcarea offices.

Sadie Dutton and Danika Nimlos are two of the first people I met at Caltech and I can't imagine my time here without them. Two of the smartest and kindest women I've ever met and I feel so lucky to call them my friends. Our early morning trail runs/gab sessions are a highlight of my first few years in LA. I feel doubly lucky that their boyfriends, Ham and Dave, are also so wonderful and that I get to count them as friends.

Most of my time in LA has been spent on a bike. If I had to write a second thesis, it would be about the beautiful and wild culture of cycling in Los Angeles. The list of people I've met through bikes that have made my last 5 years in LA so wonderful feels endless. Phil and Elliott are among the most loyal and thoughtful friends I've ever had. Audrey is one of my favorite people to spend hours in the saddle with. Mike, Jacob, Riley, Andy, Guillame and Paul are some of my favorite dudes to rip with. The list goes on. All of these people showed me how beautiful LA is on two wheels.

I have to thank Ethan for feeding me and taking care of all the small things as I pulled together this thesis. I could not have finished this PhD without you. Or maybe I could have, but I would have been hungry. You are my best friend.

My family has been endlessly supportive. Even when they thought that I was going to have to pay tuition to get a PhD. Thank you for everything.

Abstract

Calcium carbonate minerals in the ocean regulate atmospheric CO_2 through carbonate compensation. Excess atmospheric CO_2 taken up by the ocean drives a decrease in pH, promoting the dissolution of carbonate minerals, primarily at the seafloor. Carbonate mineral dissolution increases ocean alkalinity and subsequently rebalances pH, allowing for further CO_2 absorption. This process regulates Earth's climate on glacial-interglacial timescales and is likely important in the modern ocean as anthropogenic emissions drive a rapid increase in atmospheric CO_2.

The canonical timescale for carbonate compensation is roughly 6,000 years and is set largely by ocean circulation, bioturbation and the dissolution kinetics of carbonate minerals. Disagreements about the kinetics of calcite dissolution drive some of the largest uncertainties in the estimate of this timescale. Recent advancements have improved our mechanistic understanding of calcite dissolution kinetics, helping to reconcile disagreements in the field, but the picture is far from complete. In particular, there is debate around the degree of saturation dependence for rates close to equilibrium, where much of the ocean sits. Likewise, processes controlling dissolution rates in marine sediments are poorly understood. From a mechanistic perspective, there has been little work exploring how the major ion composition of any specific species in seawater conspires to set dissolution rates. The work presented here aims to fill these critical gaps in the description of calcite dissolution kinetics.

First, I revisit the experiments of Naviaux et al. (2019), that measured the temperature dependence of calcite dissolution kinetics at very high resolution using an isotope labeling technique. This method has faced criticisms due to its lack of sensitivity in differentiating net rates from gross rates, sometimes termed “isotope exchange”. I reinterpret the Naviaux et al. (2019) dataset using a model, reformulated from Subhas et al. (2019), that explicitly tracks gross dissolution rates and the size of the mineral surface reservoir. I illustrate how the nonlinear signal of dissolution can be parsed into gross dissolution and gross precipitation rates, capturing the “isotope exchange” signal while still producing net dissolution rates. I show that the Naviaux et al. (2019) method for calculating net rates is highly sensitive to the duration of experiments and whether they achieve isotopic steady state. The model also provides insights about the undersaturation dependence of gross rates and the size of the reactive surface reservoir.

Next, I modify the model for application in interpreting novel calcite dissolution experiments performed in situ in marine porewaters. These experiments represent the first direct measurements of calcite dissolution rates in marine sediments. At some sites, 2-10 cm below the sediment water interface, we measured undersaturation values and dissolution rates much higher than predicted from the overlying bottom water. Evidence from chemical profiles of alkalinity, DIC, pH and Mn in the same porewaters suggest that high dissolution rates can be driven by the products of aerobic respiration of organic matter and/or the products of reduced matter oxidation. Both processes lead to a build up of acidic porewater conditions and can drive undersaturation in sediments below their bottom water values. We also note that the porewater dissolution rates close to equilibrium are faster than the rates observed in benchtop experiments. We invoke a previously noted kinetic pressure effect to explain these elevated rates. Regardless of offset, the porewater dissolution rates exhibit a strong, nonlinear dependence on undersaturation that is largely consistent with the behavior of laboratory and water column dissolution experiments.

Finally, I studied the influence of sulfate on the rate of calcite dissolution in seawater. Compared to seawater with modern sulfate concentrations, calcite in sulfate-free seawater dissolves faster at high undersaturations but slower near equilibrium. The change in sign arises from a higher sensitivity to undersaturation far from equilibrium that corresponds to a higher free energy for forming etch pits. In parallel, we interpret the rate behavior in terms of the relative stability of the chemical species formed on the mineral surface. The presence or absence of sulfate modulates the surface stability differently close to and far from equilibrium in a manner consistent with our rate observations.

Published Content and Contributions

Cetiner, J.E.P., Berelson, W.M., Rollins, N.E., Barnhart, H.A., Liu, X., Dong, S., Byrne, R.H., Adkins, J.F., 2023. Novel device to collect deep-sea porewater in situ: A focus on benthic carbonate chemistry. Limnology & Ocean Methods 21, 82–97. https://doi.org/10.1002/lom3.10530

H.A.B. assisted in testing equipment and design considerations.

Cetiner, J.E.P., Berelson, W.M., Rollins, N.E., Liu, X., Pavia, F.J., Waldeck, A.R., Dong, S., Fleger, K., Barnhart, H.A., Quinan, M., Wani, R.P., Rafter, P.A., Jacobson, A.D., Byrne, R.H., Adkins, J.F., 2025. Carbonate dissolution fluxes in deep-sea sediments as determined from in situ porewater profiles in a transect across the saturation horizon. Geochimica et Cosmochimica Acta 390, 145–159. https://doi.org/10.1016/j.gca.2024.11.027

H.A.B. assisted in instrument deployment, data collection and data interpretation.

Table of Contents

ACKNOWLEDGEMENTS III
ABSTRACT IV
PUBLISHED CONTENT AND CONTRIBUTIONS VI
TABLE OF CONTENTS VII
LIST OF ILLUSTRATIONS IX
LIST OF TABLES XIV

CHAPTER 1. INTRODUCTION: DESCRIPTIONS OF CARBONATE DISSOLUTION, OCEAN ALKALINITY AND GLOBAL CLIMATE 1

CHAPTER 2. GROSS REACTION RATES AND SURFACE REACTIVITY OF CALCITE DURING DISSOLUTION IN SEAWATER: INSIGHTS FROM MODELLING AND ISOTOPE-TRACER EXPERIMENTS 6

1. Introduction 6
2. Methods 7
2.1 Isotope label dissolution experiments 7
2.2 Rate calculation 8
3. Model 9
3.1 Model description 9
3.2 Model initial condition and free parameters 10
3.3 Model equations 10
4. Model sensitivities 11
4.1 Gross and net rates 11
4.2 Reactive surface reservoir 13
4.3 Limitations of the model 14
5. Results 14
5.1 Model fitting 14
5.2 Constraints and limitations on parameter recovery 17
5.3 Undersaturation dependence of model parameters 20
6. Discussion 22
6.1 Isotope exchange considerations 22
6.2 Mechanistic insights into model parameters 23
6.3 Gross and net dissolution rates 27
6.4 Implications 29
7. Conclusions 29

CHAPTER 3. NOVEL MEASUREMENT OF CALCITE DISSOLUTION KINETICS IN MARINE POREWATERS 31

1. Introduction 31
2. Methods 33
2.1 Study site 33
2.2 Dissolution experiments 33
2.3 Measurements 38
2.4 Ω Calculations 38
2.5 Critical undersaturation identification 38
3. Model 39
3.1 Reaction model 39

3.2 Mixing model 41
3.3 Optimization 42
4. Results *43*
4.1 Ω interpolation 43
4.2 Experiment data 44
4.3 Mixing coefficient fits 46
4.4 Reaction model fits 47
5. Discussion *52*
5.1 *In situ* porewater rate law 52
5.2 Surface energetic parameters 57
5.3 Rate magnitude offset 59
5.4 Porewater dissolution profiles 61
5.5 Implications for the calcite lysocline 66
5.6 Implications for ocean alkalinity cycling 66
6. Conclusions *67*

CHAPTER 4. CALCITE DISSOLUTION KINETICS IN SULFATE-FREE SEAWATER 69

1. Introduction *69*
2. Methods *70*
2.1 Dissolution experiments and materials 70
2.2 Rate calculation 72
2.3 Modelling of $\delta^{13}C$ vs time 72
2.4 Ω critical calculation 72
3. Results *73*
3.1 Undersaturation calculations 73
3.2 Influence of sulfate on MarChemSpec Ω 75
3.3 Calcite dissolution rates in sulfate free seawater 76
3.4 Model verification of isotopic steady state 77
4. Discussion *78*
4.1 Rate law for calcite dissolution in sulfate-free seawater 78
4.2 Surface energetics during dissolution 79
4.3 Calcite surface reactivity with and without sulfate 83
4.4 Insights from AFM studies 84
5. Conclusions *86*

CHAPTER 5. CONCLUSIONS AND FUTURE WORK 88

BIBLIOGRAPHY 90

List of Illustrations

Chapter 1. Introduction

1.1 Schematic of the three mechanisms that describe calcite dissolution. (a) Near equilibrium dissolution proceeds via step retreat. (b) At intermediate undersaturations, dissolution proceeds via the formation of etch pits at defects. (c) Far from equilibrium, etch pits may form anywhere on the mineral surface, and dissolution proceeds at these etch pits.

Chapter 2. Gross reaction rates and surface reactivity of calcite during dissolution in seawater: insights from modelling and isotope-labelling experiments

2.1 Example results from the work of Naviaux et al. (2019), shown for experiment B24-B2. The left y-axis and light grey points represent the $\delta^{13}C$ signal in the bulk reservoir over the course of an experiment. The right y-axis and purple points show the "total moles dissolved" over the course of an experiment. The line through a subset of the purple, "moles dissolved" points is a linear regression for data between t = 24 hours and the end of an experiment (in this case ~105 hours), used to calculate the net rate in Naviaux et al (2019).

2.2 Schematic representation of 2-box calcite dissolution model. The shaded blue volume represents the bulk aqueous reservoir in which an experiment is performed. The size of this reservoir changes with time but is held at roughly constant undersaturation. The calcite grains are represented by the cube inside the aqueous reservoir that is subdivided into unit cells. Near the surface of the grain, unit cells may either be reactive (dark grey cubes) or unreactive (light grey cubes). Gross dissolution (1) and gross precipitation (2) are denoted by the dark and light orange arrows, respectively. Net dissolution (3), denoted by the yellow arrow, makes up the difference of the gross dissolution and gross precipitation fluxes such that the size of the reactive reservoir is constant during an experiment.

2.3 Model sensitivity to G_{off} and R for constant net rates. All example models shown here have a net dissolution rate of 10^{-13} mol/cm^2/s and are run under the same conditions, only varying G_{off} and R. The color coding corresponds to the G_{off}, R values noted in the legend. (a) The evolution of aqueous $\delta^{13}C$ as a function of time. (b) The corresponding evolution of the mineral surface (reported as a "fraction of the reactive sites that are ^{13}C") as a function of time.

2.4 Model sensitivity to G_{off} and R at fast net dissolution rates. All example models shown here have a net dissolution rate of 10^{-11} mol/cm^2/s and are run under the same conditions, only varying G_{off} and R. The color coding corresponds to the G_{off}, R values noted in the legend. (a) The evolution of aqueous $\delta^{13}C$ as a function of time. The different models are not discernable on this scale. (b) The corresponding evolution of the mineral surface (reported as a "fraction of the reactive sites that are ^{13}C") as a function of time.

2.5 Model sensitivity to reactive sites, S. All synthetic experiments are run with $G_{off} = 10^{-13}$ mol/cm2/s, R = 0.8. (a) $\delta^{13}C$ vs. time for 10^5 hours. (b) Zoomed in to the first 100hr of the models plotted in (a) to the first 100 hours of the model run. (c) Reactive surface fraction of 13C as a function of time.

2.6 Example model fits for experiment T30-B3 at 21°C, $\Omega = 0.82$. (a) $\delta^{13}C$ of the reactive aqueous reservoir. Measured data are in pink. Error bars on individual measurements are smaller than the size of the points. Grey lines are the model fits, n = 330. The model fits are all

comparable and sit close to each other such that they look like a thick grey line. (b) Model predicted surface isotopic composition as a function of time.

2.7 Histograms for model parameters in fits for the model curves shown in Figure 6. (a) Gross dissolution rate, mol/cm^2/s, (b) ratio of gross precipitation to gross dissolution, (c) reactive surface site density and (d) net dissolution rate.

2.8 Figure 8. Individual parameter fits for the model curves shown in Figure 6. (a) Cross plot of S and G_{off}, (b) cross plot of R and G_{off} and (c) cross plot of R and S. The color coding corresponded to the value of the residual score, shown in the color bar, for each model fit.

2.9 Fits for experiment T1-B1, 21°C, Ω = 0.92. (a) Measured $\delta^{13}C$ data (pink circles) and model predicted $\delta^{13}C$ vs. time (grey lines). (b) Histogram of net rates calculated from G_{off} and R, following Equation 14. (c-d) Cross plots of fitted parameters. Color bar denotes the residual score for each pair of fitted parameters.

2.10 For example, experiment T11-B4, 5°C, Ω = 0.95. (a) Measured $\delta^{13}C$ data (pink circles) and model predicted $\delta^{13}C$ vs. time (grey lines). (b) Surface isotopic composition with time. (c) Histogram of net rates calculated from G_{off} and R, following Equation 14. (d-e) Cross plots of fitted parameters. Color bar denotes the residual score for each pair of fitted parameters.

2.11 Model optimized parameters as a function of undersaturation for 5°C (a, b, c), 12°C (d, e, f), 21°C (g, h, i) and 37°C (j, k, l). Where error bars cannot be seen, they are smaller than the size of the marker.

2.12 Reproduction of Teng (2004) AFM image of a dissolving calcite crystal {1014} surface at (a) Ω = 0.111 and (b) Ω = 0.051. Scalebar of 1um noted in the bottom left.

2.13 The undersaturation dependence of site density (orange diamonds) and etch pit density from the seawater AFM experiments of Dong et al., 2020 (dark grey squares) and the freshwater AFM experiments of Teng, 2004 (light grey circles). The left y-axis corresponds to the magnitude of the site density term, and the right y-axis corresponds to the magnitude of the etch pit density term. The alignment of the two axes does not indicate any particular relationship between site density and etch pit density. The key information here is that the two terms change by comparable orders of magnitude and at similar values of undersaturation.

2.14 Net dissolution and gross dissolution rates for 5°C (a), 12°C (b), 21°C (c) and 37°C (d) as a function of undersaturation. Lighter markers are gross dissolution and darker markers are net dissolution.

Chapter 3. Novel measurement of calcite dissolution kinetics in marine porewaters

3.1 Locations of stations studied along the Cocos Ridge. Station 1 – CR1 blue circle. Station 2 – CR2 orange square. Station 3 – CR3 green triangle. Station 5 – CR5 yellow diamond. The same symbols used to denote the station identities here are consistent throughout the figures in this paper. Colormap denotes water depth.

3.2 Porewater chemistry profiles reproduced from Cetiner et al. 2025. DIC, alkalinity, pH and [Mn2+] for (a-d) CR1, (e-h) CR2 (i-l) CR3 and (m-p) CR5.

3.3 Schematic of a blade deployed at the seafloor and an example of how the sample coil is divided for subsampling. The sediment is denoted by the brown background, and the overlying water is denoted by the light blue background. The blade is shown in dark grey, with nine sampling windows represented in light grey. The sampling windows are positioned at staggered depths below the sediment-water interface. There is internal routing that connects each blade window to a three-way valve, which it connected to the quartz sample coil (example shown for just one blade window/valve/coil). Above the sample coil is another three-way valve, tubing and a syringe (not pictured – see Cetiner et al. 2022, 2025 for details). The blade window collects water from a given depth and the ~2.7cm above and below, shown here as the blue "halo" of collected porewater (not to scale).

3.4 Schematic of the box model for advection and reaction in our experimental system. The calcite grain is represented by the grey cubes, where an individual cube represents a single unit cell of calcite. The reactive sites, those that may participate in gross dissolution and gross precipitation (dark and light orange arrows, respectively), are shown in dark grey unit cells and nonreactive sites shown in light grey. As the reactive sites are removed, new ^{13}C is supplied from the bulk material (yellow arrows). The volume of the whole blade widow is shown as the dashed box. Inside the volume is the reactive aqueous volume. The mineral grains only directly interact with the reactive volume. An advective flux defined by the flow rate in a given experiment passes through both aqueous reservoirs at a constant rate.

3.5 Results of GPR for Ω determination at experiment depths for (a) CR1, (b) CR2, (c) CR3 and (d) CR5. The Ω values calculated from the background porewater chemistry are shown as black dots. The result of the GRP is shown as a solid blue line. There 95% confidence interval is shown as the shaded blue region. Note that regions with large confidence intervals generally correspond to where there is low data density or noisy data.

3.6 For each station, the $\delta^{13}C$ data from all experiments. The a, b, c and d subsamples for a given experiment are represented by points connected by a line. The dashed line at 0 on the x-axis represents the idealized fill-solution/sample interface. The "d" subsample is closest to the fill-solution/sample interface and represents the start of an experiment. The "a" subsample is furthest from the interface and represents the end of an experiment. The color coding denotes the depth in the sediment at which the experiment was performed.

3.7 Fitted mixing coefficients (logD, m^2/s) as a function of experiment flow rate for CR1 (blue circles), CR2 (yellow diamonds), CR3 (red squares) and CR5 (green triangles).

3.8 Example model output for experiment CR214. (a) Measured data for subsamples shown in grey circles. Model fits are purple lines. For this example, there are n=18 model fits that passed our filter for an acceptable fit (see text). (b) Histogram of net rates corresponding to the model fits in (a), calculated following Equation 18. (c-e) Cross plots of individual parameters for the fits presented in (a). The color bar represents the value of the residual score for each model/parameter combination.

3.9 Example model output for experiment CR502. (a) Measured data for subsamples shown in grey circles. Model fits are purple lines. For this example, there are n = 42 model fits that passed our filter for an acceptable fit (see text). (b) Histogram of net rates corresponding to the model fits in (a), calculated following Equation 18. (c-e) Cross plots of individual parameters for the fits presented in (a). The color bar represents the value of the residual score for each model/parameter combination.

3.10 At CR1 (a) normalized $\delta^{13}C$ and (b) modelled net rate depth profiles

3.11 At CR2 (a) normalized $\delta^{13}C$ and (b) modelled net rate depth profiles

3.12 At CR3 (a) normalized $\delta^{13}C$ and (b) modelled net rate depth profiles

3.13 At CR5 (a) normalized $\delta^{13}C$ and (b) modelled net rate depth profiles

3.14 Modelled dissolution rates as a function of 1- Ω. In both panels, the grey diamonds are from the 5°C benchtop study of Naviaux et al. (2019a) and the grey squares are from the water column study of Naviaux et al. (2019b). In (a), CR1 data are blue circles, CR2 are yellow diamonds, CR3 are red squares and CR5 are green triangles. In (b), all *in situ* porewater experiments are shown as blue circles with their respective error bars, compared against the Naviaux et al. (2019a, 2019b) data. The dashed black lines in (b) denotes the fits to the York regressions through the *in situ* data for an Ω_{crit} of 0.85.

3.15 Zoomed in version of rate vs. 1- Ω plot for just CR2 and CR3 experiments. The color bar denotes the normalized $\delta^{13}C$ value of the "a" subsample of each experiment. Higher rates have "hotter" colors, denoting larger steady state $\delta^{13}C$ signals.

3.16 The surface energetic framing of the rate vs. undersaturation. The y-axis is the surface normal dissolution rate as defined in Equation 20. The x-axis is a translation of Ω following Equation 19. The measured data are reported in grey circles for all stations. The black dashed line represents the fit for the homogeneous etch pit regime (Equation 21) and the yellow, curved dashed line represents the fit for step edge retreat (Equation 22).

3.17 Dissolution rates plotted with porewater undersaturations for (a) CR1, (b) CR2, (c) CR3 and (d) CR5. The top x-axis in each panel is the log of the modelled dissolution rate and the bottom x-axis is (1- Ω). The horizontal grey bar donates the depth at which $[Mn^{2+}]$ markedly increase from zero, which we interpret to be the approximate oxygen penetration depth. The dashed vertical line represents Ω = 1. The offset of the top and bottom x-axes are arbitrary and meant to capture the whole range of net rates – it does not to indicate any specific scaling between rate and Ω.

3.18 Alkalinity and DIC pairs from porewater measurements in the top 10cm of the sediment (a) CR1, (b) CR2, (c) CR3 and (d) CR5. One to one lines are denoted by the dashed line. The grey stars in each panel represent the composition of the overlying water at each station. The color coding of the points in each plot corresponds to the depth of each sample below the sediment-water interface.

3.19. Alkalinity and DIC measurements for porewater samples for 0 to 35cm sediment depth for CR1 (blue circles), CR2 (yellow diamonds), CR3 (red squats) and CR5 (green triangles). The 1:1 line is denoted as a dashed line.

Chapter 4. Calcite dissolution kinetics in sulfate-free seawater

4.1 Comparison of CO2SYS and MarChemSpec models for pH (a,b), carbonate ion concentration (c,d) and saturation state (e,f). All test solutions were assigned a temperature of 21C and atmospheric pressure. Calcium concentration is 9.78 mmol/kg-SW in both models. Salinity is 33.275 +/- 0.005 for both models.

4.2 Summary of MCS carbon system parameters sensitivity to sulfate concentration. (A) pKa2 as a function of the % sulfate in solution. (B) The difference between modern seawater (MSW) pH and artificial seawater (ASW) pH, where the % sulfate of the artificial seawater varies between 0.1% and 100%. Cooler colors represent lower amounts of sulfate. (C) The difference in carbonate ion between MSW and ASW. (D) The difference in Ω between MSW and ASW. All panels are shown as a function of their respective value in MSW .

4.3 Net dissolution rate of labeled calcite grains in Dickson seawater (grey circles) and artificial seawater with $[SO_4^{2-}] = 0$ (blue triangles), both at 21°C. The Ω values for both seawater datasets are calculated using MarChemSpec.

4.4 Net dissolution rate comparison between the model approach (light blue) and the regression approach (dark blue). Good agreement indicates that the linear regression approach to calculating net rates was applied after the mineral surface achieved isotopic steady state.

4.5 Identification of Ω_{crit} and York fits to data for ASW with $[SO_4^{2-}] = 0$, with Ω values calculated in MarChemSpec. $\Omega_{crit} = 0.8 \pm 0.05$.

4.6 Dissolution rates and undersaturations recast in the Dove framework for (a) sulfate free and (b) Dickson seawater experiments. In (a) the light blue triangles are the data used to fit alpha and beta in the step-retreat formulation – Equation 5. For all other regressions, the slopes and intercepts are reported in Table 3.

List of Tables

Chapter 2
2.1 Ω_{crit} values for modelled net rates and individual parameters.

Chapter 3
3.1 Location, physical and chemical description of SIPR stations

3.2 . Summary of Ω_{crit}, rate law constant and reaction order for the benchtop experiments of Naviaux et al. (2019a), the water column experiments of Naviaux et al. (2019b) and this study.

3.3 Surface energetic parameters derived from Equations 21-24 for the benchtop experiments of Naviaux et al. (2019a), the water column experiments of Naviaux et al. (2019b) and this study.

Chapter 4
4.1 Concentrations (mol/kg) of species in Morel et al. (1979) sweater recipe, estimates for Dickson seawater and estimates for Aquil solutions used in experiments (calcium corrected, see text).
4.2 Correction factors for Aquil batches, denoted as percent concentrations relative to the JN-Aquil solution.

4.3 York fit parameters for sulfate free experiments, Dickson seawater experiments at 21C determined using MarChemSpec Ω values and with CO2SYS Ω values.

4.4 Summary of calculated surface energetic parameters for sulfate-free seawater (this study), Dickson seawater at 21ºC and 5ºC (from Naviaux et al. 2019a, with omega values recalculated in MarChemSpec).
4.4 Description of surface binding reactions and their respective binding constants for the surface complexation models of Van Capellen et al. (1993), Pokrovsky and Schott (2002) and Ding and Rhaman (2018).

4.5 Subset of the results from the AFM study by Ruiz-Agudo et al. (2019). Calcite was exposed to very undersaturated water with varying concentrations of the following salts. We select the experiments performed ~50mM +/- 5mM for a given salt – the approximate concentration and approaching the IS of seawater.

Chapter 1. Introduction: Descriptions of carbonate dissolution, ocean alkalinity and global climate

The rate of calcite ($CaCO_3$) dissolution is driven primarily by the saturation state, defined as Ω following:

Eq. 1) $\Omega = [Ca^{2+}][CO_3^{2-}]/K_{sp}$

where $[Ca^{2+}]$ and $[CO_3^{2-}]$ represent the total concentrations of dissolved calcium and carbonate ion and K_{sp} is the thermodynamically defined solubility product. For a solution where $\Omega > 1$, calcite is thermodynamically stable and where Ω is < 1, calcite is thermodynamically unstable and will tend to dissolve. In the ocean, the saturation stat of calcite is primarily driven by the solubility product. The K_{sp} is a strong function of pressure and, to a lesser degree, temperature (F. Millero, 1979). As pressure increases, the K_{sp} increases, driving greater undersaturation even for constant $[Ca^{2+}]$ and $[CO_3^{2-}]$.

This behavior allows for the definition of three relevant oceanography depth distinctions: the saturation horizon, carbonate compensation depth and the calcite lysocline. The saturation horizon is the depth in ocean at which seawater is in chemical equilibrium with calcite, $\Omega = 1$. The carbonate compensation depth (CCD) is where the rate of carbonate supply is matched with the rate of carbonate dissolution in the sediments. The CCD is commonly defined operationally (rather than based on seawater thermodynamics) as the depth at which the carbonate content of sediments reaches 0%. The calcite lysocline, also operationally defined, is the depth range over which the carbonate content of sediments experiences a sharp decrease.

In general, but not exclusively, the saturation horizon sits near the upper bound of the lysocline, and the CCD sits at its lower bound. The decoupling of these depth horizons is largely driven by the slow kinetics of calcite dissolution relative to the supply of carbonate to the sediments. In other words, carbonate minerals do not disappear from sediments instantaneously when Ω drops below 1. In the context of a constant source of carbonate to the sediments, the presence of a sedimentary lysocline indicates that the rate of dissolution must dramatically increase.

Indeed, in the seminal calcite dissolution experiments of Peterson (1966) and later Berger (1967) a marked increase in the rate of calcite dissolution was noted from water column dissolution experiments at depths corresponding to the sediment lysocline rather than the crossing of the saturation. In other words, there is a nonlinear response of the dissolution rate to the thermodynamic driving force in solution, Ω.

Subsequent studies of calcite dissolution in seawater both in the lab and in natural waters, frame this nonlinear dependence as the rate law in Equation 2:

Eq. 2) $\text{rate} = k(1 - \Omega)^n$

where k is a kinetic coefficient (often in $mol/cm^2/s$) and n is a unitless reaction order that describes the undersaturation dependence of the rate. However, reported values of k and n derived from different experimental and field studies can vary by orders of magnitude (Archer et al., 1998; Berelson et al., 1994; Hales and Emerson, 1997; Keir, 1980; Walter and Morse, 1985). Reaction orders for calcite dissolution in seawater alone have been reported to span the range

from near-zero to greater than 4.5, a range too wide to reflect measurement uncertainties alone. The empirical nature of the rate law in Equation 2 and the variability in how it is fit by different authors illustrates the necessity of a mechanistic description of calcite dissolution kinetics in seawater.

To robustly define the relationship between calcite dissolution and undersaturation (in particular near equilibrium where much of the water column and porewaters sit) whatever experimental approach is employed must be sensitive to even very slow dissolution rates. Historically, calcite dissolution experiments have been performed by tracking changes in bulk solution chemistry, i.e. how [Ca^{2+}], alkalinity or pH change as calcite dissolves (Keir, 1980; Morse, 1978). Subhas et al. (2015) developed an isotope tracer method for calcite dissolution in seawater that increased their sensitivity over 200 times that of the best constrained alkalinity experiments and 20 times that of well controlled pH approaches (Morse, 1978). The method consists of dissolving pure $Ca^{13}CO_3$ grains into seawater of constant undersaturation in well-mixed, airtight reservoirs. Subsequently, Dong et al. (2018) and Naviaux et al. (2019) employed this method to explore the influence of temperature and pressure on calcite dissolution in seawater.

The body of work produced by Subhas et al. (2015, 2017), Naviaux et al. (2019a, 2019b) and Dong et al. (2018, 2020), summarized in Adkins et al. (2021), established a mechanistic description of calcite dissolution rates in seawater. Across all of these studies, that rate of calcite dissolution can be described in terms of three surface energetic mechanisms that exert varying degrees of control on the dissolution rate as a function of undersaturation (Figure 1). All three mechanisms are defined by the propagation of relatively unstable topographic “steps” on the mineral surface, and they differ in the source of the steps.

Near equilibrium, dissolution proceeds only at steps that are inherent to the mineral surface (Figure 1a). This may include crystal edges and screw dislocations. Further from equilibrium, as the thermodynamic driving force in solution increases, new steps may be sourced from defects on the mineral surface (Figure 1b). As the thermodynamic driving force increases even further, new steps can be sources effectively anywhere on the mineral surface.

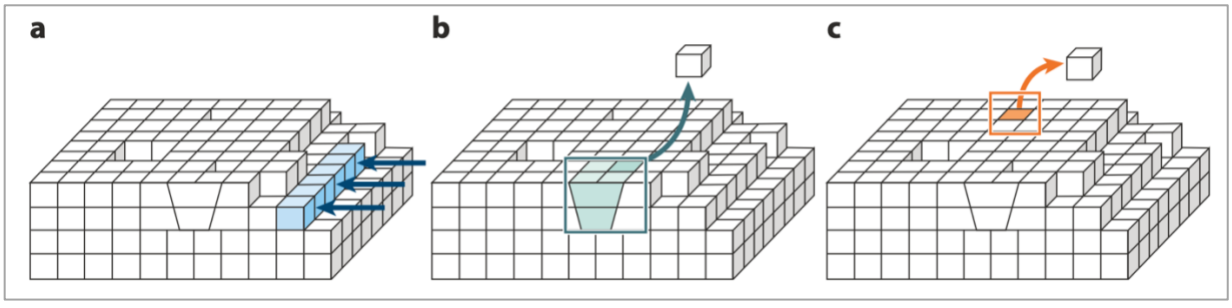


Figure 1. Schematic of the three mechanisms that describe calcite dissolution. (a) Near equilibrium dissolution proceeds via step retreat. (b) At intermediate undersaturations, dissolution proceeds via the formation of etch pits at defects. (c) Far from equilibrium, etch pits may form anywhere on the mineral surface, and dissolution proceeds at these etch pits.

Using this framework to describe three distinct regimes of dissolution rate gives rise to three separate fits of k and n in the classical rate law. In effect, this illustrates why estimates of k and n have been so variable in the literature: they are, themselves, functions of undersaturation. Studies that produce high order rate law, do, in fact, capture the undersaturation dependence but only in the far from equilibrium range. It is simultaneously true that the dissolution rate exhibits a lower

order rate when close to equilibrium. This body of work reflects a significant advancement in the description of, and mechanistic basis for, calcite dissolution rates in seawater.

Among the opportunities to further advance this body of work are a more complete utilization of the d13C data collected in any individual experiments. The isotope-label method is uniquely positioned to capture information about the gross rates of dissolution that set the overall net rate. As pure ^{13}C grains dissolve into essentially pure ^{12}C water, gross precipitation fluxes can move ^{12}C from solution to the mineral surface, changing the surface composition so that it is no longer pure ^{13}C. This process can happen even under the condition of net dissolution. The result is a nonlinear $\delta^{13}C$ signal with time during a dissolution experiment.

Most of the studies above quantify just the net dissolution rates and exclude the non-steady state signal in the early part their experiments. Subhas et al. (2017) presents a simplified treatment of the non-steady state data from the original set of Subhas et al. (2015) experiments. In Chapter 2, the Subhas et al. (2017) model is reformulated and used with the Naviaux et al. (2019a) dataset to quantify gross dissolution rates and the reactivity of the mineral surface as a function of temperature.

We also address a recurring criticism of the isotope-label method for quantifying dissolution rates: that the isotope signal interpreted as a net rate is capturing isotope exchange. By parsing the net rate into explicit gross fluxes, the model successfully captures the evolution of the mineral surface towards steady state and recovers the same net rates values as those reported by Subhas et al. and others with a key exception. When very close to equilibrium and at low temperatures (5C), the experiments run by Naviaux et al did not achieve isotopic steady state and the true net rates are lower than previously reported. This results in a reaction order near equilibrium that is more consistent with other observations in the field.

The model provides an essential correction and contribution to laboratory studies, but the application of these and other benchtop dissolution rates to natural environments has been the subject of debate. Naviaux et al. (2019b) found that the mechanistic description applied to dissolution in laboratory experiments could be translated to dissolution in the water column and in Chapter 3, we show that the same is true for marine porewaters.

We performed the first direct measurements of calcite dissolution rates in marine sediments using the isotope-label approach. In order to interpret the results the model from Chapter 2 was reformulated to match the conditions of these experiments. We found elevated dissolution rates in the 2-10cm below the sediment water interface, well above the values predicted by bottom water Ω. The chemical profiles in the sediments suggest that the elevated dissolution is due to the buildup of respiration products and/or the products of reduced matter oxidation that both lead to acidic porewater conditions and drive dissolution.

In comparing across environments, we note that the dissolution rates close to equilibrium are faster than observed in benchtop experiments, which is the possible result of a previously noted kinetic pressure effect on dissolution rates. Additionally, the porewater rates follow a rate law of similar form as bench and water column experiments with roughly the same critical undersaturation. The surface energetic framework used to explain the rate behavior in the laboratory and in the water column is therefore, also applicable at the seafloor.

With dissolution in the sediments explicitly considered, a natural next frontier to explore is how the chemistry of seawater itself influences the rate and mechanisms of calcite dissolution. In fact, the potential importance of this question arose in our porewater study: the dissolution behavior in

anoxic, high Mn^{2+} porewaters appeared faster than we would have predicted from the Ω values in those experiments. It is unclear if this behavior is the result of solution speciation changes shifting Ω values or kinetic effects altering dissolution rates. This points to a larger question about how the speciation of seawater influence dissolution rates.

We can use the tools commonly employed in the freshwater community to explore the role of individual dissolved species on calcite dissolution rates. Where the oceanographic community has struggled to agree on an empirical rate law, the freshwater community has found success in describing calcite dissolution mechanistically in terms of elementary chemical reactions controlling dissolution (Plummer et al., 1978). Arakaki and Mucci (1995) combined the surface speciation model of Van Cappellen et al. (1993) and the reactions of Plummer et al. (1978) into Equations 3-6. Together, these equations describe the elementary reactions of calcite dissolution with respect to the chemical speciation of the mineral surface.

Eq. 3) $> CO_3^- + 2H^+ \leftrightarrow > Ca^{2+} + H_2CO_3$ k_1, k_5

Eq. 4) $> Ca^+ + H_2CO_3 \leftrightarrow > CO_3\,H + CaHCO_3^+$ k_2, k_6

Eq. 5) $> CO_3H + CaHCO_3^+ \leftrightarrow > Ca^{2+} + H_2CO_3 + CaCO_3$ k_3, k_7

Eq. 6) $CaCO_{3,solid} \leftrightarrow CaCO_3^0$ k_4, k_8

Here $>i$ denotes a species associated with the mineral surface, "surface complexes". The k values represent the forward and backward rate constants, respectively, for each reaction. Overall, a rate equation can be defined following Equation 7. Arakaki and Mucci (1995) were able to capture the dissolution rate of calcite for in freshwater over a range of pH's using this formulation.

Eq. 7) $$Rate = k_1 > CO_3^-\{H^+\}^2 + (k_2 - k_5) > Ca^+\{H_2CO_3^*\} + k_4 - (k_6 - k_3) > CO_3H\{CaHCO_3^+\} - k_7 > Ca^+\{H_2CO_3^*\} - k_8\{CaCO_3^0\}$$

The translation of this approach for describing dissolution in seawater is nontrivial. The high ionic strength and complex nature of seawater mean that a full characterization of the interactions among species that allow for the calculation of [Ca], [CO3] and subsequently, Ω, is nontrivial. For typical seawater compositions the parameters required to calculated Ω have been defined empirically. This forms the basis of the widely used CO2SYS program (Lewis et al., 1998). Recently, Humphreys et al. (2022) developed a well calibrated model that uses the Pitzer framework to perform speciation calculations in seawater. With this advancement, the field is much better equipped to explore how changes to the major ion chemistry of seawater influence calcite dissolution rates.

In Chapter 4, the role of aqueous speciation is explored by changing the sulfate concentration of seawater in our dissolution experiments. Compared to seawater with modern sulfate concentrations, sulfate-free seawater dissolves faster at high undersaturations, but slower near equilibrium. This behavior can be cast in the surface energetic framework to describe changes to surface parameters as a function of undersaturation. We find that the transition in sign relative to the rate of dissolution in seawater with modern sulfate concentrations is the result of a higher thermodynamic barrier for the homogenous formation of etch pits. Likewise, we invoke the stability of specific calcite surface sites can be used to describe the differences in rate relative to modern seawater solutions close to and far from equilibrium.

Overall, the work in this dissertation represents an extension of bulk rate measurements and surface energetic descriptions of calcite dissolution. The model in Chapter 2 considers how gross

fluxes conspire to set net rates within defined mechanistic regimes and provides an undersaturation dependent description of surface reactivity independent and in validation of Dove et al. (2005) framework. In Chapter 3, we quantified dissolution rates in porewaters in novel dissolution experiments. We observed meaningful decoupling of porewater rates from the undersaturation of the bottom water with the implication that marine sediments can recycle alkalinity on rapid timescales. In Chapter 4 we draw on concepts from both surface energetics and surface complexation to describe the response of calcite dissolution to changing seawater sulfate concentrations.

Chapter 2. Gross reaction rates and surface reactivity of calcite during dissolution in seawater: insights from modelling and isotope-tracer experiments

1. Introduction

Carbonates are among the most abundant and reactive minerals at Earth's surface. Their dissolution and precipitation reactions govern some of the most consequential fluxes in the global carbon and alkalinity cycles. The weathering of carbonate rocks on land and the dissolution of biogenic carbonate on the seafloor buffer against changes in atmospheric CO_2 on timescales shorter than millions of years (Archer et al., 1998; Broecker and Peng, 1974). On millennial timescales, the rate at which calcite dissolves in the deep ocean controls the shape of the lysocline and the calcite compensation depth, influencing the capacity of the ocean to absorb and neutralize anthropogenic CO_2 (Archer, 1991; Boudreau, 2013). Calcite dissolution kinetics are critical for setting the timescales of these processes.

The rate of calcite dissolution in seawater is commonly described by an empirical rate law of the form:

Eq. 1) $\text{Net Dissolution Rate} = k\,(1 - \Omega)^n$

where Ω is the saturation state of the solution with respect to calcite, k is the empirical rate coefficient, and n is the reaction order. The simplicity of this formulation means it can be easily applied to the description of ocean sediment dissolution, diagenesis and carbon cycling. However, reported values of k and n derived from different experimental and field studies can vary by orders of magnitude (Berelson et al., 1994; Hales and Emerson, 1997; Keir, 1980; Morse and Berner, R. A., 1972). Reaction orders for calcite dissolution in seawater alone have been reported to span the range from near-zero to greater than 4.5, a range too wide to reflect measurement uncertainties alone.

The differences across estimates of n are consequential for how dissolution kinetics are considered in both small and global scale processes. The response of carbonate minerals to ocean acidification, carbonate sediment buffering against anthropogenic CO_2 and the extent of diagenetic exchange in pore fluids are all sensitive to the details of the rate law parameterization. This illustrates the need for a mechanistic, rather than empirical, approach to describes calcite dissolution rates.

Many existing mechanistic descriptions of calcite dissolution and precipitation are derived from classical crystal growth theory and kink density theory (Burton et al., 1951; Lasaga, 1998; Zhang and Nancollas, 1998). Their common premise is that the reaction rate is set by both the solution thermodynamic driving force (Ω) and the density and reactivity of features on the mineral surface. Atomic force microscopy (AFM) and vertical scanning interferometry (VSI) have been used to capture nano-scale surface topography and directly measure features like step edges and etch pits that are predicted from classical crystal growth theory. This method has been used to study the evolution of the calcite surface during precipitation and dissolution (Rolf S. Arvidson et al., 2006; Astilleros et al., 2010a; Ruiz-Agudo et al., 2010; Shiraki et al., 2000; Teng, 2004), but is limited in its ability to probe calcite dissolution close to equilibrium and translate surface measurements into bulk rates.

An alternative framework for describing calcite dissolution kinetics combines the equations derived from classical crystal growth theory with bulk rate measurements to invert for surface energetic parameters. Dove et al. (2005) employed this approach to describe the dissolution of

quartz as a function of undersaturation. They found that the dissolution behavior could be divided into three regimes that operate within define ranges of omega: (1) dissolution by the retreat of existing steps near equilibrium, (2) dissolution by the formation of etch pits at defects at intermediate undersaturations and (3) dissolution by the homogeneous formation of etch pits far from equilibrium. The transition between each mechanism occurs at critical undersaturations, denoted Ω_{crit}, that are identified by distinct changes in slope of the rate vs. undersaturation.

Naviaux et al. (2019a, 2019b) and Dong et al. (2018) used the Dove et al. (2005) framework to describe the controls on calcite dissolution on undersaturation in various seawater conditions (temperature, pressure, organic matter content). This body of work reframes the calcite dissolution rate law in Equation 1 into three distinct fits to k and n that are assigned to specific ranges of undersaturation. The resulting rate law captures mechanistic transitions at different Ω values. The invocation of an Ω dependence on n helped to reconcile the large variability in empirical estimates in the literature.

The Naviaux et al. (2019a) study relies on the highly sensitive isotope tracer method to quantify calcite dissolution rates in seawater, first described in this application by Subhas et al. (2015). This approach allows for orders of magnitude more sensitive measurements of dissolution rates, in particular, near equilibrium. However, the isotope tracer method has faced criticism as to whether it truly measures net dissolution rates. Isotope exchange has been invoked (DePaolo and Zhang, 2024) as a process that may obscure the overall dissolution signal. We argue that when isotope exchange is defined as the gross fluxes moving material on and off the mineral surface, it can be explicitly accounted for in these experiments.

We developed a simple box model, updated from Subhas et al. (2017), that describes calcite dissolution in terms of gross dissolution, gross precipitation and a reactive surface reservoir. We fit the model to the high resolution Naviaux et al. (2019a) dissolution experiments. The model naturally captures the coupled isotopic evolution of the mineral surface and aqueous reservoir and net dissolution rates can be defined once the system is at isotopic steady state. We find that that, under most conditions, the isotope tracer method can effectively capture net dissolution rates in the methods described by Subhas et al. (2017) and Naviaux et al. (2019a).

The model also offers unique mechanistic insights into calcite dissolution. We explore how gross dissolution rates and the reactive surface reservoir evolve with undersaturation and identify how these parameters can and cannot be brought to bear on the surface energetic description of dissolution.

2. Methods

2.1 Isotope label dissolution experiments

The isotopically labeled calcite dissolution experiments reinterpreted here were originally described by Naviaux et al. (2019) and Subhas et al. (2015). Briefly, 1–5 mg of isotopically enriched $Ca^{13}CO_3$ grains were dissolved in sealed reactor bags containing approximately 300 mL of seawater at a prescribed degree of undersaturation. Experiments were conducted at controlled temperatures and lasted from ~4 h to 5 days, with more undersaturated conditions corresponding to shorter experimental durations.

During each experiment, reactor bags were placed on a shaker table to ensure homogeneous mixing and to minimize transport limitations within the bulk solution. Each experiment was sampled at 5–10 approximately evenly spaced time points. At each sampling event, ~10 mL of

solution was withdrawn and immediately transferred into evacuated Exetainers for determination of dissolved inorganic carbon (DIC) concentration and $\delta^{13}C$ of DIC.

Isotopically labeled $Ca^{13}CO_3$ grains (>99 atom% ^{13}C; Sigma Aldrich, SKU 492027) were wet-sieved into two size fractions: 70–100 µm and 20–53 µm. Kr-BET surface areas were measured as 0.09 and 0.152 m^2/g, respectively.

2.2 Rate calculation

The primary experimental result is the time-resolved $\delta^{13}C$ of the bulk aqueous reservoir (**Figure 1**, left y-axis). In the previous work this data was converted to cumulative moles dissolved, *n*, following Equations 2 and 3, accounting for the evolving mass of solution as samples were removed over the course of the experiment.

Eq. 2) $${}^{i+1}_{i}n_{13C} = m_i * \left[{}^{12}C\right]_{init} * \left(R^{13}_{i+1} + R^{13}_{i}\right)$$

Eq. 3) $$R^{13}_{i} = \left(\frac{\delta^{13}C_i}{1000} + 1\right) * \quad R^{13}_{PDB}$$

Here, the subscript *i* denotes the timepoint, m_i is the mass of seawater at timepoint *i*, $[^{12}C]_{init}$ is the initial concentration of ^{12}C, and R^{13}_i is the ratio of $^{13}C/^{12}C$ at timepoint *i*. Cumulative moles of calcite dissolved at each sampling time (**Figure 1**, right y-axis) were obtained by summing incremental dissolution from the start of the experiment to time t_i. Net dissolution rates were calculated by fitting a linear regression to the portion of the cumulative dissolution versus time curve that exhibited linear behavior, where it is assumed that the dissolving surface attained isotopic steady state. The slope of this regression yields the net dissolution rate in units of moles per unit time, which are reported normalized to surface area.

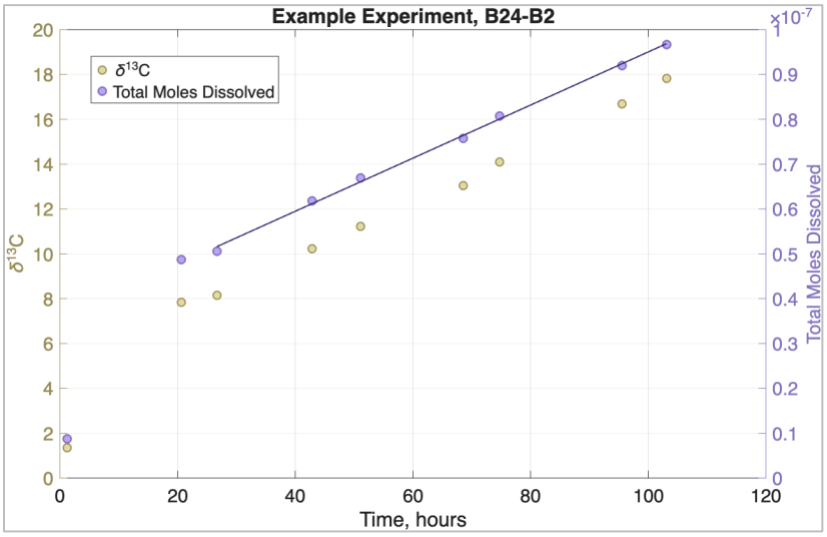


Figure 1. Example results from the work of Naviaux et al. (2019), shown for experiment B24-B2. The left y-axis and light grey points represent the $\delta^{13}C$ signal in the bulk reservoir over the course of an experiment. The right y-axis and purple points show the "total moles dissolved" over the course of an experiment. The line through a subset of the purple, "moles dissolved" points is a linear regression for data between t = 24 hours and the end of an experiment (in this case ~105 hours), used to calculate the net rate in Naviaux et al (2019).

3. Model

3.1 Model description

The Naviaux et al. (2019) experiments can be represented in terms of a two-reservoir model of the labeled grains and seawater reservoir. These reservoirs and their integrations are schematically illustrated in **Figure 2**. The seawater reservoir represents the roughly 300mL of seawater set to a constant undersaturation that is sampled in ~ 10mL increments over the course of an experiment. The change in volume from sampling is reflected in the model as a step change in the aqueous volume, v_{aq}.

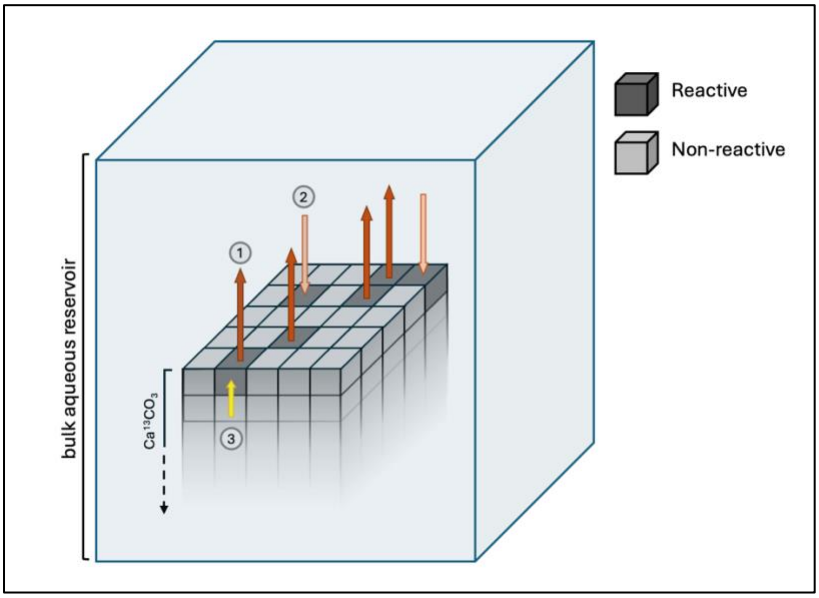


Figure 2. Schematic representation of 2-box calcite dissolution model. The shaded blue volume represents the bulk aqueous reservoir in which an experiment is performed. The size of this reservoir changes with time but is held at roughly constant undersaturation. The calcite grains are represented by the cube inside the aqueous reservoir that is subdivided into unit cells. Near the surface of the grain, unit cells may either be reactive (dark grey cubes) or unreactive (light grey cubes). Gross dissolution (1) and gross precipitation (2) are denoted by the dark and light orange arrows, respectively. Net dissolution (3), denoted by the yellow arrow, makes up the difference of the gross dissolution and gross precipitation fluxes such that the size of the reactive reservoir is constant during an experiment.

The isotopically labeled calcite grains that are subject to dissolution during an experiment sit inside the seawater reservoir. We model the solid simply as a collection of $CaCO_3$ unit cells (cubes in **Figure 2**). Near the mineral surface, a fraction of the unit cells are considered reactive sites (dark grey cubes), meaning they may participate in gross dissolution or precipitation reactions (dark and light orange arrows, respectively). The number of reactive sites is held constant over the course of an experiment via the replacement of a "dissolved unit cell" with a unit cell from the interior of the grain (yellow arrow, 3). The model is agnostic to the source of the reactive sites (step edges vs. etch pits) and to the type of site (obtuse vs. acute). All reactive sites are treated equally in the model.

The experiments of Naviaux et al. (2019) were performed on shaker tables set to shake at rates that ensured the experiments were not transport limited. Because the experiments are well outside of the transport control regime, we do not include an aqueous diffusive boundary layer in the model. In model sensitivity tests, we found that the addition of an aqueous diffusive boundary

ranging in size from 1um to 100um (greater than the diameter of an individual grain) did not significantly change our parameter estimates.

3.2 Model initial condition and free parameters

The free parameters in the model are: (1) gross dissolution rate, G_{off} in sites/s, (2) the ratio of gross precipitation (G_{on}) to gross dissolution, R unitless, and (3) the number of reactive surface sites, S in molecules. The seawater reservoir is set to the measured $\delta^{13}C$ of the seawater solution used in each experiment (generally between -1 to 1‰). The reactive solid sites are initially 100% ^{13}C for all experiments. As the experiment proceeds with time, carbon is moved between the solid and solution reservoirs. The time-evolution of ^{12}C and ^{13}C are tracked in both reservoirs of the model.

3.3 Model equations

We describe the exchange of material between the solid and the solution over time following Equations 4-6:

Eq. 4) $$\frac{d[^{13}C]_{aq}}{dt} = \left[G_{off} * F^{13}_{R.Surf} - (G_{off} * R) * F^{13}_{bulk} \right] / v_{aq}$$

Eq. 5) $$\frac{d[^{12}C]_{aq}}{dt} = \left[G_{off} * \left(1 - F^{12}_{R.Surf}\right) - (G_{off} * R) * \left(1 - F^{12}_{bulk}\right)\right] / v_{aq}$$

Eq. 6) $$\frac{d(n^{13}C_s)}{dt} = (G_{off} * R) * F^{13}_{bulk} - G_{off} * F^{13}_{R.Surf} + \left(G_{off} - G_{off} * R\right) * F^{13}_{B.Solid}$$

Where, $[^{13}C]_{aq}$, $[^{12}C]_{aq}$ are the concentrations of ^{13}C and ^{12}C in the bulk aqueous solution. The terms $n^{13}C$ and $n^{12}C$ are the number of reactive sites composed of ^{13}C or ^{12}C, respectively. These two terms sum to the value of S. The term R is the ratio of G_{on}/G_{off} (varies between 0-1). The F terms in Equations 4-6 represent fractions of ^{13}C or ^{12}C in each reservoir following Equations 8-11.

Eq. 8) $$F^{13}_{R.Surf} = \frac{n^{13}C_s}{n^{13}C_s + n^{12}C_s}$$

Eq. 9) $$F^{12}_{R.Surf} = 1 - F^{13}_{R.Surf}$$

Eq. 10) $$F^{13}_{bulk} = \frac{[^{13}C]_{bulk}}{[^{13}C]_{bulk} + [^{12}C]_{bulk}}$$

Eq. 11) $$F^{12}_{bulk} = 1 - F^{13}_{bulk}$$

Note that F terms for the solid must sum to 1. Likewise note that the term $dn^{12}C/dt$ is not explicitly modeled.

Together, Equations 4-6 track the time evolution of isotopic composition in both reservoirs as gross fluxes continuously exchange material across the mineral-fluid interface.

Model parameters were estimated by minimizing the sum of squared residuals between measured and modeled $\delta^{13}C$ values using the MATLAB nonlinear least-squares solver *lsqnonlin*. The residual function used in the optimizer is:

Eq. 13) $Residual = \frac{1}{2}\sum_{i=1}^{N}(\delta^{13}C^{i}_{model} - \delta^{13}C^{i}_{measured})^2$

The parameters are bound to physically meaningful ranges: G_{off} between 10^9 and 10^{20} sites/s, R between 0.001 and 0.999, and S between 10^5 and 10^{20} molecules of sites. Optimization runs were kept only if *lsqnonlin* reported successful convergence ("Exit Flag 1" in *lsqnonlin*) and the final residual score fell below a prescribed threshold.

To reduce sensitivity to initial parameter guesses and to propagate analytical uncertainty, we used a Monte Carlo approach. For each experiment, 500 independent optimization runs were performed using random initial parameter values from the allowed ranges. For each realization, measured $\delta^{13}C$ values were perturbed assuming a normal distribution with a standard deviation of 0.15‰. The resulting suite of accepted solutions defines the uncertainty distributions for fitted parameters.

4. Model dynamics

Here, we step through how individual parameters and coupled parameters change the structure and magnitude of the isotopic signal in both the fluid and on the mineral surface. All of the example sensitivity tests (**Figures 3, 4 and 5**) are performed assuming the same mass of labeled grains, starting solution $\delta^{13}C$, background DIC and bulk volume change.

4.1 Gross and net rates

We first consider the combined influence of G_{off} and R. Together these two parameters define the net rate following:

Eq 14) $Net = G_{off} * (1 - R) * \frac{1}{SA_{BET} * m}$ [mol/cm^2/s]

Where G_{off} and R are the free parameters described above, SA_{BET} is the BET surface area and m is the mass of label grains used in a given experiment. In **Figure 3** we show different combinations of G_{off} and R that result in the same net dissolution rate but produce different $\delta^{13}C$ vs. time signals. Each pair experiences a different degree of curvature in the first ~5 hours of an experiment (**Figure 3a)** driven by how quickly the mineral surface reaches a steady-state isotopic value (**Figure 3b**).

For the experiment with the slowest gross rate (10^{-13} mol/cm^2/s) and $R = 0$ (i.e., net dissolution rate = gross dissolution rate), there is no gross precipitation. This means the mineral surface never accumulates any ^{12}C, which can only obtained via gross precipitation, so the system's isotopic steady state is equal to the initial condition of 100% ^{13}C. This is illustrated by the yellow line in **Figure 3b**, which sits at a constant value of 1 (100% ^{13}C). Likewise, there is no curvature in the slope of $\delta^{13}C$ vs. time in solution.

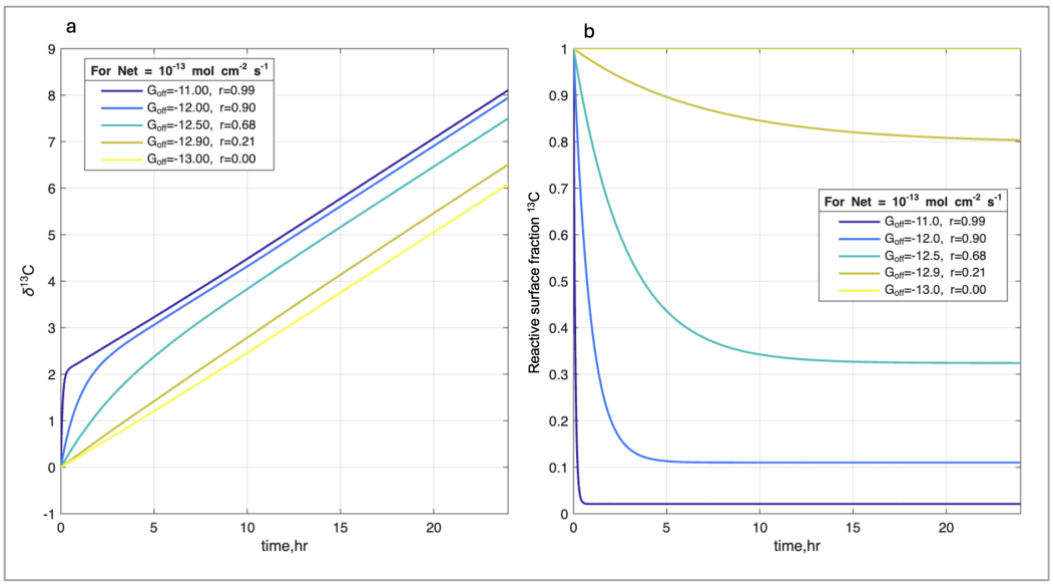


Figure 3. Model sensitivity to G_{off} and R for constant net rates. All example models shown here have a net dissolution rate of 10^{-13} mol/cm2/s and are run under the same conditions, only varying G_{off} and R. The color coding corresponds to the G_{off}, R values noted in the legend. (a) The evolution of aqueous $\delta^{13}C$ as a function of time. (b) The corresponding evolution of the mineral surface (reported as a "fraction of the reactive sites that are ^{13}C") as a function of time.

By contrast, the model run with the fastest gross dissolution rate ($G_{off} = 10^{-11}$, two orders of magnitude greater than the net rate) requires a large contribution from gross precipitation to still achieve a net rate of 10^{-13} mol/cm^2/s. As a result, a large amount of ^{12}C can be added to the mineral surface and the steady-state isotopic composition can reach very low ^{13}C. The magnitude of these fluxes is so large that the rate of surface isotopic evolution is rapid. We note a large initial drop in ^{13}C on the mineral surface that subsequently plateaus and a steep initial increase in $\delta^{13}C$ in solution that likewise reaches a constant value on short timescales.

In general, at faster net rates the model's sensitivity to R decreases. The gross fluxes required in this condition are necessarily large, so the surface reaches steady state very rapidly, regardless of the G_{on}/G_{off} ratio. The result is $\delta^{13}C$ vs. time traces that are linear over timescales that can be practically resolved in the Naviaux et al. (2019a) method. The gross dissolution can be still resolved under these conditions based on the magnitude of the $\delta^{13}C$ signal, as seen in the offset between model curves in the inset in **Figure 4a**.

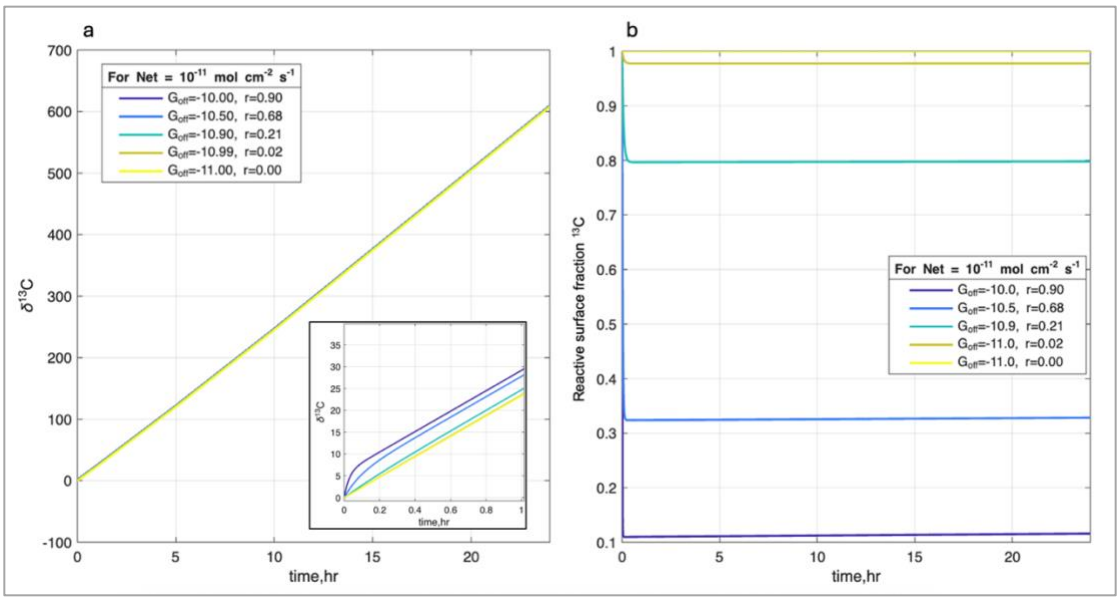


Figure 4. Model sensitivity to G_{off} and R at fast net dissolution rates. All example models shown here have a net dissolution rate of 10^{-11} mol/cm^2/s and are run under the same conditions, only varying G_{off} and R. The color coding corresponds to the G_{off}, R values noted in the legend. (a) The evolution of aqueous $\delta^{13}C$ as a function of time. The different models are not discernable on this scale. The inset zooms in on the first hour of the model. (b) The corresponding evolution of the mineral surface (reported as a "fraction of the reactive sites that are ^{13}C") as a function of time.

Figure 3a and **Figure 4a** illustrate the basis for the assumptions in Naviaux et al.'s (2019a) rate calculation. In their approach, as described in Section 2.2, they only fit the linear portion of their measured $\delta^{13}C$ vs time signal. The slope from this region is used to calculate the net rate. Our model results confirm that the steady state slope is a well-defined indicator of the net dissolution rate, regardless of the magnitude of the gross fluxes.

4.2 Reactive surface reservoir

The size of the reactive surface reservoir, S, is not directly related to the net rate in the same way as G_{off} and R, but it still influences the $\delta^{13}C$ vs time signal. In **Figure 5**, S varies and all other parameters are held constant. On long timescales, all models achieve the same slope for the linear portion of their $\delta^{13}C$ vs. time trace. The S term modifies both the timescale to achieve the steady state portion of the curve and the magnitude of the $\delta^{13}C$ signal.

When the reactive surface reservoir is small (e.g., yellow lines in **Figure 5)**, the mineral surface and solution reach isotopic steady state rapidly. When the surface reservoir is large (e.g. blue lines in **Figure 5**), it takes much longer to reach steady state for the same G_{off} and R. In some cases, if the reactive surface reservoir is very large, the initial rapid increase in $\delta^{13}C$ can appear linear on timescales typical of the Naviaux et al. (2019a) experiments (**Figure 5b**, dark blue lines). However, over longer timescales (**Figure 5a**), this curvature does, in fact, transition to linear slopes that are equal across all S values. Likewise, the steady state surface composition is constant across S values; only the timescales to reach steady state change.

The larger the reactive surface reservoir, the more ^{13}C is available to move into solution, resulting in larger $\delta^{13}C$ values. Even for the same steady state "fraction" of ^{13}C on the mineral surface, a larger reservoir means a larger total number of ^{13}C atoms that can be released into solution.

Notably, the *S* parameter loses sensitivity when *R* is small (i.e., net dissolution rate = gross dissolution rate). Under this condition, there is little or no back precipitation such that little to no ^{12}C can be added to the mineral surface. This means that regardless of the surface reservoir size, it is always very close to pure ^{13}C. This loss of sensitivity holds for all magnitudes of gross dissolution rates.

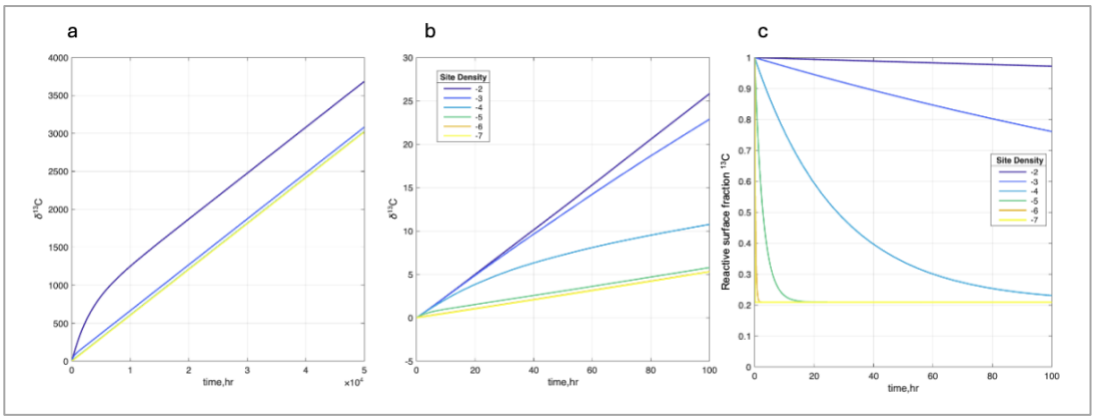


Figure 5. Model sensitivity to reactive sites, S. All synthetic experiments are run with $G_{off} = 10^{-13}$ mol/cm2/s, R = 0.8. (a) $\delta^{13}C$ vs. time for 10^5 hours. (b) Zoomed in to the first 100hr of the models plotted in (a) to the first 100 hours of the model run. (c) Reactive surface fraction of 13C as a function of time.

4.3 Limitations of the model

The model is particularly effective where there is discernible curvature in the $\delta^{13}C$ vs. time structure. This is one of the key benefits of the modeling approach compared to the linear fitting employed by Naviaux et al. (2019): we take advantage of additional measurements omitted in Naviaux et al.'s (2019a) linear fitting. Likewise, we don't need to decide a priori when steady state is reached; the model accounts for this as it fits the data.

Together, *R* and *S* exert much of the control on the degree of curvature at the start of an experiment, via the magnitude of exchange and the size of the exchangeable reservoir, respectively. Under conditions where there is no curvature, the model cannot parse between the contributions of *R* and *S* to the $\delta^{13}C$ and we lose sensitivity to these parameters.

5. Results

5.1 Model fitting

A single run of the optimizer returns a combination of the three free parameters: the gross dissolution rate G_{off}, the gross rate ratio *R* (= G_{on}/ G_{off}), and the reactive site abundance *S*. The Monte Carlo approach described in Section 4 results in an ensemble of parameter combinations. We report G_{off} in mol/cm^2/s and *S* in mol/m^2, consistent with surface-area-normalized rates in the geochemical literature and allowing for direct comparison with the net rates of Naviaux et al. (2019a).

Figure 6 shows model fits to a representative experiment (T30-B3; 21°C, Ω = 0.81). The measured aqueous $\delta^{13}C$ data are shown in pink in **Figure 6a** with an ensemble of model curves (n = 330) in grey. The fits are sufficiently similar that they appear as a single thick grey band.

Figure 6b shows, for the same parameter combinations, the model-predicted isotopic composition of the mineral surface as a function of time.

No measurements of the solid were made in the Naviaux et al. (2019a) experiments, but we can use the predicted surface evolution to illustrate the origin of the curvature in the aqueous $\delta^{13}C$ trace. The surface, initially 100% ^{13}C, evolves toward a steady-state composition of roughly 20–40% ^{13}C over approximately 10–20 hours. This interval corresponds to the steepest slopes in the aqueous measurements. As the surface ^{13}C becomes progressively diluted, the isotopic signal released into solution weakens even though the gross fluxes remain constant. Once the surface reaches isotopic steady state, the aqueous $\delta^{13}C$ evolves roughly linearly with time. This region in both the measured $\delta^{13}C$ signal and the model holds information about the net rate.

The slight increase in the measured and modelled $\delta^{13}C$ signal over the 20-60 hour window in **Figure 6a** is due to the decrease in volume of the experimental reservoir as samples are collected. Roughly 25% of the total volume is removed from the bulk reservoir over the course of an experiment (10mL per sample, ~8 samples over an experiment). As a result, the isotope signal from dissolution is felt increasingly strongly as it is released into a shrinking reservoir. The effect is small, but non-zero. We explicitly define the decrease in volume in the model and capture this signal well, as seen in **Figure 6a**.

The key result of our modelling is that we capture the full nonlinear evolution of the aqueous $\delta^{13}C$ signal using constant gross fluxes and therefore a constant net rate. The dynamic behavior of the aqueous isotope signal does not require a rate that evolves in time; it emerges entirely from the isotopic evolution of the surface reservoir. This distinction is central to the reinterpretation of the near-equilibrium data in Sections 5.2 and 6.

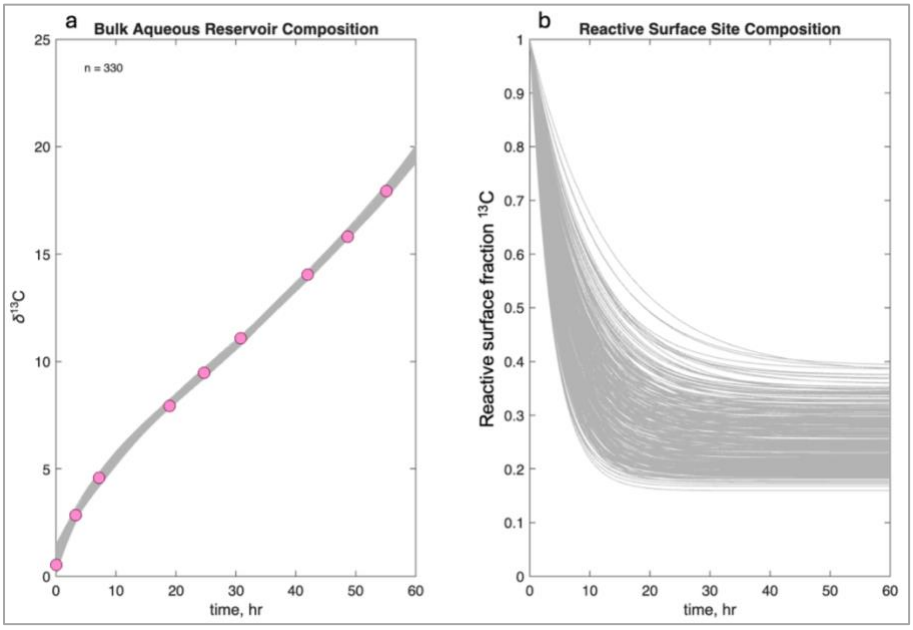


Figure 6. Example model fits for experiment T30-B3 at 21°C, Ω = 0.82. (a) $\delta^{13}C$ of the reactive aqueous reservoir. Measured data are in pink. Error bars on individual measurements are smaller than the size of the points. Grey lines are the model fits, n = 330. The model fits are all comparable and sit close to each other such that they look like a thick grey line. (b) Model predicted surface isotopic composition as a function of time.

In **Figure 7**, the values of net rate (calculated following Equation 14) and the individual model free parameters are reported as histograms. The results are generally Gaussian distributions over relatively tight parameter ranges. The range of net rates in **Figure 7d**, calculated from G_{off} and R combinations following Equation 14, exhibits a tighter range in values than the G_{off} parameter. The range in this example, of less than 0.1 log units, is well within the uncertainty on an individual rate measurement reported in Naviaux et al. (2019). The origin of this tight constraint is shown in the parameter covariances (**Figure 8**).

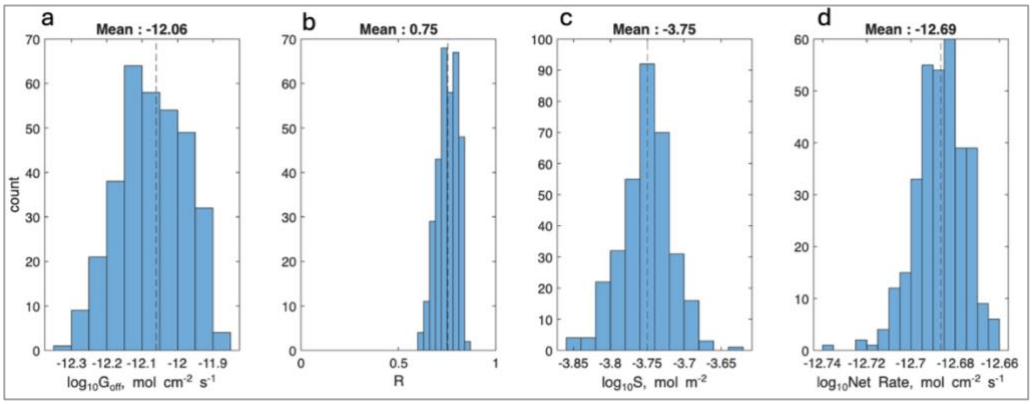


Figure 7. Histograms for model parameters in fits for the model curves shown in **Figure 6**. (a) Gross dissolution rate, mol/cm^2/s, (b) ratio of gross precipitation to gross dissolution, (c) reactive surface site density and (d) net dissolution rate.

In **Figure 8** the parameters for the fits in **Figure 6** are plotted against each other. The color denotes the residual score determined for each model run. All of the results shown were considered local minima in the optimizer algorithm described above. The spread in each parameter (also seen in **Figure 7**) is the result of (1) error propagation thought the model and (2) genuine covariances in parameters. The structure in the score data seen in **Figure 8** (e.g. that lower gross rates tend to have a slightly worse scores) likely reflects the fact that perturbations to the measured $\delta^{13}C$ via our Monte Carlo algorithm do not translate linearly to perturbations in parameters. This means that some manifestations of the error propagation systematically fit worse than the others. However, all of the scores reported here represent fits that are statistically indistinguishable within our $\delta^{13}C$ measurement error.

The strong covariation in G_{off} and R follows a relationship of roughly constant net dissolution rate. The positive correlation represents the trade-off between increasing G_{off} and correspondingly increasing G_{on} (via an increase in R). The difference between G_{off} and G_{on}, however, stays roughly constant and gives rise to the linear portion of the $\delta^{13}C$ v. time curve and a well-defined net rate.

The site term S is only weakly correlated with G_{off} and R in this experiment. In some experiments we note a stronger negative correlation between S and G_{off}, which can be seen in a subset of the points in **Figure 8a**. This behavior is consistent with the structure of the initial $\delta^{13}C$ vs. time curvature. The steep initial $\delta^{13}C$ curvature is controlled by both the size of the surface reservoir and the rate at which that reservoir is released into solution. The negative correlation represents the tradeoff between these two parameters for modulating the magnitude and the timing of the large initial $\delta^{13}C$ signal.

The behavior described for T30-B3 is representative of most experiments. Below, we discuss the key exceptions that arise from (1) insufficient $\delta^{13}C$ data density at the start of an experiment, (2) insufficient sampling duration and (3) model insensitivities.

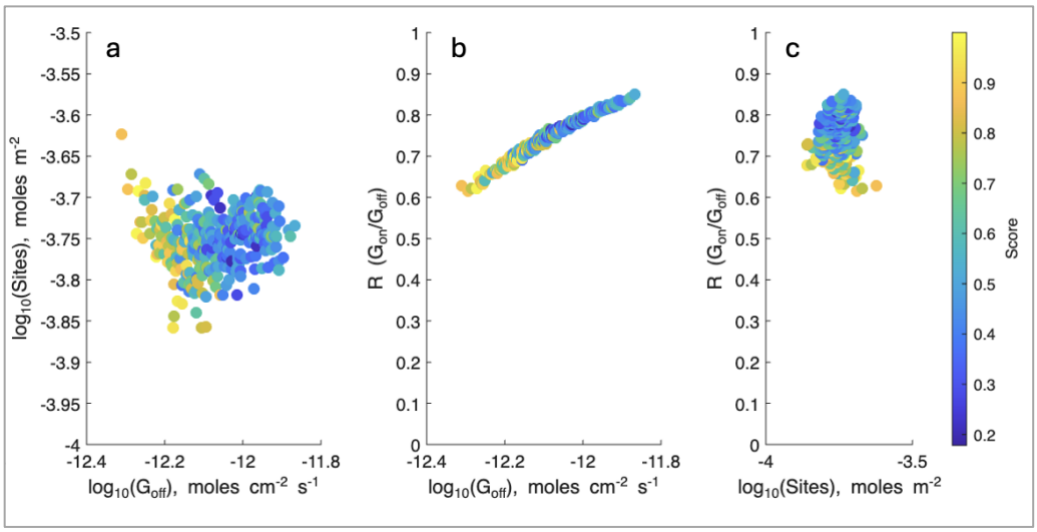


Figure 8. Individual parameter fits for the model curves shown in Figure 6. (a) Cross plot of *S* and G_{off}, (b) cross plot of R and G_{off} and (c) cross plot of *R* and *S*. The color coding corresponded to the value of the residual score, shown in the color bar, for each model fit.

5.2 Constraints and limitations on parameter recovery

5.2.1 Poorly constrained initial $\delta^{13}C$ curvature

Some experiments have low data density in the first 24 hours. This is the period in which much of the curvature in the $\delta^{13}C$ trace is observed. As a result, the optimizer finds equally good fits to the measured data with very different manifestations of curvature at the start of an experiment. This is illustrated in **Figure 9**.

In the absence of an additional constraining data point in the 24-hour window, the optimizer produces two distinct populations of model parameters with different $\delta^{13}C$ vs. time traces. The two fits reflect either high *R* with faster G_{off} (steeper initial curvature in the $\delta^{13}C$ vs. time plots) or low *R* with slower G_{off} (shallower initial curvature in $\delta^{13}C$ v. time plots). Both populations have significant overlap in *S* value for the sites term.

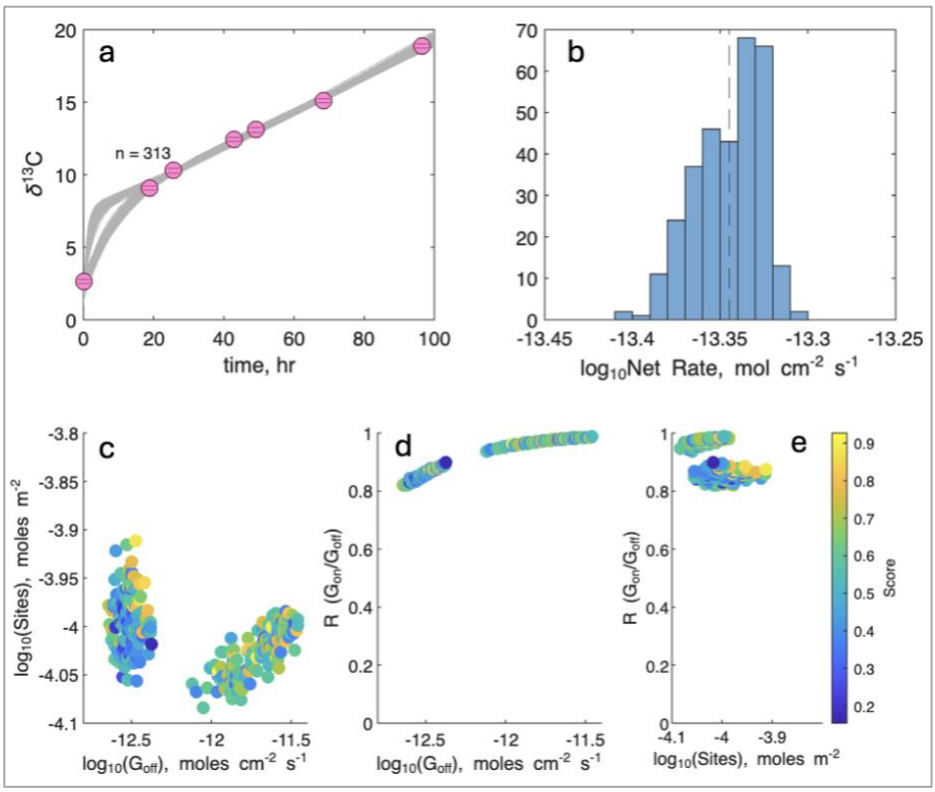


Figure 9. Fits for experiment T1-B1, 21°C, Ω = 0.92. (a) Measured $\delta^{13}C$ data (pink circles) and model predicted $\delta^{13}C$ vs. time (grey lines). (b) Histogram of net rates calculated from G_{off} and R, following Equation 14. (c-d) Cross plots of fitted parameters. Color bar denotes the residual score for each pair of fitted parameters.

Both populations give rise to roughly the same net rate. The net rate is well constrained by the $\delta^{13}C$ data measured in the latter portion of the experiment as seen in **Figure 9D**. G_{off} and R are strongly correlated along a line of constant net rate (curved because of the log scale). The two modes of fitting the initial part of the experiment only impact the partitioning of the net rate into individual parameters.

The two populations have slightly difference distributions in residual scores: the models with shallower curvature (low G_{off}, low R) have a lower mean score than models with steep curvature (high G_{off}, high R), but with significant overlap in 1σ. Compared to experiments run at similar undersaturations and temperatures, we find that the low G_{off} and low R population are more consistent across experiments.

5.2.2 Insufficient sampling duration

For some experiments, in particular the slowest and closest to equilibrium, the duration over which the experiment was run was not long enough to achieve isotopic steady state. The result is insufficient data to fully constrain the parameters in the model. Here, the optimizer finds solutions ranging from linear to entirely rolled over, as seen in **Figure 10a**. These models all fit the measured data equally well but predict very different behavior for the $\delta^{13}C$ signal after the timing of the last measured sample.

In particular, a large portion of the models predict a strong rollover in the $\delta^{13}C$ signal, reflecting R approaching 1. This is illustrated in the cross-plots in **Figure 10e,f**, where the R value

accumulates at the upper bound of 1. One of the reasons this behavior may arise is because of a failure mode in our combined model + optimizer structure. The fact that model results are pushed to 1 may be, in part, a relic of the optimizer algorithm hitting a forced bound. We require the *R* parameter to sit between 0.001 and 1. MATLAB's *lsqnonlin* trust-region-reflective algorithm estimates the Jacobian with finite differences, applying a small perturbation to each parameter and measuring the change in residuals. Near a bound, that perturbation can only be evaluated on one side, meaning the optimizer cannot step past $R = 1$ to see what the objective function looks like beyond it. This produces a one-sided, biased estimate of local sensitivity. The algorithm's fitting criteria are evaluated on the same biased estimate, so a parameter pinned against a bound with a small gradient can still satisfy the "converged" condition. The $R = 1$ output in this case is not necessarily optimal, but the optimizer cannot distinguish a real minimum from a minimum imposed because of the parameter bounds. This is exacerbated by the insufficient samples to help constrain R in the later part of an experiment.

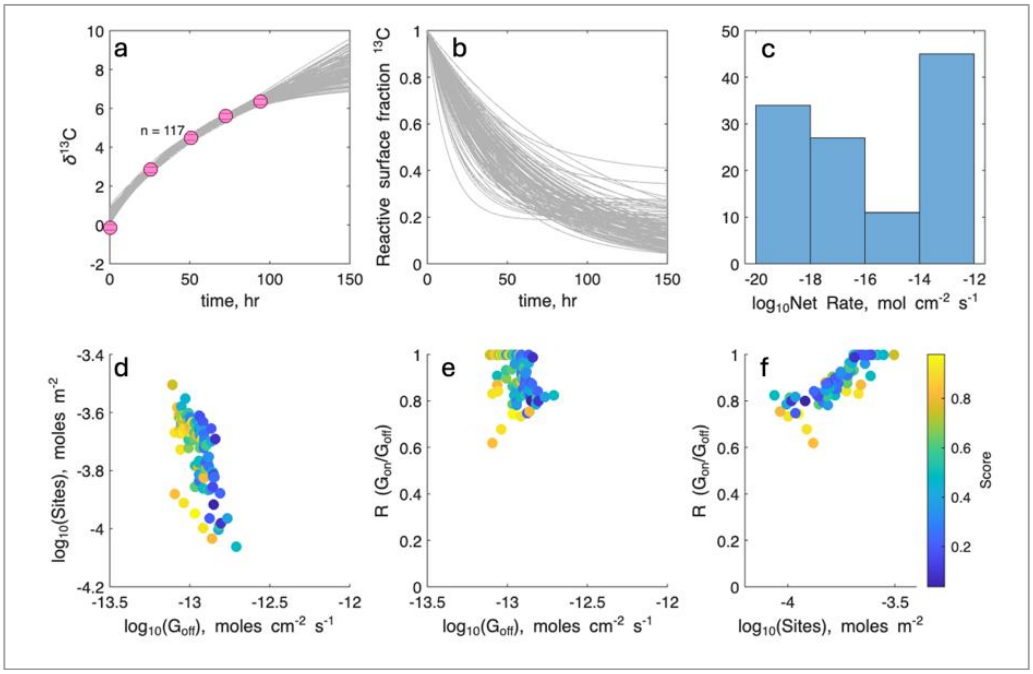


Figure 10. For example, experiment T11-B4, 5°C, Ω = 0.95. (a) Measured $\delta^{13}C$ data (pink circles) and model predicted $\delta^{13}C$ vs. time (grey lines). (b) Surface isotopic composition with time. (c) Histogram of net rates calculated from G_{off} and R, following Equation 14. (d-e) Cross plots of fitted parameters. Color bar denotes the residual score for each pair of fitted parameters.

If we were to explicitly allow $R > 1$, we would need to modify our treatment of the mineral surface reservoir. Even then, there are no well-defined descriptions of how net dissolution transitions continuously into net precipitation, so any numerical treatment would necessarily introduce a step function in the model. A discontinuity at $R = 1$ would produce the same failure as the bound case, without requiring a hard constraint. Because *lsqnonlin* is a local, gradient-based method, at every step it builds a locally linear model of the objective function from the finite-difference Jacobian and uses that linear model to decide where to move next. This only works if the objective function is smooth enough that a linear approximation is meaningful over the scale of the finite-difference step. A step-function transition between the dissolution and precipitation regimes violates this assumption.

These numerical issues are confounded by the fact that the experiments exhibiting this forcing toward the $R = 1$ bound do, in fact, sit very close to equilibrium, a regime in which R approaching 1 makes physical sense. Near equilibrium, gross precipitation is expected to approach gross dissolution, so a genuine physical signal and a numerical artifact point in the same direction. We cannot definitively determine how close to unity R actually gets. The models of $R = 0.9$, 0.99, or 0.999 all produce very similar $\delta^{13}C$ vs. time curves, but by definition (**Equation 14**) results in orders of magnitude different net rates for roughly the same gross dissolution rate.

However, if the results pushing R towards 1 where merely a numerical artifact, we would expect every Monte Carlo realization to converge there. Instead, while the majority of realizations do accumulate at or very near $R = 1$, a subset produces well-resolved fits at meaningfully lower R values (as low as ~0.6–0.85; **Figure 10d**). These fits are not pinned against a bound and represent well defined local minimum resolved by the optimizer that fit the data well. We treat this type of experiment as containing two solution populations: (1) a population with a well-defined local minimum in R, and (2) a population forced toward $R = 1$. At present, we treat the net rate value estimated from the first population as an upper bound on the net rate.

Even where sensitivity to R is lost, G_{off} and S can be well defined. These two parameters influence the magnitude and timescale of the initial $\delta^{13}C$ curvature, respectively, and can be captured by the existing data even when the final steady-state value of $\delta^{13}C$ is not.

5.2.3 Loss of parameter sensitivity far from equilibrium

As noted above (Section 4) the model can lose sensitivity to certain parameters far from equilibrium, when the $\delta^{13}C$ vs. time measured data approach a linear slope for all samples. This loss of curvature makes it difficult for the model to parse between the relative contribution of the free parameters.

In some cases, G_{off} is well defined despite noise in other parameters. This is consistent with the far from equilibrium condition that $G_{on} << G_{off} \sim$ Net. In these cases, the gross dissolution rate is insensitive to the fact that R is noisy and small. We recover gross dissolution rate values here, but we do not consider R and S to be independently identifiable.

5.3 Undersaturation dependence of model parameters

The model does not consider the thermodynamic driving force for dissolution (1- Ω) or the temperature in the box model or optimizer, though we know both of these values precisely for all experiments. The plots of parameters vs. undersaturation are arrived at wholly independently with no assumptions about the calcite rate law. The undersaturation dependence of parameters and the calculated net rates come exclusively from the structure of the $\delta^{13}C$ data with time. The results for 5°C, 12°C, 21°C and 37°C are shown in **Figure 11**. All parameters show a strong, nonlinear dependence on undersaturation.

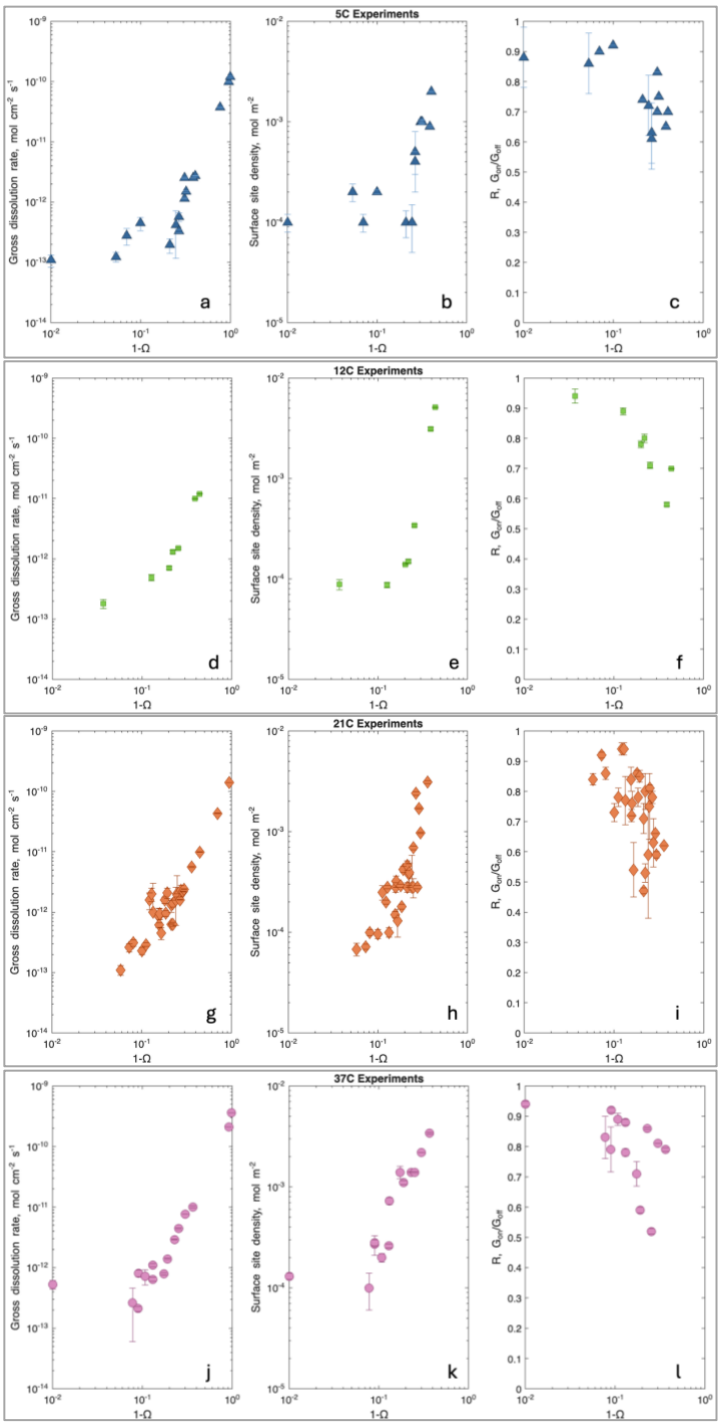


Figure 11. Model optimized parameters as a function of undersaturation for 5°C (a, b, c), 12°C (d, e, f), 21°C (g, h, i) and 37°C (j, k, l). Where error bars cannot be seen, they are smaller than the size of the marker.

Where possible, we define an Ω_{crit} for a statistically meaningful change in slope in individual parameters, shown in **Table 1**. For the 12°C experiments, there were too few experiments for the changepoint analysis to meet criteria for a minimum number of points in each regression. For all temperatures, a changepoint was identified for parameter R, but it was not determined to be statistically significant (denoted by a star in Table 1). With the exception of 37°C, the Ω_{crit} values

for net rate are largely consistent with the range of 0.75-0.8 estimated by Naviaux et al. (2019a) and Naviaux et al. (2019b). At 37°C the shift in changepoint to higher Ω is likely driven by a single datapoint at Ω ~ 0.01. The Ω_{crit} values identified for each parameter are largely consistent with the Ω_{crit} for net rate at a given temperature.

Table 1. Ω_{crit} values for modelled net rates and individual parameters.

Temperature	Ω_{crit} – ***Net Rate***	Ω_{crit} - G_{off}	Ω_{crit} - ***S***	Ω_{crit} - ***R***
5°C	0.79 ± 0.03	0.77 ± 0.02	0.78 ± 0.02	0.88 ± 0.05*
12°C	low data density			
21°C	0.74 ± 0.01	0.83 ± 0.06	0.77 ± 0.02	0.84 ± 0.06*
37°C	0.90 ± 0.01	0.90 ± 0.02	0.91 ± 0.01	0.86 ± 0.05*

6. Discussion

6.1 Isotope exchange considerations

Isotope exchange is commonly invoked as a process that complicates the interpretation of isotopic labeling experiments because it may be conflated with the isotope signal from net dissolution (DePaolo and Zhang, 2024; Harrison et al., 2022). DePaolo and Zhang (2025) argue that a background, time-sensitive isotope exchange flux, operating separately from the gross dissolution and precipitation fluxes, is convolved with the net rate signal for the close to equilibrium Naviaux et al. (2019a) experiments. Among the mechanisms they propose as candidates for isotope exchange are Oswald recrystallization, impurity replacement and solid state diffusion. By their own calculations, the former two processes are likely negligible for explaining the magnitude of the Naviaux et al. (2019a) dissolution signals.

The most plausible mechanism is solid state diffusion. Solid state diffusion is generally thought to be negligible at ambient temperatures. Most measurements of solid state diffusion in calcite are done at high temperatures and/or pressures and extrapolated to Earth surface conditions (Farver, 1994; Labotka et al., 2004). There may be some evidence for enhanced solid state diffusion via diffusion along grain boundaries in calcite (Farver and Yund, 1991; Fisler and Cygan, 1999), but these experiments, too, are extrapolated from high temperature conditions. Géhin et al. (2021) provide an estimate for the diffusion constant in calcite at 25°C, 4.8x 10^{-25} m^2/s.

To tell if solid state diffusion is important, we perform a simply flux comparison analysis. We translate diffusion into flux terms following:

Eq. 15) $$F_D = \frac{D_{ss}}{L_{ss}} M_{cc} * 100^{-2}$$

where F_D is a diffusive flux in $mol/cm^2/s$, D_{ss} is the solid state diffusion coefficient, M_{cc} is the molar density of calcite (26300 mol/m^3) and L_{ss} is the length scale over which diffusion operates (m). For a conservative estimate, we assign L_{ss} to 1 monolayer (0.5nm), which we consider to be an underestimate of the reactive surface (Section 6.2.2). Using the Gehin et al. (2021) estimate for D_{ss}, the resulting diffusive flux is ~2.5 x 10^{15} $mol/cm^2/s$, about an order of magnitude slower than our slowest measured dissolution rates.

DePaolo and Zhang (2025) propose a larger diffusion coefficient, on the order of 10^{-23} m^2/s, based on the SIMS profiles from (Subhas et al., 2017). The profiles showed ^{12}C penetration up to 6 monolayers deep into pure ^{13}C calcite after exposure to slightly undersaturated waters. DePaolo

and Zhang (2025) argue that this profile represents solid state diffusion. In Subhas et al. (2017) and here, this signal is interpreted as the size of the exchangeable surface reservoir during dissolution. We identify multiple lines of independent evidence in Section 6.2.2 for a large, reactive surface reservoir that interacts with solution.

Our model captures the curvature in $\delta^{13}C$ using just the gross fluxes and the surface sites term (reactive surface reservoir). No additional isotope exchange term is required to reproduce the measured data, as invoked in DePaolo and Zhang (2025). Further, the data are fit using constant values for the free parameters. Even though there is no time dependence of these terms in the equations, they are able to fit $\delta^{13}C$ data that is nonlinear with time.

When defined simply as the transfer of isotopic material between the solid and solution, isotope exchange is naturally represented by the gross fluxes in the present framework. This formulation allows the gross signals (isotope exchange) to be deconvolved from the net rate signal.

Naviaux et al. (2019a) interpreted only the linear portion of the δ13C v. time trajectories and used the slope of this interval to estimate net dissolution rates (**Section 2.1**). They correctly recognized that this interval corresponds to a period in which the system is at isotopic steady state, whereas the initial curvature reflects transient evolution of the mineral surface toward steady state. For slowly reacting, near-equilibrium experiments, they assumed that isotopic steady state was reached after approximately 24 hours.

Our results show that the timescale required to achieve isotopic steady state depends strongly on the magnitude and ratio of the gross rates. Slower gross dissolution and precipitation fluxes require longer timescales for the mineral surface to reach isotopic steady state. In some experiments, our modelling suggests that isotopic steady state is reached well after the 24 hour interval assumed by Naviaux et al. (2019a). As a result, a subset of the Naviaux et al. (2019a) experiments were not sampled for sufficient durations to capture the true net rate signal. Their estimates of the supposed “net rate” from the linear regression approach (Section 2.2) actually capture some component of the gross rates.

These experiments do, in fact, contain some degree of an “isotope exchange” signal that operates on an order of magnitude capable of obscuring the net rate signal. We find that the exchange signal is captured effectively by the model presented here.

6.2 Mechanistic insights into model parameters

As noted in the introduction, there are a number of theoretical approaches to mechanistically describe calcite dissolution that are derived from classical crystal growth theory (Burton et al., 1951; Lasaga, 1998; Steefel and Van Cappellen, 1990; Zhang and Nancollas, 1990). In the analysis of their experiments, Naviaux et al. (2019a), applied the framing used by Dove et al. (2005) for quartz dissolution in terms of the retreat of atomic steps on the mineral surface.

The Dove et al. (2005) formulation for dissolution via step retreat, defect-assisted etch pit formation and homogenous etch pit formation (with increasing solution undersaturation, respectively) is described in Equations 16 and 18. For dissolution proceeding via the formation of etch pits, (by defects or homogeneously), the overall dissolution is given by:

Eq. 16) $$\ln\left(\frac{R_D}{(1-\Omega)^{\frac{2}{3}}|\sigma|^{\frac{1}{6}}}\right) = \ln\left(h\beta C_e(\omega^2 h n_s a)^{\frac{1}{3}}\right) - \frac{\pi\alpha^2\omega h}{3(k_b T)^2}\left|\frac{1}{\sigma}\right|$$

Where h is the step height (m), β is the step kinetic coefficient (m/^{2}), ω is the molecular volume (m^3), n_s is the density of active nucleation sites (sites/m^2), a is the lattice spacing (m) , α is the step edge free energy (mJ/m^2), k_b is Boltzmann's constant, T is the temperature in Kelvin and C_e is the mineral solubility. Here, the left-hand side of the equation is the normalized dissolution velocity, where R_D denotes the surface normal dissolution rate in m/s and σ is:

Eq 17) $$\sigma = \ln(\Omega)$$

Dissolution that proceeds by the retreat of existing steps on the mineral surface (near equilibrium mechanism), follows a different formulation:

Eq. 18) $$\ln\left(\frac{R_D}{(1-\Omega)^{\frac{2}{3}}|\sigma|^{\frac{1}{6}}}\right) = \ln\left(\frac{\omega\beta m h}{P}\right) + ln\left((1-\Omega)^{\frac{1}{3}}\left|\frac{1}{\sigma}\right|^{\frac{1}{6}}\right) - \ln\left(1 + 8\left(\frac{\omega\alpha}{Pk_bT}\right)\left|\frac{1}{\sigma}\right|\right)$$

Where, *P* is the perimeter of the screw dislocation that is the source of the existing steps and m is the number of elementary steps (equal to 1). The values *h, ω, a, P,* and *m* are all assumed constants, specific to the calcite crystal structure. The terms C_e, T, Ω and sigma are all defined relative to a given experiment. This leaves the fundamental unknowns: *β*, n_s and *α*.

The utility of the Dove et al. (2005) approach is that bulk dissolution rate measurements, when collected at sufficient resolution across a range of undersaturation, can be inverted for energetic and structural properties of the mineral surface that are otherwise accessible only by direct imaging like AFM. It converts a rate curve into a quantitative statement about step edge free energy and defect density, and thereby into a mechanistic interpretation of what limits dissolution. But, as noted above and illustrated by the presence of Ω and sigma in equations 16, 17, this necessarily enforces an Ω dependence on the measured parameters.

The model presented here does not require Ω dependence on the three free parameters. While G_{off}, R and S do not map directly onto Dove surface energetic parameters, we can interpret them within the same conceptual framework that describes mechanistic transitions as a function of undersaturation.

6.2.1 Reactive surface

The reactive sites term, *S*, represents the size of the solid reservoir capable of participating in gross dissolution and precipitation reactions. This parameter reflects the number of reactive surface sites available for ion attachment and detachment. Calcite surface sites may be classified geometrically (e.g., acute and obtuse step edges, kink sites, dislocations) or chemically (e.g., >Ca^+ and >CO_3^- surface sites). In the present model, all reactive sites are treated equivalently and are assumed to participate in gross forward and reverse fluxes with equal probability and kinetics. Similarly, the reactivity of ^{12}C and ^{13}C sites are treated identically (see equations in Sections 3.3). This assumption simplifies the treatment of isotope exchange and future work could explicitly consider crystallographic site types or isotope-specific kinetics.

To facilitate comparison across experiments and materials with different surface areas, the reactive site abundance is expressed as a surface-normalized site density (mol/m^2). This representation allows direct comparison across the different calcite materials used in the Naviaux et al. (2019a) experiments and with other studies of calcite surface reactivity and kinetics. As

noted above (and shown in **Figure 11**), there is a strong, nonlinear dependence of reactive site density on undersaturation that is qualitatively consistent with the Dove et al. (2005) framework's consideration of nucleation site densities.

Near equilibrium, the reactive site density exhibits little dependence on undersaturation. In the Dove framework, close to equilibrium dissolution proceeds through the retreat of existing steps on the mineral surface. In this regime, the density of reactive steps is thought to reflect an intrinsic property of the crystal surface rather than the external solution chemistry itself (Lasaga and Luttge, 2001; Zhang and Nancollas, 1990). Consistent with this interpretation, the fitted reactive site densities for all temperatures fall on approximately the same value near equilibrium, suggesting that temperature does not influence the amount of existing reactive surface sites in this regime. This behavior is observed for Ω values corresponding to the step retreat regime identified by Naviaux et al. (2019) (Ω ≈ 1–0.9 for the 12, 21, and 37°C experiments and Ω ≈ 1–0.75 for the 5°C experiments).

At greater undersaturation, reactive site density increases systematically with increasing (1-Ω). For the 12, 21, and 37°C experiments, this increase corresponds to the defect-assisted etch pit regime identified for calcite by Naviaux et al. (2019) at Ω ≈ 0.9-0.75 or homogeneous formation of etch pits at Ω < 0.75. In this framework, increasing undersaturation promotes the opening and propagation of etch pits, thereby increasing the number of reactive surface sites available for dissolution. As noted in **Section 4**, we lose sensitivity to this parameter at very high undersaturations.

Overall, these modeled trends and descriptions deriving from crystal growth theory are supported by direct observations of calcite surface evolution. In seawater, specifically, Dong et al. (2020) quantified calcite step velocities and etch pit densities during dissolution in seawater solutions at varying undersaturations in AFM measurements. Their experiments showed minimal etch pit formation within the step retreat regime, followed by a sharp increase in etch pit density within the defect-assisted dissolution regime and eventual transition toward pervasive surface roughening at far-from-equilibrium conditions. Similar transitions in freshwater AFM measurements have by made by Teng (2004).

Measured etch pit densities span $10^{10.4}$–10^{12} 1/m^2 in seawater (Dong et al., 2020) and $10^{9.8}$–$10^{12.7}$ 1/m^2 in freshwater (Teng, 2004). We emphasize that these etch pit densities—denoted n_s in the Dove framework—are not directly comparable in magnitude to our reactive site density S. A nucleated pit is not a single reactive site but a generator of steps and kinks, and the number of sites created per pit depends on pit size, depth, and edge morphology in ways that are not well constrained. The AFM images in Teng (2004) illustrate the difficulty: at the micron scale, pits of widely varying size are visible, including pits nucleated within older pits. Some have well-defined geometries with smooth edges, while others have jagged, serrated edges that likely host many reactive sites. Any mapping from n_s to S would therefore require assumptions about pit geometry that AFM snapshots alone cannot supply.

The magnitudes of n_s and S are not directly comparable but their dependence on undersaturation can be. Both Dong et al. (2020) and Teng (2004) measured pit densities across a range of undersaturations up to Ω ~ 0.82. **Figure 12** compares the undersaturation dependence of n_s from these studies with the fitted S from our model, with the difference in absolute magnitude noted by the two separate x-axes.

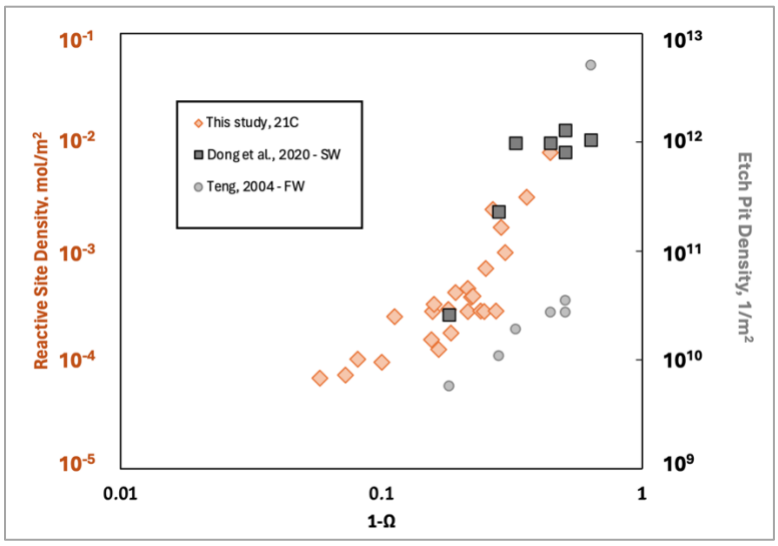


Figure 12. The undersaturation dependence of site density (orange diamonds) and etch pit density from the seawater AFM experiments of Dong et al., 2020 (dark grey squares) and the freshwater AFM experiments of Teng, 2004 (light grey circles). The left y-axis corresponds to the magnitude of the site density term, and the right y-axis corresponds to the magnitude of the etch pit density term. The alignment of the two axes does not indicate any particular relationship between site density and etch pit density. The key information here is that the two terms change by comparable orders of magnitude and at similar values of undersaturation.

As noted by Dong et al. (2020), the value of n_s increases sharply at the Ω_{crit} predicted from bulk dissolution experiments. Near $\Omega \approx 0.75$ in seawater, etch pit density increases by nearly two orders of magnitude, corresponding to the transition from defect-assisted to homogeneous pit nucleation. In freshwater, the same mechanistic transition occurs at $\Omega \sim 0.007$ (Teng, 2004) but also captures a roughly two orders of magnitude increase in etch pit density. Independently, our model requires an increase in S of comparable magnitude at $\Omega_{crit} \sim 0.75$. In both the AFM observations and the model fits, the transition is nearly step-like, sharper than the changes in slope we observe in the net rate or in our other fitted parameters. The correspondence between AFM and modelled surface behavior suggests that *S* is tracking a real physical property of the dissolving surface, not a mechanistically undefined fitting parameter.

6.2.2 Magnitude of site densities

The reactive site densities inferred from the model converge to approximately 10^{-4} mol/m^{2}under near-equilibrium conditions at all temperatures investigated. We interpret this convergence as setting a baseline or inherent reactive surface reservoir of the calcite materials used in the Naviaux et al. (2019a) experiments. Notably, this value is large. Based on considerations of crystal geometry, van Cappellen et al. (1993) estimated the site density of an idealized single crystallographic monolayer of calcite at approximately $10^{-5.1}$ mol/m^2. Our model derived estimates of *S* exceed the one-monolayer estimate by a factor of ~10. In other words, the fitted S corresponds to roughly ten monolayers worth of crystallographic sites per unit of BET-measured surface area.

Several independent studies support a reactive reservoir that extends beyond one crystallographic layer. Harrison et al. (2022) found that one monolayer was insufficient to reproduce the magnitude of isotope exchange observed during their experiments. Their model instead required participation of 2–7 monolayers of calcite. In another study, Subhas et al. (2017) used secondary ion mass spectrometry (SIMS) depth profiles to demonstrate that isotopic label could penetrate 2–

6 monolayers into calcite surfaces after exposure to both slightly supersaturated and slightly undersaturated seawater. Our fitted value of ~10 reactive monolayers is at the upper end of the estimates of Harrison et al. (2022) and Subhas et al. (2017), but on the same order of magnitude.

The observation of a large reactive surface reservoir may be based in mineral geometry. Calcite surfaces possess microscopic roughness and topographic complexity that may not fully captured by BET surface area measurements. BET measurements are inherently static and can be thought of as a "snapshot" of surface area when a mineral is under stable conditions. This is a fundamentally different regime than when a mineral is actively dissolving.

Additionally, the structure of the calcite–water interface is dynamic rather than crystallographically static. Experimental and theoretical studies have demonstrated mobility of both surface species and topographic features on calcite at low temperatures (Davis et al., 1987; Fenter et al., 2000; Kendall and Martin, 2007; Stipp, 1998). Surface restructuring, step migration, dissolution/precipitation and lattice relaxation may contribute to redistribute species within the outer monolayers of the mineral. Stipp (1998), for example, showed that impurity ions can be "mixed" to depths approaching ~10 monolayers during post-reaction surface reorganization associated with evolving surface topography. Under this interpretation, the reactive reservoir is not a static geometric feature but a continuously refreshed near-surface volume participating in mineral–fluid exchange.

The interpretations above treat surface reactivity as fundamentally geometric and sit within the Dove et al. (2005) framework. In contrast, in the surface complexation modeling (SCM) literature, surface reactivity is defined chemically. The reactive reservoir is the population of surface sites (e.g. $>Ca^+$, $>CO_3^-$) available to participate in adsorption and desorption reactions (e.g. Pokrovsky and Schott, 1999; van Cappellen et al., 1993). Classical SCM treatments assign a single site density and uniform reactivity, but more recent work has begun to merge the chemical and geometric perspectives by assigning distinct complexation behavior to specific site types and step geometries (e.g. Andersson and Stipp, 2012; Wolthers et al., 2008).

Molecular dynamics simulations of the calcite–water interface extend this chemical view further. Simulations by Wolthers et al. (2008, 2012) show that calcite surfaces in aqueous environments have highly structured hydration layers in which up to three water molecules can simultaneously coordinate individual surface calcium and carbonate groups. Ion attachment and detachment are mediated through this extended adsorbed-water network rather than occurring at a crystallographic surface. If the reactive layer is defined chemically as a population of hydrated, exchangeable surface complexes and adsorbed species, then the effective reservoir naturally exceeds simple crystallographic site-density estimates. In this view, our fitted S measures the size of the chemically active interfacial region in which the crystallographic surface is the boundary.

Although the mechanism responsible for the large site density is not uniquely identified from our data, multiple independent lines of evidence indicate that the effective reactive reservoir of calcite in aqueous systems is larger than a single crystallographic monolayer. Whether this arises from topographic complexity, dynamic restructuring, an extended hydrated interfacial region, or some combination, the implication is that the crystallographic site-density estimates are likely a lower bound on the surface reservoir available for dissolution.

6.3 Gross and net dissolution rates

The gross dissolution rate, G_{off}, exhibits a strong, nonlinear dependence on undersaturation that follows the same transitions observed in the reactive site density term (Section 6.1). The

transitions in G_{off} correspond closely to the critical saturation states identified by Naviaux et al. (2019a) that mark shifts in the dissolution mechanism. The consistency across the Naviaux et al. (2019a) Ω_{crit} values and those estimated here for G_{off} and S indicate that these values denote real physical processes rather than model parameterization artifacts.

Close to equilibrium, gross dissolution rates have a weak dependence on undersaturation (reaction order n ~ 0) at all studied temperatures. This result is distinct from the net dissolution reaction order being zero. Our updates to the Naviaux et al. (2019a) datasets show that the net rate exhibits a low, but non-zero, undersaturation dependence for the slowest experiments.

Naviaux et al. (2019a) could not resolve thermodynamic parameters in the near-equilibrium regime at 12, 21, and 37 °C because regression using **Equation 17** requires high data density in this Ω range. Because our parameters are fit to data from individual experiments, we can parse the relative contributions of surface reactivity (S) and gross rate (G_{off}) in the observed $\delta^{13}C$ evolution on a per-experiment basis.

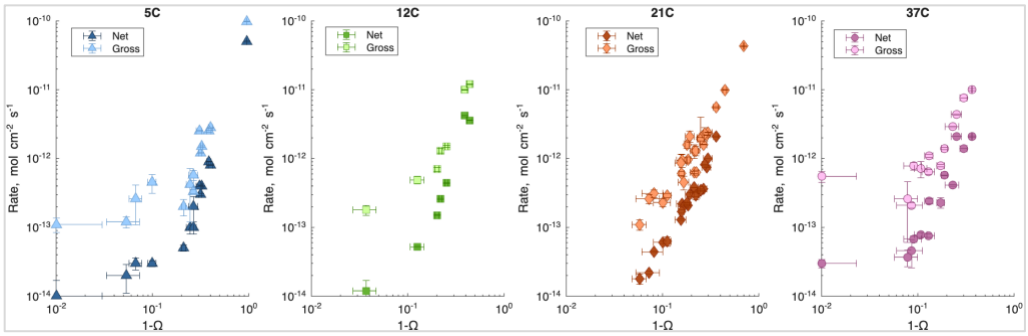


Figure 13. Net dissolution and gross dissolution rates for 5°C (a), 12°C (b), 21°C (c) and 37°C (d) as a function of undersaturation. Lighter markers are gross dissolution, and darker markers are net dissolution.

Despite the weak Ω dependence within the near-equilibrium regime, there is a systematic offset in the absolute magnitude of G_{off} with temperature: gross dissolution rates at 37°C exceed those at 5°C by up to an order of magnitude over the same range of undersaturations. This is in contrast to the site density term, which collapses to a common value near equilibrium at all temperatures (**Section 6.1**). Near equilibrium, these two terms illustrate that the temperature dependence of the net rate near equilibrium is driven by changes in the magnitude of the gross rates, not by changes in the reactive surface reservoir. This is consistent with the reactive surface in the step-retreat regime being an inherent property of the specific calcite grains used in the Naviaux et al. (2019a) experiments.

Comparison of the gross and net rates in **Figure 13** shows one of our central results: close to equilibrium, gross dissolution exceeds net dissolution by up to an order of magnitude. The offset means that even when the net signal is small, the surface is being actively recycled. This near-equilibrium exchange flux may represent something like a baseline overturning frequency of the calcite surface in seawater. In other words, an inherent rate of surface turnover persists regardless of solution thermodynamic driving force.

The behavior of gross and net close to equilibrium (in conjunction with the *R* results**, Figure 11**) also tells us that the influence of gross precipitation increases as a solution moves towards equilibrium. This reframing has consequences for how near-equilibrium dissolution experiments are interpreted. The kinetics and mechanisms of gross precipitation (nucleation and attachment at

step and kink sites) may be as important to near-equilibrium dissolution experiments as they are to precipitation experiments. A complete kinetic description of the calcite–seawater system near equilibrium will require the gross fluxes to be characterized on both sides of $\Omega = 1$, and the isotope tracer approach demonstrated here provides a direct means of doing so.

6.4 Implications

Surface complexation modeling (SCM) is widely used for describing the chemical reactivity of mineral surfaces, with applications spanning environmental remediation, contaminant transport and natural resource recovery. The foundation of SCM's is the assignment of relative proportions of chemical species that adsorb to surface sites. This requires a definition of the total number of sites available to participate in reactions. The earliest calcite SCMs (e.g., Van Capellen et al., 1993; Pokrovsky et al., 2000) adopted crystallographic site densities that assume perfect cleavage surfaces and a single reactive monolayer (Section 6.2.2). More recent formulations have incorporated topographically distinct site populations with site-specific reactivities (e.g., Wolthers et al., 2008; Andersson and Stipp, 2012).

Our results indicate that the reactive site inventory should be larger than the crystallographic site densities and that it is omega dependent. Whether or not the absolute magnitude of our site term is correct, its undersaturation dependence is robust and consistent with both direct AFM measurements of etch pit densities (Dong et al., 2020; Teng, 2004) and the predictions of classical crystal growth theory (Section 6.2.1). In the parameterization of SCM's, the site density should be considered dependent on the undersaturation, rather than a static value.

Our model results also have direct consequences for how diagenetic alteration is considered in carbonate proxy systems. We find that gross dissolution and precipitation fluxes near equilibrium routinely exceed net rates by up to an order of magnitude (Section 6.2). A carbonate grain in a pore fluid at $\Omega = 0.95$, for example, may show negligible net mass loss over geologic time but its reactive surface reservoir may turn over rapidly through gross exchange. The isotopic and trace-element composition of that reservoir can therefore re-equilibrate with pore fluid on timescales substantially shorter than those implied by net rates. Further, the reservoir subject to such exchange may itself be an order of magnitude larger than a single crystallographic monolayer, meaning correspondingly more material is available for alteration.

The temperature dependence of gross rates carries additional implications for the depth and latitudinal patterns of diagenetic alteration in marine sediments. Because gross dissolution rates increase by up to an order of magnitude between 5 and 37°C near equilibrium (Section 6.2.1), carbonates buried in warm, shallow sediments should experience faster surface exchange than those in cold deep-sea environments, all else being equal (Edgar et al., 2013).

Our results suggest that saturation state and temperature act as separable controls: Ω governs the balance of the gross fluxes (and hence the net behavior), while temperature sets the absolute speed of surface turnover even when that balance is unchanged. Two pore-fluid systems at identical Ω but different temperatures could drive isotopic and trace-element re-equilibration at rates differing by up to an order of magnitude.

7. Conclusions

Net rates calculated by the present model agree well with the majority of the net rates reported by Naviaux et al. (2019a), confirming that a finite, non-zero timescale is required for the reactive mineral surface to reach isotopic steady state. However, the original assumption that this

timescale is at most 24 hours breaks down close to equilibrium. For the slowest experiments, isotopic steady state may require days to weeks, longer than the original experimental durations. In these cases, the net rate is poorly constrained, and additional measurements would be needed to resolve it. This finding is consistent with the conclusion of DePaolo and Zhang (2025) that longer-duration experiments are necessary to constrain the slowest rates in the Naviaux dataset.

The model reproduces the complete shape of the $\delta^{13}C$ time series, including the initial nonlinear behavior, using only a gross dissolution rate (*Goff*), a gross rate ratio (R = *Gon* / *Goff*), and a reactive surface site abundance (S). We do not need an additional exchange term is required to capture the raw data. The curvature in $\delta^{13}C$ versus time arises naturally from the progressive isotopic evolution of the surface reservoir as initially ^{13}C-enriched sites are replaced by material of mixed isotopic composition through gross dissolution and precipitation.

Both S and *Goff* exhibit strong, nonlinear dependence on undersaturation (the dependence exists but it noisier for R), with breakpoints at the same critical Ω values that Naviaux et al. (2019a) identified from net rate measurements as transitions between dissolution mechanisms. This correspondence is notable because no thermodynamic driving force or rate-law assumptions are embedded in our approach—the transitions emerge entirely from the structure of the $\delta^{13}C$ data. The convergence of independently derived breakpoints provides mutual validation of the surface energetic framework of Dove et al. (2005) as applied to calcite dissolution in seawater.

Near-equilibrium site densities are $\sim 10^{-4}$ mol/m^2 at all temperatures, roughly an order of magnitude larger than the density calculated for a single monolayer ($\sim 10^{-5.1}$ mol m^{-2}; Van Capellen et al., 1993). The presence of a large reactive surface reservoir is corroborated by a number of independent studies (Subhas et al., 2017, Harrison et al., 2022; Gehin et al., 2021, Wolthers et al., 2008, 2012). These observations support the description of the calcite surface as a dynamically reorganizing region rather than a static single-layer boundary.

Gross rates near equilibrium are up to an order of magnitude faster than net rates, meaning the mineral surface exchanges far faster than bulk mass loss would suggest. Carbonates in near-equilibrium pore fluids may undergo meaningful alteration of their isotopic and trace-element signals through gross exchange, without net mass loss.

Further work should focus on the near-equilibrium regime with longer experiments and high-density sampling to characterize the gross rate ratio and net rate where they are currently least constrained. The physical basis for the large reactive site density is unclear and would benefit from coordinated, surface characterization (AFM, VSI, SIMS) and isotope tracer experiments. Finally, translating the gross rate framework developed here into quantitative predictions of proxy re-equilibration timescales under realistic burial conditions—as a function of temperature, saturation state, and grain geometry—represents the most important extension of this work, with direct relevance to the fidelity of carbonate archives over geologic time.

Chapter 3. Novel measurement of calcite dissolution kinetics in marine porewaters

1. Introduction

Carbonate sediments operate as a natural buffer to changes in atmospheric CO_2 via carbonate compensation, the process by which $CaCO_3$ sediments dissolve in response to acidifying ocean conditions, subsequently releasing alkalinity and rebalancing ocean pH (Archer et al., 1998; Broecker and Peng, 1987). This process plays an important role in buffering ocean pH against modern CO_2 emissions (Archer and Maier-Reimer, 1994; Montenegro et al., 2007) and in the natural cycles of ocean CO_2 and alkalinity over glacial-interglacial periods. The timescale of carbonate compensation is therefore essential to understanding both modern and past climate change. The combined effects of CO_2 solubility, overturning circulation, bioturbation and dissolution kinetics themselves set this response time (Archer et al., 1998; Zeebe and Zachos, 2013). The dissolution kinetics component is generally described in terms of a rate law in the form:

Eq. 1) $$\text{Rate} = k(1-\Omega)^n$$

This description is purely an empirical one and historically, there has been disagreement as to how to fit the reaction order *n* and the kinetic coefficient *k* (Hales and Emerson, 1997; Honjo and Erez, 1978; Keir, 1980). Discrepancies in the fits to *k* and *n* exist between different experimentalists and between laboratory and field studies.

In recent years, there has been an effort to ground the rate law in mechanistic terms, rather than the empirical fitting approach. Subhas et al. (2015) developed a novel method using isotopically labeled calcite to precisely measure dissolution rates near equilibrium, where a large portion of marine environments reside.

This approach enabled a thermodynamic description of the specific surface processes that control the rate of dissolution as a function of undersaturation following classical crystal growth theory (Chernov, 1984; Malkin et al., 1989). Subhas et al. (2015), Dong et al. (2018), Naviaux et al. (2019) employed this framework to describe dissolution rates as controlled by (1) step retreat at existing sites on the mineral surface close to equilibrium, (2) by defect-assisted etch pit formation farther from equilibrium, and (3) by homogeneous etch pit nucleation very far from equilibrium. This framework has proven effective for describing calcite dissolution in seawater with varying temperature and pressure and is supported by direct AFM measurements (Dong et al., 2020). Additionally, Naviaux et al. (2019b) extended these experiments to the water column, finding good agreement with the classic study of dissolution of calcite spheres in the Pacific by Peterson, 1966.

Despite this extensive body of work, no study has yet directly measured calcite dissolution *in situ* in sedimentary porewaters, where most dissolution in the modern ocean is thought to occur (Broeker and Peng, 1987; Archer et al., 1989). This gap fuels ongoing debate in the literature as to whether laboratory and water column derived rate laws can be applied directly to sediments (Boudreau et al., 2020; Sulpis et al., 2017).

Quantifying dissolution rates *in situ* in porewaters can help disentangle the relative contributions of phenomena such as the benthic diffusive boundary layer (Santschi et al., 1991; Sulpis et al., 2017) and respiration-driven dissolution (Archer et al., 1989; Emerson and Bender, 1981) to alkalinity fluxes at the seafloor. Understanding these alkalinity fluxes has direct implications for defining the shape of the calcite lysocline and constraining the timescale of carbonate compensation.

Building on the porewater dataset of Cetiner et al. (2025, 2022), we present novel calcite dissolution experiments performed *in situ* within these same sediment porewaters. By combining direct, isotopically labeled dissolution rate measurements with high-resolution porewater chemical profiles at the same stations and depths, this approach allows us, for the first time, to directly attribute measured *in situ* dissolution rates to specific porewater chemical processes, rather than relying on chemical profiles alone. These observations, in turn, lets us probe some of the most pressing questions in the ocean's alkalinity cycle: the timescale of ocean carbon cycling, the role of respiration-driven dissolution in setting alkalinity fluxes, and how nonlinear dissolution kinetics shape the depth and form of the lysocline.

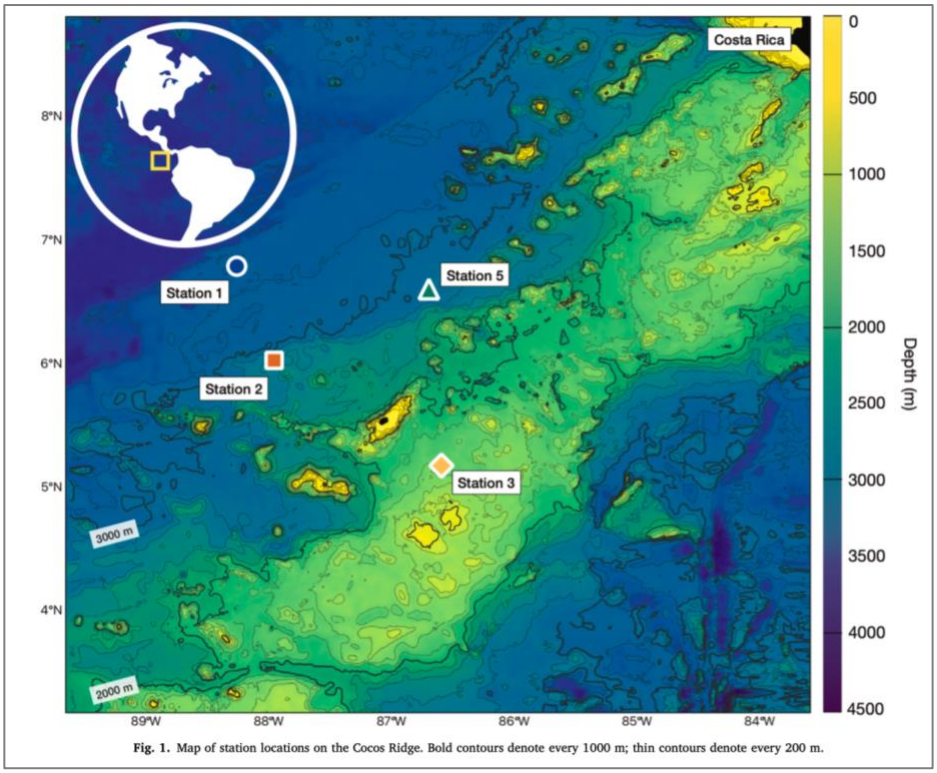


Fig. 1. Map of station locations on the Cocos Ridge. Bold contours denote every 1000 m; thin contours denote every 200 m.

Figure 1. Locations of stations studied along the Cocos Ridge. Station 1 – CR1 blue circle. Station 2 – CR2 orange square. Station 3 – CR3 green triangle. Station 5 – CR5 yellow diamond. The same symbols used to denote the station identities here are consistent throughout the figures in this paper. Colormap denotes water depth.

2. Methods

2.1 Study site

The measurements and experiments described in this study were collected in December 2021 aboard the R/V Sally Ride in the Eastern Equatorial Pacific, at stations along and adjacent to the Cocos Ridge. Station-specific details, including the measurements and experiments performed at each site, are listed in **Table 1**; a map of the study area is shown in **Figure 1**. A detailed description of the study sites, including sediment characterization and porewater chemistry, is provided in Cetiner et al. (2025, 2022). We reproduce the porewater profiles from Cetiner et al. (2025) in **Figure 2**, as these previously published results are directly relevant to the description and discussion presented here.

Table 1. Location, physical and chemical description of SIPR stations

Station ID	Station coordinates	Water depth, m	Sediment description	Porosity range, %	Core top carbonate content, %	BW Ω	BW O_2
CR1	6° 47.080 N, 88° 15.650 W	3223	Low carbonate clay	84-94	0.8	0.84	105
CR2	5° 57.480 N, 87° 57.400 W	2650	Medium carbonate clay	78-88	63	0.94	100
CR3	5° 10.170 N, 86° 35.590 W	1630	High carbonate clay	74-83	78	1	75
CR5	6° 35.990 N, 86° 41.750 W	2911	Medium carbonate clay	81-93	13	0.89	100

2.2 Dissolution experiments

Our porewater calcite dissolution experiments use the same *in situ* porewater sampler (SIPR) described in Cetiner et al. (2022, 2025), originally developed for natural porewater sampling. A schematic of the setup when deployed at the seafloor is shown in **Figure 3**. We first describe the porewater collection mechanism, then describe the modifications made to conduct *in situ* calcite dissolution experiments.

In brief, the SIPR consists of a "blade" that filters porewater *in situ*, attached to a standard MC-800 multicore. After deployment from the ship, the multicore lands on the seafloor and drives the blade into the sediment. The blade has eight "windows," spaced along its length, that serve as sampling ports at different sediment depths. Each blade window is connected via Tygon tubing to a quartz coil (internal volume 30 mL), which is connected via additional tubing to a spring-loaded syringe (60 mL) initially held closed. After the multicore is deployed and after a designated settling time on the seafloor, the spring-

loaded syringes are released, drawing porewater from the sediment through a filter [0.45um pore size, Pall Supor filter] into the blade window then into the quartz sample coil. Prior to recovery of the multicore, a "pinch" mechanism compresses the tubing, preventing additional water uptake as the device travels back through the water column to the ship.

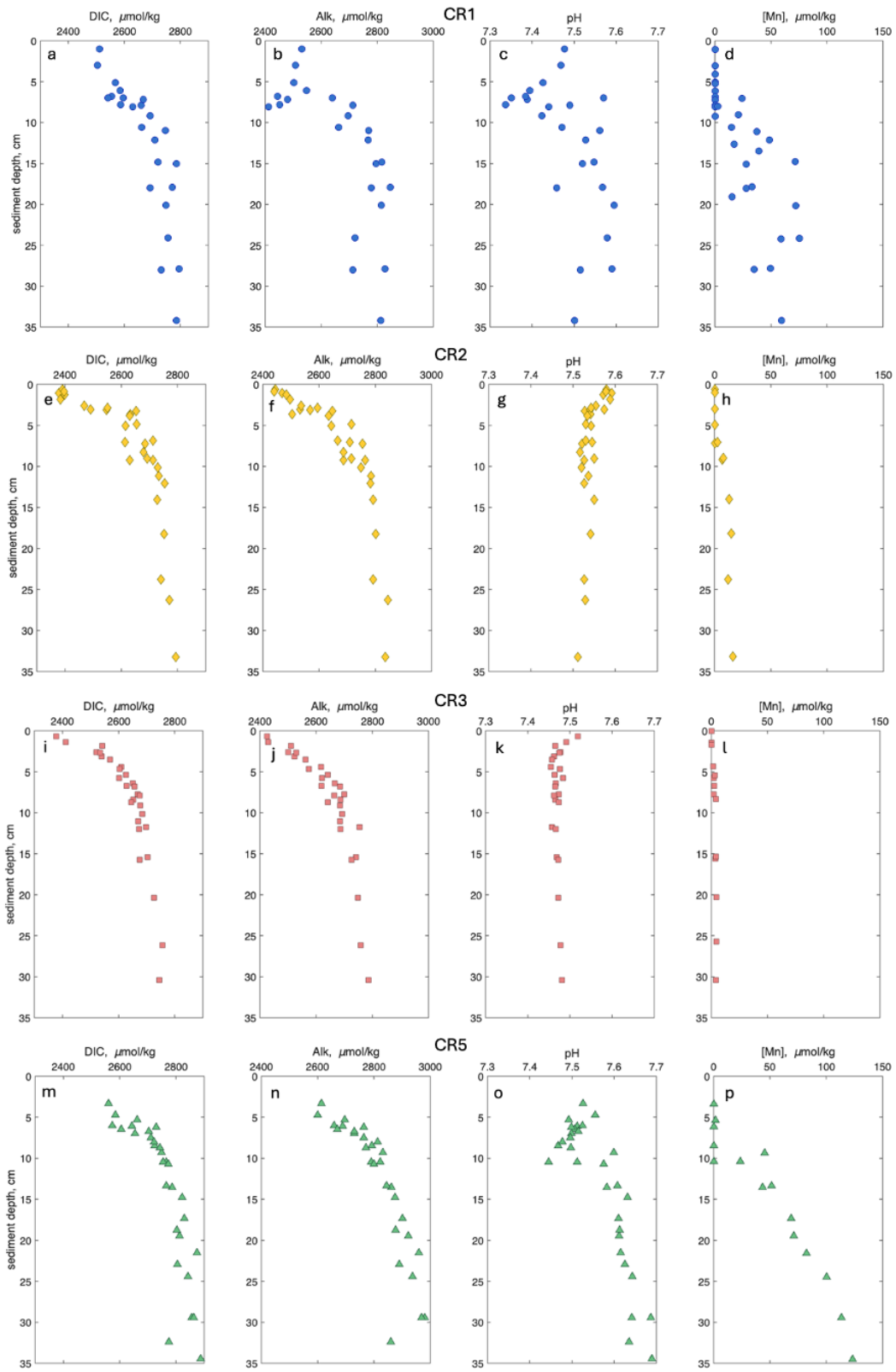


Figure 2. Porewater chemistry profiles reproduced from Cetiner et al. 2025. DIC, alkalinity, pH and [Mn2+] for (a-d) CR1, (e-h) CR2 (i-l) CR3 and (m-p) CR5.

All tubing lines, quartz coils and blade windows are pre-filled with a fill solution consisting of filtered surface seawater spiked with fluoride. This fill solution prevents tubing collapse under seafloor pressure. The fluoride spike also allows us to quantify the extent to which the fill solution mixes with porewater, since porewater displaces this fill volume in the system during collection.

Upon return to the ship, the quartz sample coils are isolated from the rest of the system by closing and disconnecting the three-way valves between (1) the blade and the coils and (2) the coils and the syringes. The coils are placed in cold storage 4C until sampling, at most 2 hours.

in situ calcite dissolution experiments use the SIPR apparatus with the following modifications. The filters in the blade windows are replaced with a filter "bag" containing 5–10 mg of isotopically labeled $Ca^{13}CO_3$. The bags are constructed by heat-sealing two filter papers together, leaving one side open for the labeled grains to be added, then sealing the final side (see sample draw schematic in **Figure 3**).

For the dissolution experiment setup, only one side of the blade is open to the porewater, in order to slow the flow rate past the grains and limit dilution of the dissolution signal. A 30 mL draw-volume limit is also imposed on the dissolution experiment windows, ensuring that the full isotope-label/dissolution-rate signal is collected within the 30 mL quartz coil. In other words, no water that reacted with the labeled grains was drawn past the coil into the unsampled auxiliary tubing or syringe. An underwater video camera (Group B Inc.) and light were mounted in pressure housings on the multicore and pointed at the dissolution experiment syringes to determine the flow rate of each experiment.

A dissolution experiment is considered "started" the instant porewater is drawn into the blade window. An experiment ends either when the 30 mL maximum is reached or, if less than 30 mL is drawn, when the coils are pinched at the end of the deployment.

2.2.1 Dissolution experiment sampling

As discussed in Subhas et al. (2015, 2017) and Chapter 2, the isotopically labeled dissolution method produces a time-sensitive isotope signal, arising from the system's evolution toward isotopic steady state from an initial condition that is inherently unbalanced (pure ^{13}C solid, ~99% ^{12}C seawater). We likewise expect a nonlinear, time-resolved ^{13}C signal within our experiments, and therefore divide the water in each coil into discrete, approximately time-resolved subsamples, following the approach below.

Samples are collected from the "bottom" of the quartz coil, where the coil attaches to the blade, and are therefore nearest the most recently drawn water. A 1–2 mL aliquot is collected first to flush the three-way valve and the short length of Tygon tubing connecting the coil to the valve; this aliquot is discarded.

The remaining water in the coil is then collected in four discrete aliquots of roughly 7–8 mL each. For each aliquot, water is slowly drawn from the coil into a syringe, taking care

to avoid introducing air bubbles; the syringe contents are then shaken to homogenize, filtered, and distributed among vials for measurement of (1) DIC and $\delta^{13}C$ of DIC, (2) alkalinity, (3) fluoride concentration, and, in some cases, (4) silica.

This process is repeated for each subsample. Because sampling proceeds from the blade end of the coil, the first subsample collected, denoted "a", corresponds to the water most recently in contact with the labeled grains, i.e., the water present at the end of the experiment. Subsequent subsamples denoted "b," "c," and "d," are collected progressively toward the syringe end of the coil, with "d" corresponding to the first plug of porewater that was drawn past and reacted with the grains at the start of the experiment. Coil geometry and subsample labelling are illustrated in **Figure 3**.

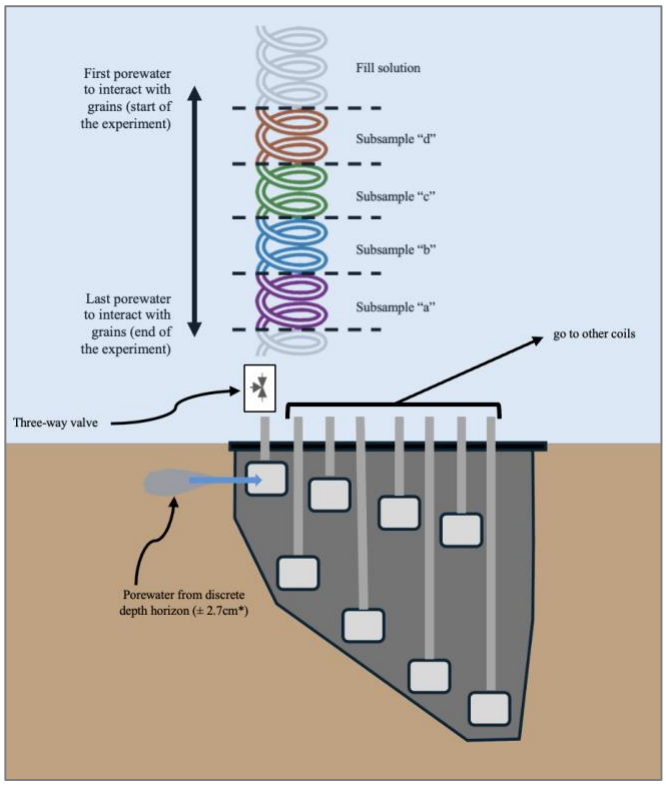


Figure 3. Schematic of a blade deployed at the seafloor and an example of how the sample coil is divided for subsampling. The sediment is denoted by the brown background, and the overlying water is denoted by the light blue background. The blade is shown in dark grey, with nine sampling windows represented in light grey. The sampling windows are positioned at staggered depths below the sediment-water interface. There is internal routing that connects each blade window to a three-way valve, which it connected to the quartz sample coil (example shown for just one blade window/valve/coil). Above the sample coil is another three-way valve, tubing and a syringe (not pictured – see Cetiner et al. 2022, 2025 for details). The blade window collects water from a given depth and the ~2.7cm above and below, shown here as the blue "halo" of collected porewater (not to scale).

2.3 Measurements

Measurement methods for DIC and $\delta^{13}C$ of DIC, alkalinity, fluoride, and silica are described in detail in Cetiner et al. (2022) and summarized briefly here. The DIC and $\delta^{13}C$ of DIC were measured using a Picarro Cavity Ring-Down Spectrometer (G2131i) with Dickson seawater as a DIC standard and Iceland spar as a $\delta^{13}C$ standard. Total alkalinity and pH were measured spectrophotometrically using a mvMICA system described in Liu et al. (2006, 2011). Dissolved manganese was measured using an Agilent 8800 triple-quadrupole ICP-MS, calibrated using commercial multi-element standard solutions matrix-matched to artificial seawater. Fluoride concentrations were measured using an Orion fluoride-specific electrode. Dissolved silica was measured following the spectrophotometric molybdenum blue method described in Parsons et al. (1984).

2.4 Ω Calculations

Calcite saturation state for natural porewater samples is calculated using CO2SYS (MATLAB v3.1.1; Lewis & Wallace, 1998), using pH and alkalinity measurements. Each calculation is specific to the pressure and temperature at the corresponding station. We use the total pH scale, with K1 and K2 constants from Hansson (1972, 1973) and Mehrbach et al. (1973), as refit by Dickson & Millero (1987), and the calcite K_{sp} from Mucci (1983).

Only DIC and alkalinity (not pH) are measured on the dissolution-experiment subsamples, and DIC carries relatively large uncertainty, driven in part by the small sample volumes allocated to this measurement from each subsample. As a result, Ω values calculated directly from the experiment subsamples propagate to very large uncertainties. We instead interpolate Ω from the more precise natural porewater samples (those without labeled grains) to the depths of the dissolution experiments, using a Gaussian process regression (MATLAB *fitrgp* function) to define a smoothed Ω profile at each station. This approach has limitations where the Ω profile exhibits sharp curvature, addressed in Section 5.3.

2.5 Critical undersaturation identification

We use changes in the slope of the rate vs. 1- Ω relationship to define transition in the mechanism controlling dissolution. To find statistically meaningful changes in slope we use the approach of Muggeo (2003) for estimating regression parameters with unknown breakpoints. The approach consists of testing all known measurements as candidate breakpoints and comparing the two resulting regressions against the fit of a single regression through the data. We enforce the condition that the two regression lines must intersect. We propagate error though the calculation following a Monte Carlo strategy, each time the breakpoint test is run, the rate and Ω data are perturbed within their measured standard deviations.

3. Model

3.1 Reaction model

The model presented here for interpretation of the *in situ* dissolution experiment data is a modified version of the model in Chapter 2. An illustration of the model is shown in **Figure 4**. There are two reservoirs considered explicitly in the model: (1) a bulk reactive reservoir and (2) a mineral surface reservoir. The former represents the volume within the heat-sealed filter bag where the labeled grains reside (~0.1mL). This is the water that may directly interact with the labeled grains via gross dissolution (G_{off}) or gross precipitation (G_{on}). We consider the remainder of the blade window volume (surrounding the heat-sealed region of the filter bags) to be a non-reactive volume, that simply operates to dilute the signal collected from the reactive volume. The reactive mineral surface reservoir represents the total number of "active" sites on the mineral surface that may participate in gross dissolution or gross precipitation, denoted S (molecules). The size of this reservoir is constant over the course of an experiment. During net dissolution, the number of surface sites is held constant by the replacement of removed material with material from the interior of the grain (pure ^{13}C).

An aqueous diffusive boundary layer above the grains is not explicitly considered in the model. We find that the $\delta^{13}C$ and net rate signal is not sensitive to the absence or presence of a DBL until it reaches a thickness of ~500 μm, which corresponds to the average size of the reactive aqueous reservoir inside the heat sealed grain bags.

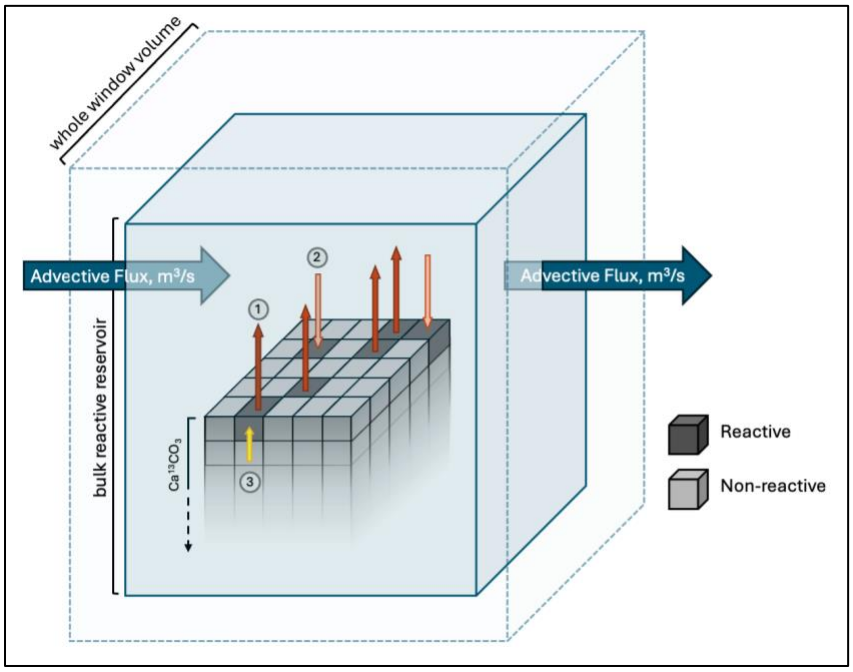


Figure 4. Schematic of the box model for advection and reaction in our experimental system. The calcite grain is represented by the grey cubes, where an individual cube represents a single unit cell of calcite. The reactive sites, those that may participate in gross dissolution and gross precipitation (dark and light orange arrows, respectively), are shown in dark grey unit cells and nonreactive sites shown in light grey. As the reactive sites are removed, new ^{13}C is supplied from the bulk material (yellow arrows). The

volume of the whole blade widow is shown as the dashed box. Inside the volume is the reactive aqueous volume. The mineral grains only directly interact with the reactive volume. An advective flux defined by the flow rate in a given experiment passes through both aqueous reservoirs at a constant rate.

The model includes an advective flux that represents the flow of pore water past the grains during an experiment. Porewater is pulled into and exits the whole window (reactive + nonreactive volumes) at a constant rate. We model the instantaneous composition of the reactive aqueous and reactive surface reservoirs following **Equations 2-4**.

Eq. 2) $\frac{d[^{13}C]_{aq}}{dt} = [\ FR * \ (G_{off} \ * \ F^{13}_{R.Surf} - \ \ (G_{off} * R) \ * \ F^{13}_{bulk}\ )\ ]\ /\ v_{aq}$

Eq. 3) $\frac{d[^{12}C]_{aq}}{dt} = \left[FR * (\ G_{off} \ * \left(1 - F^{12}_{R.Surf}\right) - \left(G_{off} * R\right) * \ (1 - F^{12}_{bulk}))\ \right]\ \ /v_{aq}$

Eq. 4) $\frac{d(n^{13}C_s)}{dt} = (G_{off} * R) * \ F^{13}_{bulk} - \ \ G_{off} * \ \ F^{13}_{R.Surf} + \left(G_{off} - \ G_{off} * R\right) * F^{13}_{B.Solid}$

where $[^{13}C]_{aq}$ and $[^{12}C]_{aq}$ are the instantaneous concentrations (molecules/m^3) of ^{13}C and ^{12}C in the reactive aqueous reservoir and $n^{13}C_s$ and $n^{12}C_s$ are the instantaneous number of molecules of ^{13}C and ^{12}C in the reactive mineral surface reservoir. FR is the measured flow rate (m^3/s), v_{aq} is the volume of the reactive aqueous reservoir and G_{off} and G_{on} are the gross dissolution and gross precipitation fluxes (molecules/s), respectively. Note that based on the mass balance we impose in the surface reservoir, it would be redundant to explicitly model the ^{12}C in the surface. The overall size of that reservoir is held constant at the value set by the size of *S* and any change in its ^{13}C composition is necessarily compensated by a change in ^{12}C composition.

The fraction terms in Equations 1-3 represent the instantaneous fraction of ^{13}C or ^{12}C in each of the reservoirs and are defined in Equations 5-9.

Eq. 5) $F^{13}_{bulk} = \frac{[^{13}C]_{aq}}{DIC}$

Eq. 6) $F^{12}_{bulk} = 1 - \ F^{13}_{bulk}$

Eq. 7) $F^{13}_{R.Surf} = \frac{n^{13}C_s}{n_s}$

Eq. 8) $F^{12}_{R.Surf} = 1 - F^{13}_{R.Surf}$

where the DIC is set by its value in the porewater that is drawn into the window (here, in terms of molecules/m^3) and *S* is the total number of molecules of reactive sites on the mineral surface.

To calculate the concentration of ^{13}C and ^{12}C in whole window volume, the following dilution factor is applied:

Eq. 9) $\left[^{13}C\right]_{window} = \left[^{13}C\right]_{aq} f_{r,v} + \left[^{13}C\right]_{bakcground}\left(1 - f_{r,v}\right)$

where $f_{r,v}$ is the fraction of the total window volume taken up by the reactive aqueous reservoir. This concentration represents the solution drawn into the sample coil. It is converted to $\delta^{13}C$ following:

Eq. 10) $$\delta^{13}C = \left(\frac{^{13}R_{sample}}{^{13}R_{PDB}} - 1\right) * 1000$$

The model is initialized to the ^{13}C and ^{12}C composition of the fill solution that initially sits in the blade window, prior to the start of an experiment. This assumes that the fill solution is retained in this reservoir upon deployment and not flushed with water column water as the multicore travels through the water column.

Under ideal conditions, the reactive mineral surface is initially pure ^{13}C. In practice, the labeled grains we use in our experiments are exposed to supersaturated fill solution and, potentially, water column water prior to the start of an experiment. As such, the isotopic composition of the grain surfaces may be shifted away from pure ^{13}C due to exchange or even net precipitation. The choice of initial surface composition is therefore non-trivial and likely not 100% pure ^{13}C. We test three treatments of the initial surface condition: (1) high initial surface ^{13}C, (2) low initial surface ^{13}C and (3) initial surface composition as a free parameter.

3.2 Mixing model

The reaction model produces a time resolved signal in $\delta^{13}C$, that, under perfect plug-flow conditions, would be unmodified along the length of the sample coil. In practice, as the reacted water in the blade window is pulled into the sample coil, it experiences turbulent mixing that both (1) mixes fill solution into the reacted water near the fill solution/sample interface and (2) smooths the time resolved dissolution signal.

There are two options for treating the data to address the potential for mixing of the sample water over the course of an experiment. This first is to apply a simple fill solution correction to the data. For each subsample a fluoride measurement is made that can be translated into a % of fill solution in the sample following Equation 14:

Eq. 14) $$\%\ FS = ([F]_{sample} - [F]_{background}) / ([F]_{fs} - [F]_{background})$$

Where $[F]_{background}$ is the concentration of fill solution in the background porewater pulled into the window during an experiment, $[F]_{fs}$ is the concentration of fluoride in the spiked fill solution and $[F]_{sample}$ is the fluoride concentration in the measured subsample that represents a mixture of the previous two. The calculated %FS can then be applied to the measured $\delta^{13}C$ signal to correct for dilution by mixing with the lower $\delta^{13}C$ value of fill solution.

This simplified approach is limited in the sense that it only considers dilution of the $\delta^{13}C$ signal by mixing with the fill solution. In the case of a constant $\delta^{13}C$ over an experiment/across all subsamples, this approach would be sufficient for accounting for

mixing in the system. However, because there is a non-linear signal of $\delta^{13}C$ with time/distance along the coil, the mixing that occurs influences the distribution of $\delta^{13}C$ with distance along the coil independent of its interaction with fill solution.

To account for this, we use a 1-D model to define an effective mixing coefficient using the fluoride spike as a tracer. Notably, we do not explicitly consider advection in this model. The advection in our system (flow rate) is constant over the course of an experiment, such that the fill solution/sample interface moves at a constant rate along the length of the sample coil, independent of the mixing. This has no practical impact on the mixing and therefore we can consider the fill solution/sample interface a stationary reference point about which mixing occurs.

We use a basic diffusion model, Equations 15 - 16, but instead of a molecular diffusion coefficient for fluoride ions in seawater, we define a mixing coefficient D (m^2/s) as free parameter fitted to the fill solution data.

Eq. 15) $$J_{i+\frac{1}{2}} = \frac{-D*\left([F]_{i+1} - [F]_i \right)}{dx_{i+\frac{1}{2}}}$$

Eq. 16) $$\frac{d[F]_i}{dt} = \frac{\left(J_{i-\frac{1}{2}} - J_{i+\frac{1}{2}} \right)}{dx_i}$$

Here, J is the Fickian-type flux across the interface between two discrete model boxes, $[F]_i$ is the fluoride concentration in each box in mol/m^3, and dx_i is the spacing between adjacent interfaces. The spacing corresponds to the degree of discretization of the system. The mixing model is run using MATLAB's *ODE15s* stiff solver for the duration of the experiment. The initial condition in the model is a step function representing 100% FS in the first half of the coil, and 0% FS in the second half. The output of the model is [F], mol/m^3 versus experiment time.

Once D is defined relative to a specific experiment, we apply the mixing model to the output of the reaction model. In this application, we set up an initial condition in a "synthetic" model coil defined by the isotopic composition of the fill solution that sits adjacent to the isotopic composition of the reaction model output. This requires transforming the reaction model output from a function of time to a function of length in the coil, simply the product of the flow rate and time. Equations 15 and 16 are modified from mixing fluoride to mixing ^{12}C and ^{13}C. The mixed model output is then discretized and integrated over the volumes corresponding to each subsample in a given experiments in order to directly compare to the measured $\delta^{13}C$ values of the subsamples.

3.3 Optimization

We used the Matlab function *lsqnonlin* to optimize the fits to the three free parameters: the gross dissolution rate (G_{off}, molecules/s), the gross rate ratio ($R = G_{on}/G_{off}$) and the number of reactive surface sites (n_s, molecules). These parameters are optimized between values of 10^7-10^{18} molecules/s, 0.001-1 and 10^{10}-10^{20} molecules, respectively. For each realization of the model the parameters are held constant (i.e., not a function of time).

The algorithm runs the reaction model then the mixing model and uses the integrated model output corresponding to the $\delta^{13}C$ of each subsample to calculate a "score" in the form of Equation 17 that describes how well the model matches the data, where lower residual scores reflect better fits to the data.

Eq. 17) $$Residual = \frac{1}{2}\sum_{i=1}^{N}(\delta^{13}C_{model}^{i} - \delta^{13}C_{measured}^{i})^2$$

To reduce sensitivity to initial parameter guesses and propagate analytical uncertainty, a Monte Carlo strategy was employed. For each experiment, 500 independent optimization runs were performed using random initial parameter values drawn from the allowed ranges. For each realization, measured $\delta^{13}C$ values were perturbed assuming a normal distribution with a standard deviation of 0.15‰. The resulting ensemble of accepted solutions defines the uncertainty distributions for fitted parameters. Further, optimization runs were retained only if *lsqnonlin* reported successful convergence ("Exit Flag 1" in *lsqnonlin*) and the final misfit fell below a prescribed threshold.

4. Results

4.1 Ω interpolation

The results of the Gaussian Process Regression for smoothing Ω depth profiles for each station are shown in **Figure 5**. The Ω at the sediment-water interface is set by the measured overlying water Ω value. The GPR fit can be limited where there is sharp curvature in the depth profile. For the stations we studied, this is most prominent at station CR1 and CR5, where there is a sharp decrease in Ω ~5-10cm depth in the sediment. The GPR, in these cases, tends to predict low values of Ω. This has potential implications interpreting dissolution rates at these depths, as noted in **Section 5.1.**

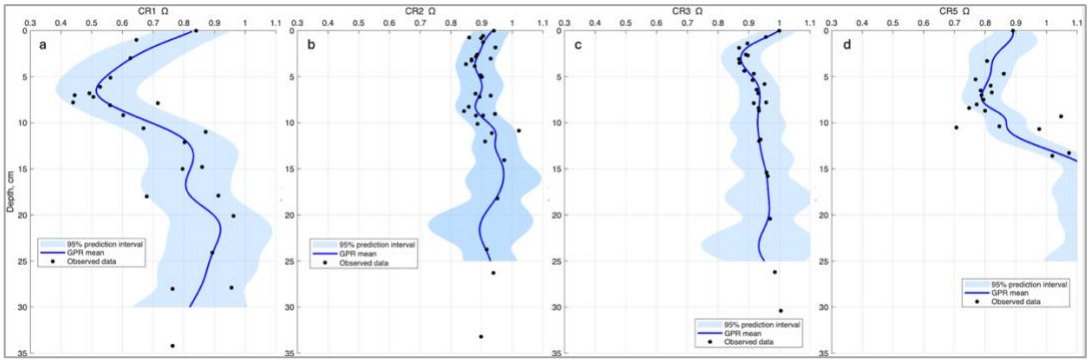
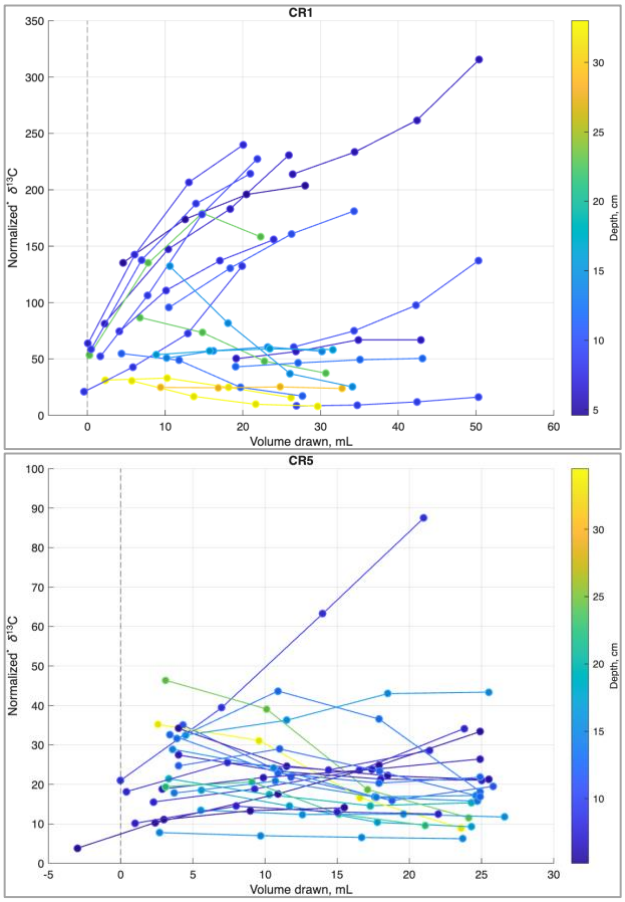


Figure 5. Results of GPR for Ω determination at experiment depths for (a) CR1, (b) CR2, (c) CR3 and (d) CR5. The Ω values calculated from the background porewater chemistry are shown as black dots. The result of the GRP is shown as a solid blue line. There 95% confidence interval is shown as the shaded blue region. Note that regions with large confidence intervals generally correspond to where there is low data density or noisy data.

4.2 Experiment data

The rawest form of our experimental data is $\delta^{13}C$ v. time or volume. We assign each subsample from a given experiment a "distance," in mL, from the fill solution/sample interface (0mL in Figure 6). We normalize the $\delta^{13}C$ data to the mass and flow rate specific to each experiment in order to compare trends in the magnitude of the dissolution signal across different experiments and stations. This version of our data is plotted in Figure 6, where each point is a subsample and groups of four points connected by a line represent an experiment. The "d" subsample is always the first point on a line segment, closest to the fill solution/sample interface (0mL), and represents the start of an experiment. The "a" subsample sits at the end of a line segment (usually at 25mL +) and represents the end of an experiment.

In Figure 6, the points reflect the "mid-point" of each subsample volume. The most accurate visual description of the data would be a horizontal line centered at each subsample point in Figure 6 that corresponds to the total volume of each subsample (typically ~8mL). Note that some "d" subsamples are centered very near 0mL or less than 0mL. In these cases, the subsample included water we estimate to be on the fill solution side of the fill solution/sample interface.



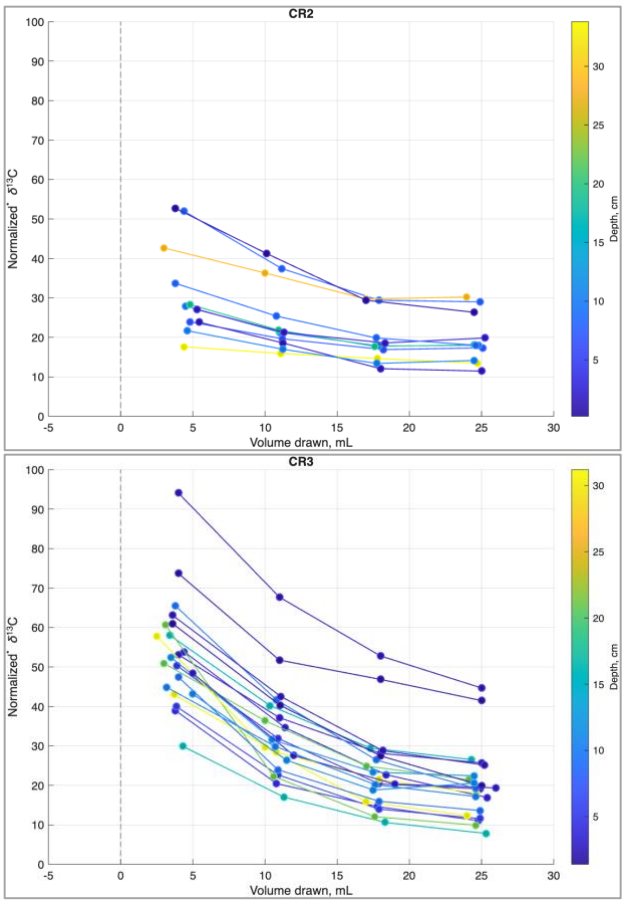


Figure 6. For each station, the $\delta^{13}C$ data from all experiments. The a, b, c and d subsamples for a given experiment are represented by points connected by a line. The dashed line at 0 on the x-axis represents the idealized fill-solution/sample interface. The "d" subsample is closest to the fill-solution/sample interface and represents the start of an experiment. The "a" subsample is furthest from the interface and represents the end of an experiment. The color coding denotes the depth in the sediment at which the experiment was performed.

Overall, there are two general trends in the $\delta^{13}C$ v. volume data that we denote Type 1 and Type 2. Type 1 (T1) data is exemplified in stations CR2 and CR3 (with some examples at CR1 and CR5) and is characterized by a $\delta^{13}C$ signal that deceases as it moves away from the sediment water interface. This means that the first water to react with the grains, at the start of the experiment, has a higher $\delta^{13}C$ than the last water to react with the grains, the end of the experiment. In these experiments, the $\delta^{13}C$ signal appears to plateau towards the end of the experiment, noted by the shallow slope between the b-a subsamples relative to d-c. For most of the experiments that follow this trend, the $\delta^{13}C$ value of the "a" subsample sits between 10-30‰. This is an order of magnitude larger $\delta^{13}C$ signal than the background porewater $\delta^{13}C$ value (reported in Cetiner et al., 2025).

We characterize Type 2 (T2) data as increasing in $\delta^{13}C$ signal with distance from the fill solution/sample interface. These data tend to sit at overall larger $\delta^{13}C$ values than the T1

data and can reach normalized $\delta^{13}C$ values of up to 300‰, indicating a large signal of dissolution. We only observe T2 data at stations CR1 and CR5, which have lower bottom water Ω values than CR2 and CR3. At CR1 and CR5, the T1 appear to be dependent depth in the sediments (color bar in Figure 6) – they largely occur shallower than ~15cm sediment depth.

4.3 Mixing coefficient fits

The mixing coefficients fitted to the fill solution data for each experiment are reported in Table A1 and plotted as a function of the flow rate of the same experiment. Intuitively, as the flow rate increases, the extent of mixing in the sample coil increases. Note that each station sits within a relatively well-defined range of flow rates and therefore mixing coefficients. The correlation between flow rates and station ID is related to the physical sediment properties at each station. CR1 and CR5 have the lowest carbonate content, have more clay and therefore have lower porosity, making it more difficult to pull porewater through the sediments and into the coils. Stations CR2 and CR3 have higher carbonate content and porosity, resulting in easier collection of porewaters.

At CR2, CR3 and CR5 cameras record the rate at which the syringes move allowing us to precisely measure the flow rate for each experiment. The depth of station CR1 is greater than the pressure rating on our camera set up, meaning that our flow rates are not precisely measured, but estimated based off the draw volume read off of the syringe after the multicore is retrieved and divided by the known draw time. We exclude experiment that draw the maximum volume as we cannot know when the max volume was reached.

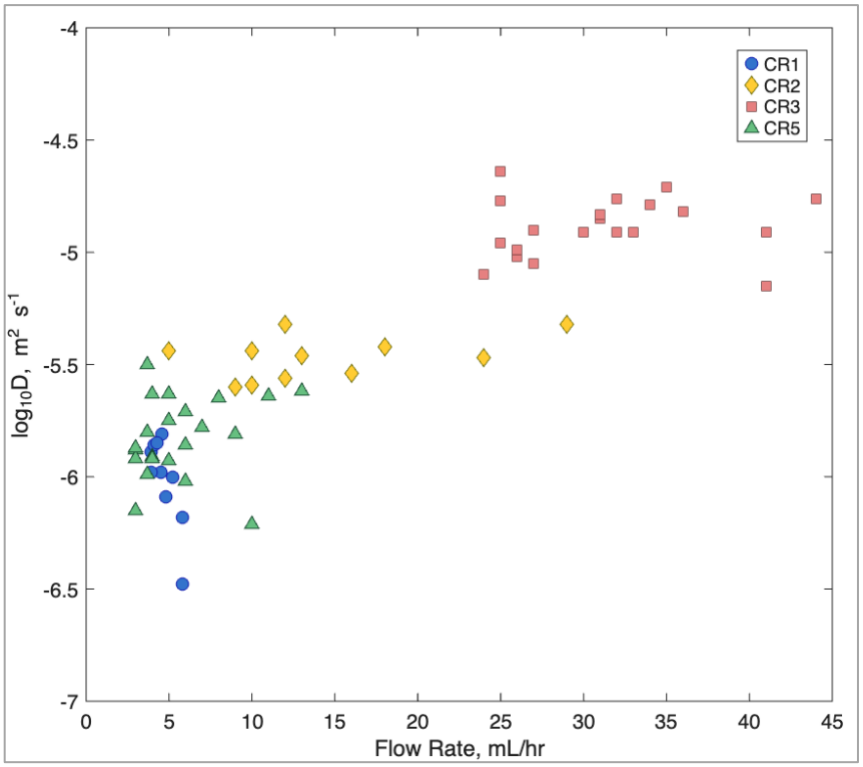


Figure 7. Fitted mixing coefficients (logD, m^2/s) as a function of experiment flow rate for CR1 (blue circles), CR2 (yellow diamonds), CR3 (red squares) and CR5 (green triangles). For comparison, molecular diffusion is on the order of 10^{-9} m^2/s.

4.4 Reaction model fits

We present two example model outputs that illustrate the behavior of the model in fitting the three free parameters, Go_{ff}, R, and S. The continuous model output, parameter covariances and histograms are presented in **Figure 8** and **9** and discussed. In all future discussion and text, we converted the units of G_{off} to the surface area normalized rate ($moles/cm^2/s$) and S to the surface site density ($moles/m^2$). All of the models discussed have been passed through the mixing model such that the $\delta^{13}C$ vs time curves and parameter fits are performed on the mixed reaction models.

4.4.1 T1 model fits

The structure of the T1 models follows an initial spike in $\delta^{13}C$ and a subsequent decay to a constant $\delta^{13}C$ value, which is greater than the background porewater $\delta^{13}C$. The initial spike is consistent with dissolution moving ^{13}C from an initially enriched ^{13}C surface to solution. As a result, the initial spike captures information about the gross dissolution rate. As the experiment proceeds, some ^{12}C is added to the carbonate surface as the result of gross precipitation, shifting the composition of the reactive surface to a lower ^{13}C content. Eventually, the mineral surface will reach an isotopic steady state resulting from the balance of gross dissolution and gross precipitation fluxes and the composition of the $\delta^{13}C$ signal will be constant. The steady state signal is captured in the "plateau" portion of T1 experiments and is representative of net dissolution signal.

In **Figure 8**, we show the modeling results for an example experiment (ID: CR214). In panel a, the grey circles represent the measured data ($\delta^{13}C$ v. distance from the fill solution/sample interface), and the pink lines represent the best fit model output. The model output shown are for the combined reaction and mixing model. Each single blue line represents the $\delta^{13}C$ trend expected for a given set of optimized parameters (fitted G_{off}, R and S values). The model is effective at capturing the early peak in $\delta^{13}C$ that decreases and plateaus with distance from the fill solution/sample interface.

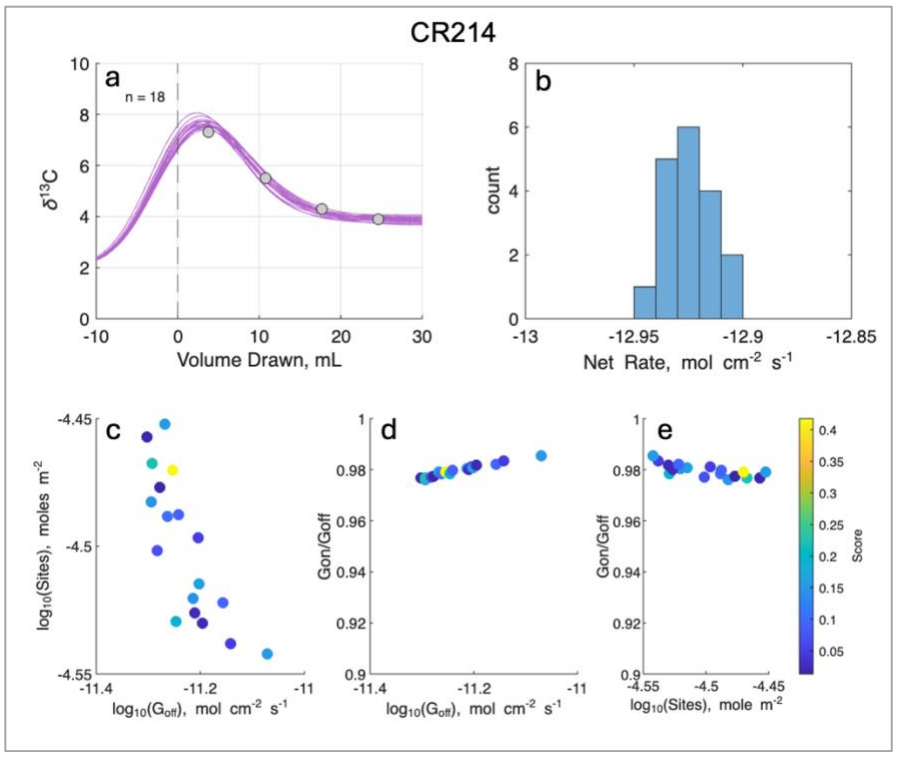


Figure 8. Example model output for experiment CR214. (a) Measured data for subsamples shown in grey circles. Model fits are purple lines. For this example, there are n=18 model fits that passed our filter for an acceptable fit (see text). (b) Histogram of net rates corresponding to the model fits in (a), calculated following **Equation 18**. (c-e) Cross plots of individual parameters for the fits presented in (a). The color bar represents the value of the residual score for each model/parameter combination.

The histogram in **Figure 8b** represents the net rates corresponding the model curves shown in **8a**, calculated following Equation 18:

Eq 18) $$Net = G_{off} * (1 - R) / (SA_{BET} * m)$$

Where SA_{BET} is the BET surface area in m^2/g and m is the mass of labeled grains used in an experiment in g. Note that the values for the net rate are very tightly constrained, for the average rate of 2 x 10^{-13} mol/cm^2/s, 2sigma is roughly 1 x 10^{-14} mol/cm^2/s, well within the error we would expect from a benchtop measurement of dissolution rate (Subhas et al. 2015).

Likewise, there are good constraints on individual parameters, that include covariances between them as seen in **Figure 8c-e**. The correlation between G_{off} and G_{on}/G_{off} is the most straightforward to interpret given the relationship between these parameters and the net rate. The strong correlation seen in Figure 7d falls on a line of roughly constant net rate and helps explain why the net rate (not explicitly optimized for in the model) is so well captured. The information contained in our measured d13C vs. volume signal places a strong constraint on the *in situ* net rate of CaCO3 dissolution, even while the individual gross fluxes vary more widely.

The reactive surface sites term, *S,* is not explicitly accounted for in the net rate term but is well constrained. It exhibits a negative correlation with both the gross dissolution rate (**Figure 8c**) and the gross rate ratio, R (**Figure 8e**). The covariation can be interpreted as modulating the size and timing of the $\delta^{13}C$ peak. A larger gross dissolution rate produces a larger initial $\delta^{13}C$ signal in solution. But for a small reactive surface reservoir, the amount of material the gross dissolution rate can operate on is smaller, resulting in a reduced $\delta^{13}C$ signal. As such, these parameters operate in different directions to modulate the $\delta^{13}C$ value of, primarily, the "d" subsample. The covariation between G_{on}/ G_{off} and *S* is related through the value of G_{off}. For smaller *S*, turning up G_{off} can maintain a spike in ^{13}C or turning down the contribution from G_{on} (via decreasing R) can also maintain that spike in ^{13}C. In other words, if S decreases, Goff rate must increase to get same d13C value in the water.

4.4.2 T2 model fits

T2 results are generally noisier and more variable than the T1 experiments, consistent with the large $\delta^{13}C$ values and the large absolute errors on individual $\delta^{13}C$ measurements. The errors for these experiments tend to be greater than for T1 experiments. This is illustrated in the higher residual scores **(Figure 9 c-e color bar**) and in the visual assessment of the model fits (**Figure 9a**)

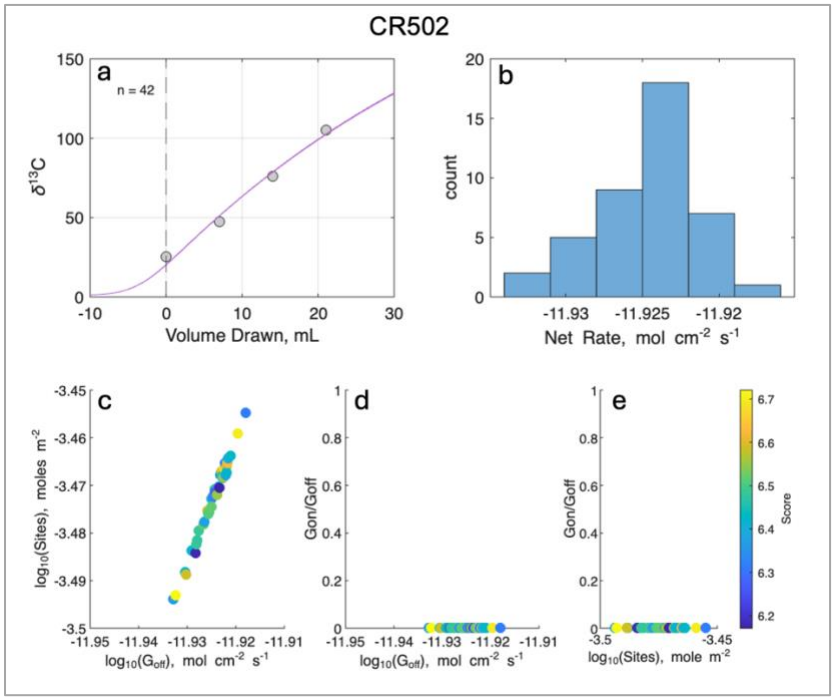


Figure 9. Example model output for experiment CR502. (a) Measured data for subsamples shown in grey circles. Model fits are purple lines. For this example, there are n = 42 model fits that passed our filter for an acceptable fit (see text). (b) Histogram of net rates corresponding to the model fits in (a), calculated following Equation 18. (c-e) Cross plots of individual parameters for the fits presented in (a). The color bar represents the value of the residual score for each model/parameter combination.

While the correlation behavior between parameters is markedly different here than for T1, the constraints on individual parameters are very tight. For *S*, compare the range of ~0.3 log units in T1 (**Figure 8**) to the < 0.05 range in T2. Likewise, the range for G_{off} here is ~0.01 log units and all the fits to G_{on}/G_{off} are pushed essentially to zero. These trends generally hold for all fits to T2 data.

The positive correlation between *S* and G_{off} likely arises from the model trying to fit high $\delta^{13}C$ values that increase slowly. As an endmember example, when G_{off} is large and *S* is small, the model curvature looks almost like a step function, even with a mixing component. The $\delta^{13}C$ signal rises steeply and plateaus early at a high $\delta^{13}C$ value. In order to get the "slower" transition to the max $\delta^{13}C$ value (i.e. shallower slope), a large reactive surface reservoir is invoked. Because of the way we formulate the initial surface composition as a faction of ^{13}C on the surface for a given initial surface composition of anything less than 100% ^{13}C, a larger surface reservoir means a larger total number of ^{12}C on the surface. A large number of ^{12}C on the surface means a longer timescale for even large Goff values to "dig" into the interior of the grain and reach the pure ^{13}C bulk solid. We discuss the sensitivity to initial condition in more detail below.

4.4.3 Sensitivity to initial surface composition.

The initial surface composition of the isotopically labeled grains influences the magnitude of the $\delta^{13}C$ signal at the start of the experiment and in the model. However, the isotopic composition of the mineral surface is dynamic, particularly at the start of an experiment, and will evolve regardless of it's starting composition. The final, steady state flux of material that comes off of the mineral surface is largely independent of the starting condition.

The model predicted net dissolution rate is largely insensitive to the choice of initial surface composition. We find that the net rate estimates for T1 models vary ~2% across initial surface compositions ranging from 1% ^{13}C to 100% ^{13}C. Type 2 models are more sensitive; they can vary by ~20% for the same range of initial surface conditions. The difference between the two model likely derives from the strong constraints on net rate imposed by T1 models and experiments. As noted above, much of the net rate signal resides in the "a" and "b" subsamples and in T1-type experiments, these impose a strong forcing on the model to meet this steady state/net rate condition. For T2-type experiments, the "a" and "b" subsamples do plateau as strongly as T1-type data, meaning they do not impose as strict of a forcing towards steady state and can be more sensitive to the starting model condition. Even given this sensitivity, the T2 models are strongly associated with fast net dissolution rates and a 20% uncertainty is small relative to the orders of magnitude that whole range of rates span.

The starting surface composition influences the curvature at the start of an experiment where much of the parsing between the relative contributions of individual parameters is decided. Individual parameters, therefore, can be highly sensitive to initial surface composition.

4.4.4 Difference from bench model

Trends in parameter covariance for T1 are largely consistent with the trend observed when using original version of the model (described in **Chapter 2**) for fitting benchtop dissolution experiments. One of the key differences between T1 fits and benchtop fits is the magnitude of the reactive surface sites term. For experiments in comparable undersaturation regimes, *S* is 1-2 orders of magnitude smaller in the experiments presented here.

One of the key results from modelling the benchtop experiments was that for very undersaturated and very slow dissolution rates (in particular, at low temperatures), the calcite surface can take on the order of 10 days to reach an isotopic steady state. This has important implication for the experimental set up of the benchtop experiments and illustrates limitation in the interpretation of $\delta^{13}C$ for short experiments. The experiments present here were performed for durations on the order of hours. We found that the advective component and small volumes used in the *in situ* experiments result in much faster timescales for the mineral surfaces to achieve isotopic steady state compared to the large volume, batch experiment approach on the bench.

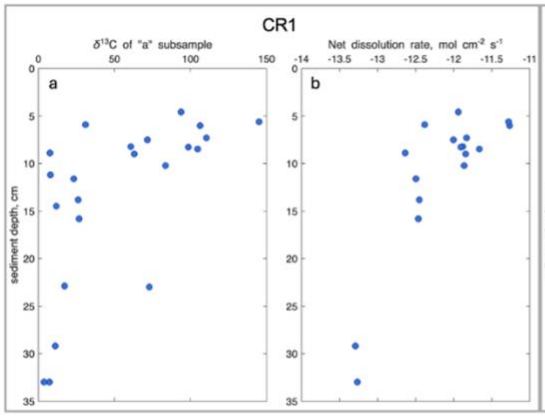


Figure 10. At CR1, (a) normalized $\delta^{13}C$ and (b) modelled net rate with depth in the sediment.

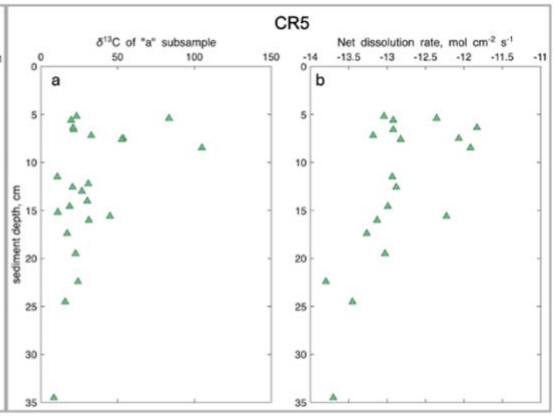


Figure 11. At CR5, (a) normalized $\delta^{13}C$ and (b) modelled net rate with depth in the sediment.

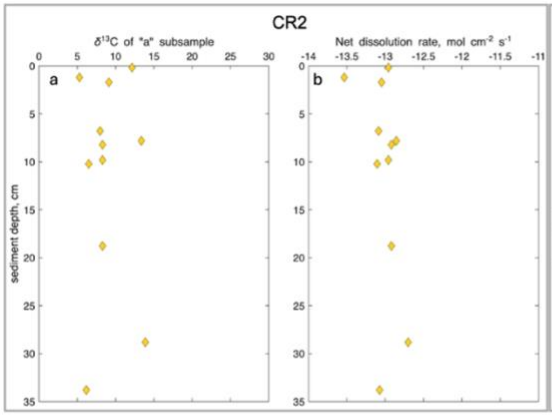


Figure 12. At CR2, (a) normalized $\delta^{13}C$ and (b) modelled net rate with depth in the sediment.

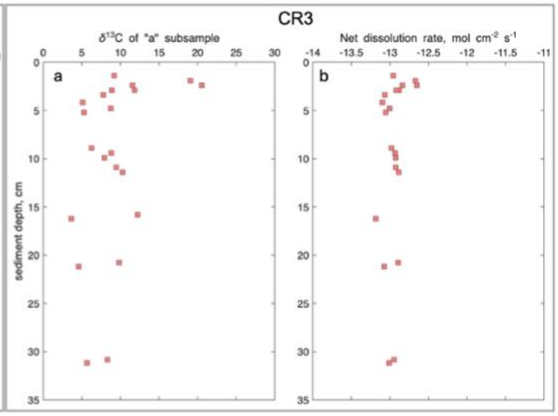


Figure 13. At CR3, (a) normalized $\delta^{13}C$ and (b) modelled net rate with depth in the sediment.

5. Discussion

5.1 In situ porewater rate law

In seawater at 21°C, the dissolution rate proceeds via three distinct mechanisms as a function of undersaturation: step retreat near equilibrium, defect assisted etch pit formation at intermediate undersaturations and homogeneous etch pit formation far from equilibrium (Naviaux et al., 2019a). As noted by Naviaux et al. (2019a), at 5°C, the defect assisted etch pit mechanisms is skipped and dissolution proceeds from step retreat to homogeneous etch pit formation as undersaturation increases.

Regardless of the mechanism, dissolution proceeds at topographical steps on the mineral surface. The difference between mechanisms is the source of those steps. Step retreat proceeds at steps inherent to the mineral surface (point defects and existing step edges) and homogeneous etch pit formation generates new reactive sites anywhere on the surface via the nucleation of etch pits. This framework builds on classical crystal growth theory (Chernov, 1984; Malkin et al., 1989), reframed for mineral dissolution by Dove et al. (2005) and is supported by benchtop and water-column observations of calcite dissolution across a range of temperature and pressure conditions (Subhas et al., 2015, 2019; Naviaux et al., 2019a; Dong et al., 2020).

The transition between mechanisms can be identified by a change in slope of the calcite dissolution rate law. The Ω at which this transition occurs is the "critical undersaturation", denoted Ω_{crit}. In benchtop experiments at 5°C, Naviaux et al. (2019a) noted the change from step retreat to homogeneous etch pit formation occurred at an $\Omega_{crit} = 0.75$. In water column dissolution experiments in the North Pacific at around 5°C, Naviaux et al. (2019b) noted that the Ω_{crit} occurred between 0.75-0.8, roughly the same as observed in the laboratory.

When all of our stations are considered together, we calculate that there is a statistically significant break in the slope of our rate data as a function of undersaturation at $\Omega_{crit} = 0.85 \pm 0.06$, following the method described in Section 3.4. This Ω_{crit} value is slightly closer to equilibrium than both the benchtop and water column experiments, but subject to large error bars. The fitting algorithm may be influenced by the gap in data around the Ω_{crit} value and the nearly vertical data from CR5. With respect to the former: the algorithm searching for the break in slope only gets evaluated at measured data points. The absence of rate measurements between $\Omega \sim 0.85$ and ~0.89, means the algorithm will never report an Ω_{crit} in that range. Likewise, the vertical structure of our CR5 data, which may be a relic of sediment compaction from the lander deployment itself (discussed in more detail below), may be driving shallower slopes and higher $\Omega_{crit.}$ If we only perform the breakpoint analysis on the CR1, CR2 and CR3 experiments, the Ω_{crit} sits $\sim 0.83 \pm 0.04$.

Alternatively, the shift in $\Omega_{crit.}$ may be a real feature of our results. The Naviaux et al. (2019b) water column experiments are also noisy and sit closer to $\Omega = 0.8$ than the $\Omega = 0.75$ value from the benchtop data (Naviaux et al. 2019a). Moving from the laboratory to the water column to porewaters represents a progressive pressure increase and

temperature decrease that may lead to a real, if small, shift of the Ω_{crit} towards equilibrium.

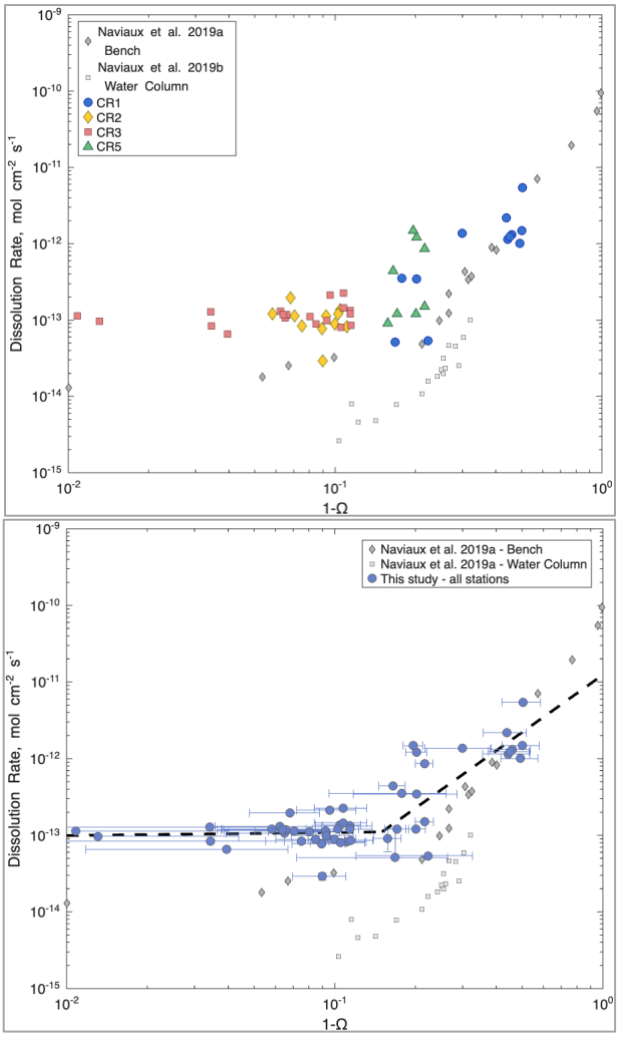


Figure 14. Modelled dissolution rates as a function of 1- Ω. In both panels, the grey diamonds are from the 5°C benchtop study of Naviaux et al. (2019a) and the grey squares are from the water column study of Naviaux et al. (2019b). In (a), CR1 data are blue circles, CR2 are yellow diamonds, CR3 are red squares and CR5 are green triangles. In (b), all *in situ* porewater experiments are shown as blue circles with their respective error bars, compared against the Naviaux et al. (2019a, 2019b) data. The dashed black lines in (b) denotes the fits to the York regressions through the *in situ* data for an Ω_{crit} of 0.85.

Even given the uncertainty in $\Omega_{crit,}$, the structure of the rate behavior as a function of undersaturation is consistent across all three environments. Dissolution rates are rapid with a strong undersaturation dependence far from equilibrium and slow with a much lower undersaturation dependence close to equilibrium (Figure 15). The large error bars, uncertainty in Ω and log-log scaling of **Figure 14** all conspire to indicate a 0^{th} order Ω dependence of our dissolution rates near equilibrium. However, a zero-order dependence of dissolution rate on undersaturation close to equilibrium is inconsistent with the

observations at comparable temperatures in both the laboratory (Naviaux et al., 2019a, refit in Chapter 1) and the water column (Naviaux et al., 2019b).

We turn instead to log-linear plots of the rate vs. undersaturation in **Figure 15** to identify if there is a trend in the rate with undersaturation in these close-to-equilibrium experiments. The experiments are color coded to the normalized $\delta^{13}C$ value of their respective "a" subsamples which is most reflective of the net dissolution rate. The correlation between the $\delta^{13}C$ of the "a" subsample and the modelled net rate indicates that the chemical signal of dissolution is being consistently translated by the model into rate information.

At CR3, there is a small but robust trend of decreasing rate and decreasing $\delta^{13}C$ with decreasing undersaturation. This is corroborated by the depth profiles at CR3 (**Figure 12, 13**) that show peaks in undersaturation at specific depths that coincide with elevated $\delta^{13}C$ values and elevated modeled net rates. When the Ω profile at this station is interpolated to assign Ω values to the experiment depths, the relatively small excursion in Ω is not effectively captured, even though we interpret it as a real signal. As a result, when the data are recast into a log(rate) vs. log(1–Ω) plot, this underlying signal can become obscured.

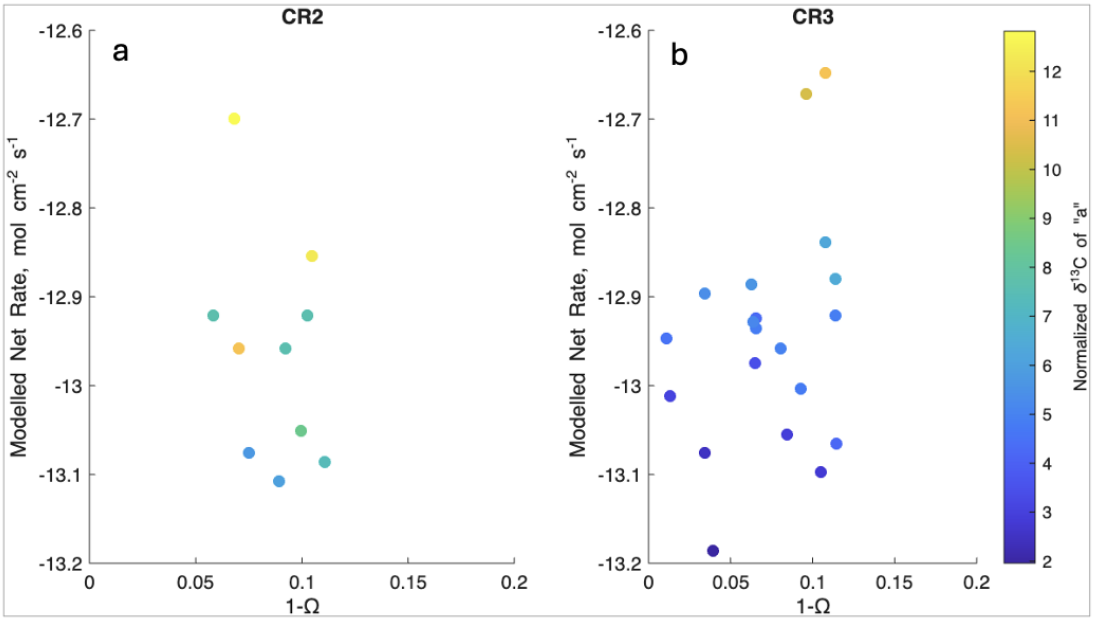


Figure 15. Zoomed in version of rate vs. 1- Ω plot for (a) CR2 and (b) CR3 experiments. The color bar denotes the normalized $\delta^{13}C$ value of the "a" subsample of each experiment. Higher rates have "hotter" colors, denoting larger steady state $\delta^{13}C$ signals.

At CR2 both the rate v. undersaturation plots (**Figure 15**) and the depth profiles are noisy. Here we interpret this behavior as true lack of structure in the Ω depth profiles and a tendency to sit very close to equilibrium at this site. As a result, we expect the size of the dissolution signal to be small and with correspondingly little structure.

As noted above, we think that a sampling artifact from sediment compaction arises in our CR5 data. During both deployments at this station, the multicore forced the blade deeper than expected into the sediment. The blade has a "retaining plate" that is meant to sit gently at the sediment-water interface while the blade is deployed in the sediment and collecting porewater. At CR5 the retaining plate was pushed ~3cm into the sediment. **Figure 14** shows a gap in samples in the 0–3 cm range which is a measure of how far the plate over-penetrated. We also have video evidence of the overpenetration from the cameras attached to the multicore. The effect of sediment compaction could be to mix and displace the porewater chemistry signal at those depths. However, the pH measurements and dissolution experiments may be uniquely capable of capturing this porewater disruption. The porewater samples of pH were collected from the first few milliliters of water in the coil after flushing the three-way value – analogous to the way we collected our "a" subsamples. The remainder of the porewater in the coil was homogenized for the alkalinity, DIC and other measurements. As the blade samples porewater, it retains some spatial information in the coil – i.e. the first water sampled is the porewater that was closest to the window. By discretizing the experiment sample coils and pulling the pH aliquot for the coil prior to homogenization, these measurements may hold some spatial information that could capture the displacement of the porewater caused by compaction. In pH, $\delta^{13}C$ and rate we see binary behavior at constant depths. Near ~10cm, pH measurements span almost 0.2 pH units and $\delta^{13}C$ and rate measurements both span an order of magnitude. This behavior may be capturing the effect of compaction disrupting the original chemical structure of the porewaters that has been smoothed out in the alkalinity and DIC sampling.

5.1.1 York fits

The calcite dissolution rate law, formulated as:

Eq 19) $$\log R = \log_{10}(k) + n\log_{10}(1- \Omega)$$

describes the rate of calcite dissolution in terms of a dissolution rate constant (k, mol/cm^2/s) and a reaction order, n (unitless). In order to properly capture the nonlinear undersaturation dependence, the rate law should be fit separately to each region of undersaturation where a specific mechanism of dissolution is operating. For the 5°C experiments reported here (and in Naviaux et al., 2019a, 2019b), we perform two York fits, reported in Table 2, that represent the step retreat regime and homogeneous etch pit formation regimen. We report these with the values from Naviaux et al. (2019a) 5°C benchtop experiments (refit in – Chapter 2) and the Naviaux et al. (2019b) water column experiments.

For the near equilibrium ($\Omega > \Omega_{crit}$, step retreat) regime in our new data we note two fits to the York regression in Table 2. The first fits of all of the data following the changepoint calculation, and results in a roughly 0th order dependence on undersaturation. In the second fitting, denoted in parenthesis in Table 2, we simplify the regression to two points that are the min and max rates and the minimum and maximum measured (not

interpolated) Ω values. This gives an endmember estimate of the fitted parameters that represents the strongest possible signal we may see, for example, in **Figure15b.**

Table 2. Summary of Ω_{crit}, rate law constant and reaction order for the benchtop experiments of Naviaux et al. (2019a), the water column experiments of Naviaux et al. (2019b) and this study.

			Step retreat $\Omega > \Omega_{crit}$		**Homogeneous Etch Pit** $\Omega < \Omega_{crit}$	
Study	**Environment**	**Ω_{crit}**	**$\log_{10}k$ (mol cm^{-2} s^{-1})**	**n**	**$\log_{10}k$ (mol cm^{-2} s^{-1})**	**n**
Naviaux et al. 2019a (refit by Barnhart et al., 2026)	Laboratory benchtop	0.8	-13.1 ± 0.2	0.43 ± 0.1	-10.2 ± 0.1	4.51 ± 0.1
Naviaux et al. 2019b	Water column, Northern Pacific	0.8	-13.5 ± 0.4	0.8 ± 0.5	-10.8 ± 0.4	4.7 ± 0.7
This study	Porewater, Eastern Equatorial Pacific	0.85 ± 0.06	-12.98 ± 0.16 (-12.92 ± 0.19)	0.03 ± 0.1 (0.43 ± 0.1)	-10.94 ± 0.4 (-10.96 ± 0.4)	2.69 ± 1.2 (2.49 ± 1.1)

In our experiments the rate coefficient estimates are around -12.9 and -10.9 for step retreat and homogeneous etch pit mechanisms respectively. For the step retreat mechanism, this value is very similar to the benchtop but about half an order of magnitude greater that the rate coefficient in the water column. In the homogeneous etch pit regime, the rate coefficient in porewaters is more similar to the value in the water column relative to the benchtop. The reaction orders shift between regimes: near equilibrium the reaction order may range from 0.03 to 0.43. The upper end of this range is comparable to the benchtop experiments of Naviaux et al. (2019a) that were refit in **Chapter 2**. Far from equilibrium the reaction order in porewaters is about 60% lower than in the laboratory or water column, indicating a much weaker dependence on undersaturation in this regime.

Taken together, the consistent structure of rate vs. (1–Ω) imply that a single mechanistic description of the processes controlling calcite dissolution rate applies across laboratory, water column, and porewater environments. In all three environments, there is a meaningful shift in dissolution rate near the same thermodynamic driving force, once corrected for temperature and pressure. Differences in the absolute magnitude of the rate and the strength of the Ω dependence may reflect changes to calcite surface energetics that are specific to marine porewaters. We discuss these considerations below.

5.2 Surface energetic parameters

Using the framework described in Dove et al. (2005) and subsequently applied to calcite dissolution by Naviaux et al. (2019a), we can define surface energetic parameters to help us understand what processes on the mineral surface are controlling our observed rate behavior.

These different surface mechanisms are defined in terms of σ and a surface normal dissolution rate, m/s, following Equations 19 and 20, respectively:

Eq. 19) $\sigma = \ln(\Omega)$

Eq.20) Surface normal rate = $\ln\left(\frac{R_D}{(1-\Omega)^{\frac{2}{3}} * |\sigma|^{\frac{1}{6}}}\right)$

For dissolution proceeding via the formation of etch pits, (at lattice defects or homogeneously from flat surfaces), the overall dissolution rate dependence on saturation state is given by:

Eq. 21) $$\ln\left(\frac{R_{2D}}{(1-\Omega)^{\frac{2}{3}} |\sigma|^{\frac{1}{6}}}\right) = \ln\left(h\beta C_e(\omega^2 h n_s a)^{\frac{1}{3}}\right) - \frac{\pi\alpha^2\omega h}{3(k_b T)^2}\left|\frac{1}{\sigma}\right|$$

Where h is the step height (m), β is the step kinetic coefficient (m/s), ω is the molecular volume of calcite (m^3), n_s is the density of active nucleation sites (sites/m^2), a is the lattice spacing (m) , α is the step edge free energy (mJ/m^2), k_b is Boltzmann's constant, T is the temperature in Kelvin and C_e is the mineral solubility.

Dissolution that proceeds by the retreat of existing steps on the mineral surface (near equilibrium mechanism), follows a different formulation, show as:

Eq. 22) $$\ln\left(\frac{R_{2D}}{(1-\Omega)^{\frac{2}{3}} |\sigma|^{\frac{1}{6}}}\right) = \ln\left(\frac{\omega\beta m h}{P}\right) + ln\left((1-\Omega)^{\frac{1}{3}}\left|\frac{1}{\sigma}\right|^{\frac{1}{6}}\right) - \ln\left(1 + 8\left(\frac{\omega\alpha}{P k_b T}\right)\left|\frac{1}{\sigma}\right|\right)$$

Where, *P* is the perimeter of the screw dislocation that is the source of the existing steps and m is the number of elementary steps (equal to 1). The values *h, ω, a, P,* and *m* are all assumed constants, specific to the calcite crystal structure. The terms C_e, *T,* Ω and σ are all defined relative to a given experiment. This leaves the fundamental unknowns: β, n_s and α.

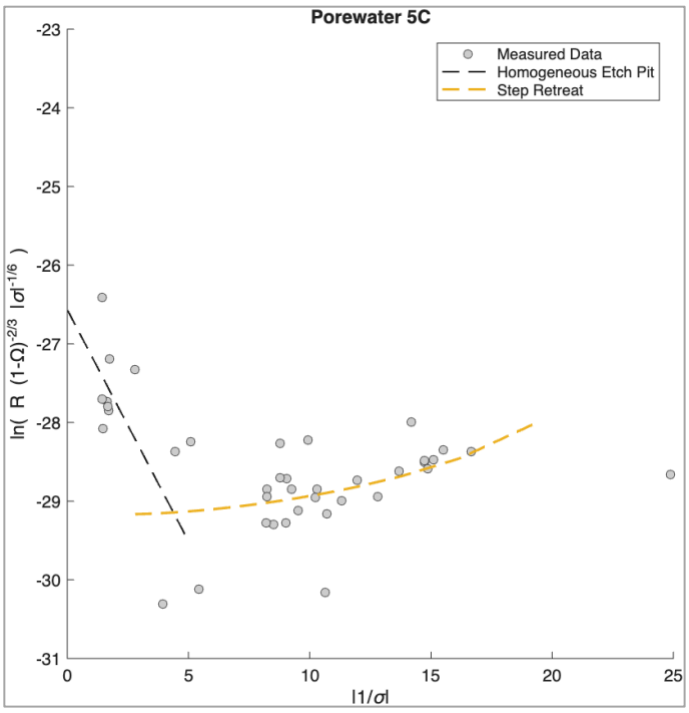


Figure 16. The surface energetic framing of the rate vs. undersaturation. The y-axis is the surface normal dissolution rate as defined in **Equation 20**. The x-axis is a translation of Ω following **Equation 19**. The measured data are reported in grey circles for all stations. The black dashed line represents the fit for the homogeneous etch pit regime (**Equation 21**) and the yellow, curved dashed line represents the fit for step edge retreat (**Equation 22**).

When plotted in terms of R_{2D} and $|1/\sigma|$ (**Figure 16**), the discontinuities in slope, by definition, define a change in surface energetic mechanism. Likewise, regressions through the data in surface energetic framing hold mechanistic information in their slope and intersect values. Note that the slope and intercept in this framing are distinct from the slope and intercept determined from the York fitting in Section 5.1. The latter contains no mechanistic information but is useful for comparison across studies. In contrast, the intercept and slope of each fitted segment in **Figure 16**, in the surface energetic framing, can be used to solve for the thermodynamic unknowns: β, n_s and α.

Eq. 23) $$Intercept = ln\left(h\beta C_e(\omega^2 h n_s a)^{\frac{1}{3}}\right)$$

Eq. 24) $$Slope = -\frac{\pi\alpha^2\omega h}{3(k_b T)^2}$$

In the step retreat regime, surface energetic parameters β and α are fit to Equation 22. The surface energetic parameters derived from fitting the data both close to and far from equilibrium are listed in **Table 3** and compared against the fitted parameters in 5°C benchtop and water column experiments.

Table 3. Surface energetic parameters derived from Equations 21-24 for the benchtop experiments of Naviaux et al. (2019a), the water column experiments of Naviaux et al. (2019b) and this study.

	Step Edge $\|1/\sigma\| > 5.2$			**Homogeneous $\|1/\sigma\| < 5.2$**		
	β, m/s	**n_s, sites/m²**	**α, mJ/m²**	**β, m/s**	**n_s, sites/m²**	**α, mJ/m²**
Naviaux et al. 2019a (refit by Barnhart et al., 2026)	$3 \cdot 10^{-7} \pm 5 \cdot 10^{-8}$	n/a	-0.5	$4 \cdot 10^{-4}$	$5 \cdot 10^{12}$	-37.6 ± 0.7
Naviaux et al. 2019b – Water column	$4 \cdot 10^{-8} \pm 2 \cdot 10^{-8}$	n/a	-0.5	$3.5 \cdot 10^{-4} \pm 2 \cdot 10^{-4}$	$5 \cdot 10^{12}$	-32 ± 3
This study	$10^{-6} \pm 26$	n/a	-6	3.03·10-4	$5 \cdot 10^{12}$	-21.23

In the step retreat regime, the porewater data shows that the step kinetic coefficient is one to two orders of magnitude greater than on the bench and in the water column, respectively. This parameter drives the offset in dissolution rates between the three experiments. In this regime α, which roughly correlates with the slope of the data, is an order of magnitude larger than the other two environments, corresponding to a larger energy barrier for propagating a retreating step.

In the homogeneous etch pit regime, the estimate of β assumes that the surface is saturated with etch pits, following the observations of Dong et al. (2020), in which the density of etch pits is high and roughly constant. In this case, the step edge retreat values in porewater experiments are comparable to those in the water column. Both are slower than in the laboratory. The step edge free energy in this regime is notably lower than in the water column or benchtop, pointing a smaller sensitivity of activating new etch pits to the solution undersaturation, consistent with the shallow slopes in log-log space (**Figure 14**).

5.3 Rate magnitude offset

While maintaining the same structure for their undersaturation dependence, all three datasets are offset from one another in magnitude in the close to equilibrium/step retreat regime. The offset between the benchtop experiments (Naviaux et al., 2019a, reprocessed in Chapter 2) and water column experiments (Naviaux et al., 2019b) has been discussed by Naviaux et al. (2019b) and attributed to inhibition of dissolution rates in the water column by specific dissolved organic matter species.

Briefly, the same seawater used in the water column experiments was collected, stored and carbon system parameters monitored to confirm that dissolved organic carbon in the original water had been respired during storage. When dissolution experiments were performed in the lab using this respired water-column seawater (5°C, atmospheric pressure), measured dissolution rates agreed with the benchtop rates. As additional validation, Naviaux et al. (2019b) added specific forms of organic carbon to benchtop experiments and showed that certain molecules depressed dissolution rates to roughly same degree observed in the water column experiments.

Why don't we see the same rate depression in porewater relative to benchtop rates that we see in the water column? The answer may lie in which forms of organic carbon reach the seafloor. More labile organic carbon may be respired before reaching the seafloor, leaving only the most refractory material to interact with sedimentary carbonate (Arndt et al., 2013; Lee, 1992). Of the species that Naviaux et al. (2019b) tested, D-glucose was found to be the most effective at inhibiting rates. This species is highly labile and tends to be consumed in the upper water column (Bianchi et al., 1996). Without direct measurements of organic carbon species at our study sites, we can only speculate about how differences in water column vs. benthic DOC pools in driving dissolution rate offsets.

An offset in rate magnitude also exists between our *in situ* experiments and the Naviaux et al. 2019a 5°C benchtop experiments in the close to equilibrium regime. This may be due to the kinetic pressure effect described by Dong et al. (2018). In that study, dissolution rates increased with elevated pressure even after accounting for the pressure effect on the solubility product, with rates enhanced by a factor of 2-4× at pressures up to 700 dbar, over $\Omega = 0.65\text{-}1$. This factor of 2-4 matches observations between the benchtop and our *in situ* porewater experiments. However, Dong et al. (2018) noted that above 700 dbar (up to 2500 dbar), no additional rate enhancement was observed.

This interpretation captures why the *in situ* rates are faster than the benchtop rates performed at atmospheric pressure, but the question remains why our *in situ* rates are so much faster than water column rates measured at comparable depths and pressures. This may indicate that the inhibitory effect of specific organic carbon species is stronger than assumed by Naviaux et al. (2019b). The observed DOM inhibition may operate on top of a kinetic pressure enhancement.

In the far from equilibrium regime, porewater rates are comparable to the magnitude of the 5°C benchtop experiments. However, the two datasets exhibit different slopes. When translated through Equations 21 and 24, the measured slopes can be interpreted in terms of the free energy for homogeneously forming etch pits. Compared to benchtop experiments, our porewater experiments have a lower free energy for etch pit formation. In the Dong et al. (2018) experiments, higher pressures were associated with lower free energies for the formation of defect-assisted etch pits (they did not perform experiments in the homogeneous regime). Taken together, we interpret our far from equilibrium porewater experiments to have lower sensitivity to Ω (shallower slopes) as the result of a

kinetic pressure effect that can be mechanistically described in terms of a lower free energy for the formation of etch pits.

5.4 Porewater dissolution profiles

The magnitude of the $\delta^{13}C$ dissolution signal and the modeled net dissolution rates vary systematically with depth and correlate strongly with porewater profiles of pH, Ω, and dissolved Mn^{2+} (**Figure 2**, **Figure 5, Figure 17**). These covariations provide insight into the chemical processes driving changes in carbonate dissolution with depth in the sediment.

As discussed above, the normalized $\delta^{13}C$ of the "a" subsample represents the least-processed form of the isotopic data and can be interpreted as a relative measure of dissolution-signal magnitude across stations. We include these values alongside the modeled net dissolution rates as an independent, ground-truthing of the depth dependence of the dissolution signal in **Figure 5**. Stations CR1 and CR5 exhibit the largest range in both $\delta^{13}C$ and modeled net dissolution rate; at both stations these maxima coincide roughly with peaks in the pH and Ω profiles and occur just shallower than the oxygen penetration depth.

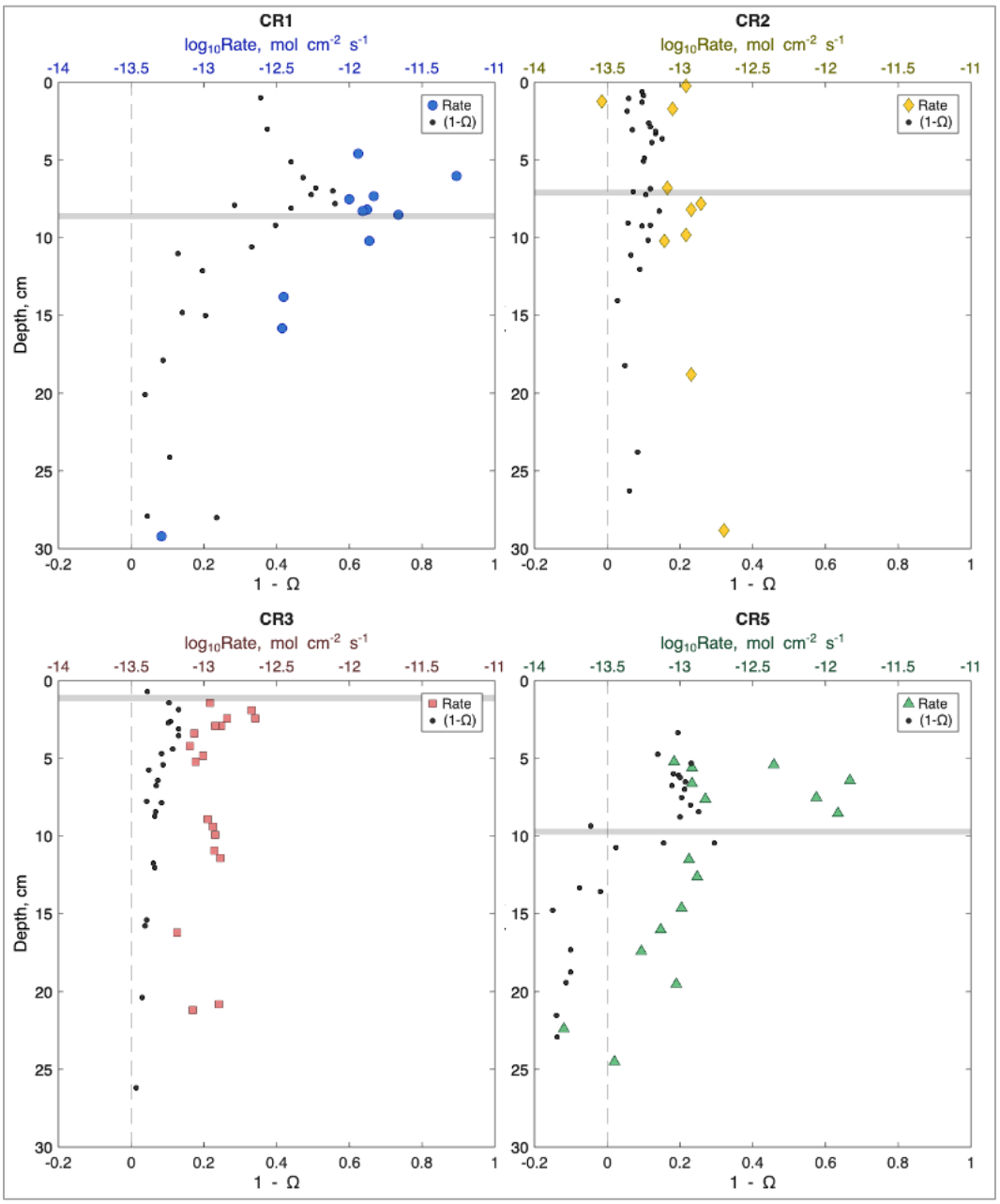


Figure 17. Dissolution rates plotted with porewater undersaturations for (a) CR1, (b) CR2, (c) CR3 and (d) CR5. The top x-axis in each panel is the log of the modelled dissolution rate and the bottom x-axis is (1- Ω). The horizontal grey bar donates the depth at which [Mn^{2+}] markedly increase from zero, which we interpret to be the approximate oxygen penetration depth. The dashed vertical line represents Ω = 1. The offset between the top and bottom x-axes are arbitrary and meant to capture the whole range of net rates – it does not indicate any specific scaling between rate and Ω.

This spatial correspondence with the oxic zone indicates that the process(es) enhancing dissolution rates are oxygen dependent. Two candidate mechanisms are (1) oxic respiration-driven dissolution, in which CO_2 produced by aerobic organic matter degradation lowers porewater Ω (Emerson and Bender, 1981; Jourabchi, 2005) and (2)

acid production from oxidation of reduced porewater species (e.g., Fe, Mn, H_2S) diffusing upward across the oxygen penetration depth (Aller and Rude, 1988; Boudreau, 2000). We infer that both processes operate to varying degrees at every station and that they are buffered differently depending on sediment carbonate content. Combining porewater chemical profiles with our novel measurements of dissolution rates lets us directly attribute the processes controlling *in situ* carbonate dissolution.

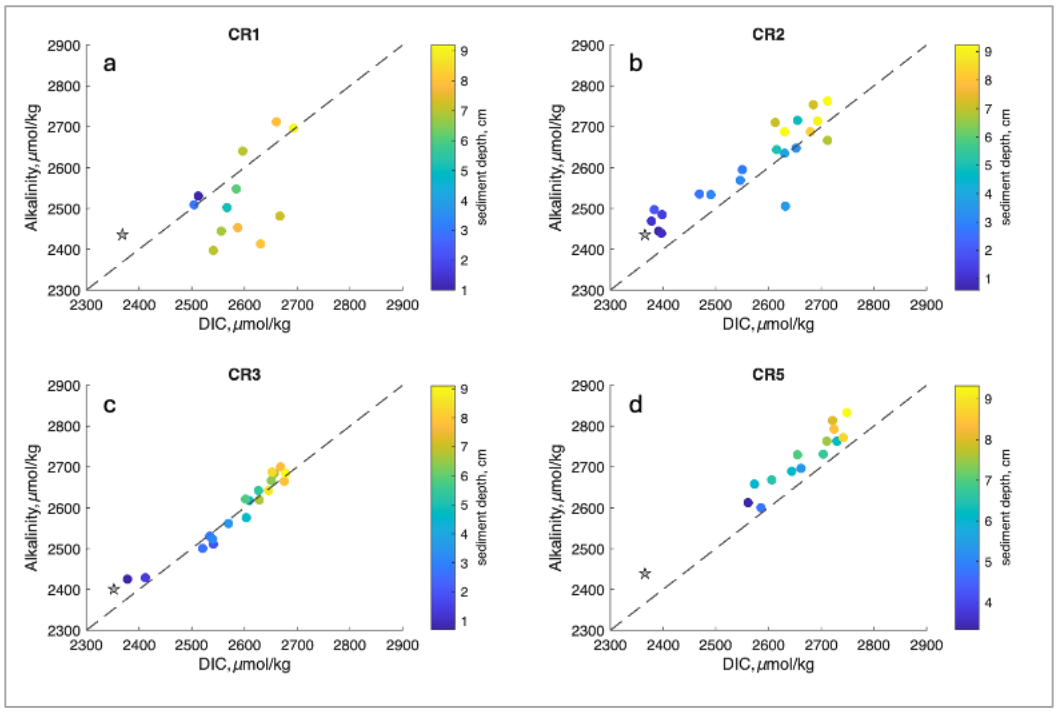


Figure 18. Alkalinity and DIC pairs from porewater measurements in the top 10cm of the sediment (a) CR1, (b) CR2, (c) CR3 and (d) CR5. One to one lines are denoted by the dashed line. The grey stars in each panel represent the composition of the overlying water at each station. The color coding of the points in each plot corresponds to the depth of each sample below the sediment-water interface.

The ratio of alkalinity to DIC in the upper 10 cm (**Figure 18**) falls into three main populations. The first has low alkalinity and low DIC and closely resembles the OLW. Some mixing with OLW during sample collection is possible, but this composition is also expected. A second population falls along a 1:1 alkalinity to DIC line, offset toward higher DIC relative to the first population. A DIC-only increase with no accompanying alkalinity change is diagnostic of aerobic respiration of organic carbon:

Eq 25) $C_{org} + O_2 \rightarrow CO_2 + \text{nutrients}$

in which only DIC (as CO_2) is added to the porewater. Carbonate dissolution driven by this CO_2 addition proceeds following Equation 21, which, in the net, yields a 1:1 alkalinity to DIC ratio.

Eq 26) $CaCO_3 + CO_2 + H_2O \Leftrightarrow Ca^{2+} + 2HCO_3^-$

A third population in the alkalinity to DIC plot, seen prominently only at CR1, has low alkalinity relative to DIC. In depth space this corresponds to a pronounced low-alkalinity, low-pH interval at ~5–10 cm, coincident with the oxygen penetration depth at this station (~10 cm). We attribute this to acid production from oxidation of upward-diffusing reduced species near the oxygen penetration depth. Depending on the oxidant, this reaction can be written:

Eq 27) $Fe^{2+} + 0.25\ O_2 + 2\ HCO_3^- + 0.5\ H_2O \Leftrightarrow Fe(OH)_3 + 2\ CO_2$

Eq 28) $Mn^{2+} + 0.5\ O_2 + 2\ HCO_3^- \Leftrightarrow MnO_2 + 2\ CO_2 + H_2O$

Eq 29) $H_2S + 2\ O_2 + 2\ HCO_3^- \Leftrightarrow SO_4^{2-} + 2\ CO_2 + 2\ H_2O$

In each case no net DIC is produced (HCO_3^- is converted to CO_2), while two units of alkalinity are consumed, consistent with the pH, alkalinity, and DIC trends at CR1, and in contrast to oxic respiration, which adds DIC without changing alkalinity.

Respiration and reduced-species oxidation can also be distinguished spatially. Respiration proceeds throughout the oxic portion of the sediment column, with products distributed by diffusive transport. Reduced-species oxidation, by contrast, is confined to the narrow interval where upward-diffusing reduced species meet downward-diffusing O_2, at or just below the OPD. This localized source produces the sharp, low-alkalinity, low-pH features observed near the OPD at CR1 (Figure 2b and 2c).

A similar low-pH feature appears at CR5, but without the corresponding low alkalinity seen at CR1. We attribute this to CR5's higher sediment carbonate content. The alkalinity consumed by redox reactions there is offset by carbonate mineral dissolution, following the example in Equation 30:

Eq 30) $Mn^{2+} + 0.5\ O_2 + 2CaCO_3 + H_2O \Leftrightarrow MnO_2 + 2Ca^{2+} + 2HCO3$

Here, Mn^{2+} oxidation drives a 1:1 increase in alkalinity and DIC, matching the ratio observed in CR5's upper 10 cm. The pH profile is what lets us identify a redox contribution at CR5 despite the absence of an alkalinity anomaly.

The carbonate-buffered redox pathway at CR5 (Equation 30) dissolves more $CaCO_3$ per mole of O_2 consumed (4 mol $CaCO_3$ per 1 mol O_2) than respiration-driven dissolution alone (1:1). This higher yield per unit oxygen helps explain why the dissolution signal at CR5 exceeds that at the purely respiration-dominated stations CR2 and CR3, even without the pronounced pH/alkalinity anomaly seen at CR1.

At CR2 and CR3, alkalinity and DIC fall along a roughly 1:1 line (noisier at CR2), without the low-pH spike seen at CR1 and CR5. Both stations have higher sediment carbonate content, giving greater buffering capacity against Ω changes from either respiration or reduced-species oxidation. Notably, CR2 and CR3 also have less dissolved

Mn^{2+} below their respective oxygen penetration depths compared to CR1 and C5. A smaller upward Mn^{2+} flux across the OPD would limit redox-driven acid production, reinforcing why CR2 and CR3 lack the alkalinity/pH anomalies at CR1 and CR5, and why their dissolution signal is better explained by respiration alone.

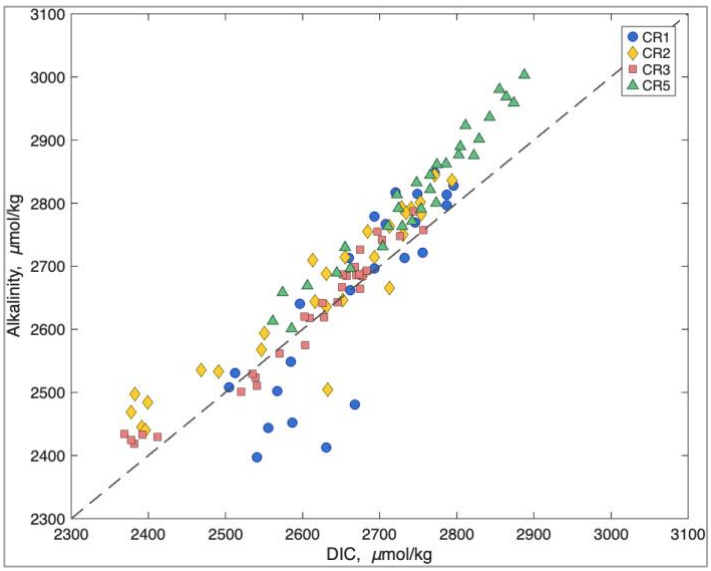


Figure 19. Alkalinity and DIC measurements for porewater samples for 0 to 35cm sediment depth for CR1 (blue circles), CR2 (yellow diamonds), CR3 (red squats) and CR5 (green triangles). The 1:1 line is denoted as a dashed line.

A potential fourth porewater chemistry population be defined at high alkalinity and high DIC where the ratio shifts to greater than 1:1. This population appears more prominently in the full porewater chemistry profiles in **Figure 19**, and, in particular at CR5. In general, these high alkalinity and high DIC porewaters sit near the bottom of our sediment profiles. At CR 5 the points start to fall off the 1:1 line at ~8-10cm, the same depth where we note an increase in porewater $Mn^{2+}$and interpret as the depth of oxygen penetration. Increasing alkalinity in anoxic conditions is consistent with anaerobic metabolisms. Equations 31-33 are examples of anaerobic metabolisms the can net > 1:1 alkalinity to DIC. The degree to which alkalinity is produced in excess of DIC is specific to assumptions about the ratio of C:N:P in the organic matter being metabolized.

Eq. 31) $(CH_2O)(NH_3)_{(n/c)}(H_3PO_4)_{(p/c)} + 0.8NO_3^- \Leftrightarrow 0.2CO_2 + 0.4N_2 + 0.8HCO_3^- + (n/c)NH_3 + (p/n)\ H_3PO_4 + 0.6H_2O$

Eq. 32) $(CH_2O)(NH_3)_{(n/c)}(H_3PO_4)_{(p/c)} + 2Mn(O)_2 + 3CO_2 + 4H_2O \Leftrightarrow 4HCO_3^- + 2Mn^{2+} + (n/c)NH_3 + (p/c)H_3PO_4$

Eq. 33) $(CH_2O)(NH_3)_{(n/c)}(H_3PO_4)_{(p/c)} + 4Fe(OH)_3 + 7CO_2 \Leftrightarrow 8HCO_3^- + 4Fe^{2+} + (n/c)NH_3 + (p/c)H_3PO_4 + 3H_2O$

The shift towards higher alkalinity at CR5 could also explain the increase in the saturation state beyond $\Omega = 1$. As noted above, even though these porewaters are

supersaturated, we still see measurable dissolution. This may be explained by other chemical changes in the porewater and their relationship to setting the calcite saturation state. CO2SYS is parameterized to calculate Ω for changing carbonate system parameters, not major ion chemistry. In the presence of elevated Mn^{2+} or Fe^{2+}, the speciation of carbonate ion may shift. For example, the formation of the $MnCO_3^0$ ion pair (logK = ~5; Grauer, n.d.; Luo and Millero, 2003) would shift the pK_{a2} in the carbonate system to higher values and, therefore, Ω to lower values. While the total concentration Mn^{2+} in solution is low relative to the other species that complex carbonate (e.g. Mg^{2+}, which complexes roughly 50% of the carbonate in seawater), even small changes to carbonate ion speciation can be meaningful for Ω.

5.5 Implications for the calcite lysocline

The calcite lysocline corresponds to a zone, roughly ~1 km thick, above the calcite compensation depth (CCD), over which the rate of carbonate dissolution increases rapidly (Berger, 2016). Equivalently, the lysocline can be described as the depth interval over which sedimentary carbonate content drops sharply. The depth and thickness of the lysocline are generally attributed to some combination of deep ocean circulation, bottom water saturation state, calcite dissolution kinetics, sediment porosity and bioturbation, and the rain rate of organic matter relative to calcite (Archer, 1991, 1996). Models incorporating these controls have achieved moderate success in reproducing observed lysocline shape and depth, but they consistently over-predict a "tail" of low-but-nonzero $\%CaCO_3$ extending deeper than is observed in real sediments. This is an artifact linked to the use of linear dissolution rate laws, which respond only to bottom-water saturation state and cannot reproduce the sharp, near-complete loss of carbonate seen in the deepest part of the transition zone. Subhas et al. (2015) illustrated with a simplified box model how nonlinear kinetics more accurately capture the structure of the calcite lysocline.

Our work introduces two new observations: (1) that the saturation state in the porewaters can be decoupled from the saturation state of bottom water and (2) defines specific mechanisms by which the porewater undersaturations and dissolution rates can be enhanced. We show that acid generation within the sediment column, via either organic matter respiration or oxidation of upward-diffusing reduced species, can decouple *in situ* dissolution rates from bottom water chemistry, driving faster dissolution than bottom-water Ω alone would predict. In some cases, this can push porewater Ω across critical undersaturation thresholds where dissolution kinetics change fundamentally (see Section 5.1). Because this acid production is generated *in situ*, close to the sediment-water interface and independent of the overlying water's saturation state, it represents a dissolution pathway that a bottom-water-forced, rate laws capture.

5.6 Implications for ocean alkalinity cycling

The same processes that set the depth and structure of the calcite lysocline also govern the timescale over which the ocean's carbonate system responds to changes in atmospheric CO_2 and alkalinity. Following Archer et al. (1997, 1998), this "carbonate compensation" timescale is conventionally estimated at ~5–6 kyr. There is evidence, however, in both the climate record and in modern marine environments for more rapid carbon cycling than this canonical timescale implies.

Some of this evidence comes from the upper water column, where organic matter and carbonate minerals held together within sinking marine particles can be subject to respiration and dissolution, producing localized undersaturated microenvironments even where bulk seawater is supersaturated (Kwon et al., 2024; Subhas et al., 2022; Ziveri et al., 2023). At the seafloor, Sulpis et al. (2018) showed that anthropogenic CO_2 uptake has already measurably accelerated benthic calcite dissolution, accounting for 40–100% of total seafloor dissolution at the most sensitive locations. This implies that the sedimentary $CaCO_3$ system responds to perturbation faster than a simple CCD-shoaling picture would suggest.

Our porewater rate profiles provide independent, mechanistic support for this broader conclusion: the alkalinity flux from marine sediments is not a slow, threshold response to bottom-water saturation state alone, but can be locally amplified, driven by respiration and redox process that can be decoupled from the bottom water saturation state. Specifically, the acid generation we document via both aerobic respiration and reduced-species oxidation provide concrete mechanisms by which sediment porewaters can sustain higher dissolution rates, and therefore larger alkalinity and carbon fluxes, than bottom-water Ω would predict on its own.

This effect is compounded by bioturbation, which continually overturns and homogenizes the upper part of the sediment. A grain residing in the bioturbated mixed layer can be repeatedly reworked through the mixed zone, including the depth interval of greatest undersaturation and highest dissolution intensity identified. Relative to a model that considers only bottom-water Ω, this repeated exposure to the zone of most intense in-situ acid generation increases the cumulative dissolution a given grain experiences before burial.

Respiration and redox driven carbonate dissolution within marine sediments are mechanistic pathways, based on direct observations of accelerated dissolution, that indicate the carbonate system may respond to changes in atmospheric CO_2 more rapidly than the canonical ~5–6 kyr compensation timescale.

6. Conclusions

We used *in situ* porewater chemical profiles and net dissolution rates across four stations in the Eastern Equatorial Pacific to, for the first time, directly measure *in situ* dissolution rates and identify the specific chemical processes controlling carbonate dissolution in marine sediments. Our findings revise how *in situ* carbonate dissolution should be understood and modeled.

The calcite dissolution rate law for marine sediments follows the same structure as benchtop and water column dissolution. This indicates that the same mechanisms controlling the dissolution rate as a function of undersaturation can be applied across all seawater environments. Notably, the rate of dissolution in porewaters can exceed the rates in the laboratory and in the water column, potentially due to a kinetic pressure effect and

the absence of specific organic carbon species in the porewaters that may otherwise inhibit dissolution.

Porewater alkalinity, DIC, pH, and Mn^{2+} profiles point to two distinct processes driving carbonate dissolution, and that their relative contributions vary with sediment carbonate content. Where carbonate content is low (CR1), acid generated by oxidation of reduced species near the oxygen penetration depth is poorly buffered and produces sharp, localized alkalinity and pH minima, and correspondingly large dissolution signals. Where carbonate content is higher (CR5), the same redox acid production instead titrates against the sediment's carbonate reservoir, elevating both alkalinity and DIC together rather than depressing alkalinity alone, muting the pH and alkalinity anomalies while still enhancing dissolution relative to majority respiration-driven stations (CR2, CR3). This is, to our knowledge, among the first direct attributions of specific *in situ* processes to measured porewater dissolution rates, rather than an inference from bulk fluxes alone.

These mechanisms have consequences beyond the individual stations we sampled. Porewater acid generation can be decoupled from bottom-water saturation state and can drive dissolution rates that a bottom water Ω model would not predict. This may even include locally crossing critical undersaturations that trigger disproportionately faster dissolution (i.e. transitions into homogeneous etch pit formation mechanism). This decoupling, combined with bioturbation induced reworking of sediment, implies that the sedimentary carbonate system can respond to changes in ocean carbon chemistry faster than the canonical ~5–6 kyr carbonate-compensation timescale. This is consistent with independent evidence that anthropogenic CO_2 has already measurably accelerated benthic dissolution at some seafloor locations (Sulpis et al., 2018) and that comparable respiration-driven dissolution occurs in the upper water column.

Chapter 4. Calcite dissolution kinetics in sulfate-free seawater

1. Introduction

Calcite dissolution has been studied extensively in freshwater. The predictions of classical crystal growth theory (Lasaga, 1998; Steefel and Van Cappellen, 1990), that dissolution proceeds at steps and via the formation of etch pits, has been observed by atomic force microscopy (AFM) and vertical scanning interferometry (VSI) on calcite (R. S. Arvidson et al., 2006; Astilleros et al., 2010b; Ruiz-Agudo et al., 2010; Teng, 2004). In this approach, dissolution can be quantified in terms of the rate that the step retreat and etch pits form and propagate. There are limitations, however, in translating surface measurements into bulk dissolution rates needed for application in most settings.

Dove et al. (2005) used the framework of classical crystal growth theory to translate bulk quartz dissolution rate measurements in surface energetic parameters, analogous to those observed in AFM studies. Naviaux et al. (2019) applied this framework to calcite dissolution and found that the undersaturation dependence of dissolution rates in seawater can be described in terms of the particular surface mechanisms. That said, the reactivity of calcite is not fully captured by this energetic description alone. There is a chemical component that is also important, involving the chemical speciation of aqueous solutions and of the mineral surface.

Arakaki and Mucci (1995) addressed this in freshwater, successfully describing calcite dissolution in terms of four elementary reactions whose combined kinetics set the overall dissolution rate. In freshwater, the number of dissolved species and their possible interactions is small enough that this reaction set can be defined explicitly. In seawater, even considering only the major ions, the number of possible species interactions grows exponentially. This is compounded by the nonlinear effects of high ionic strength on ion activities. As a result, it is difficult to define the activity of individual seawater species or identify which reactions they participate in during dissolution.

Recently, Humphreys et al, (2022) and others have developed a model (MarChemSpec) describing the chemical speciation of seawater using the Pitzer ion-interaction approach, calculating activity coefficients for the major seawater constituents. This is a meaningful advance for two reasons. First, even estimating Ω is difficult in seawater whose major-ion composition deviates from that assumed at a given salinity, because the equilibrium constants conventionally used to calculate Ω are themselves empirically calibrated to standard seawater composition. The Humphreys et al. (2022) framework allows Ω to be calculated reliably even as major-ion composition is varied. Second, this tool opens the door to a chemical description of calcite dissolution in seawater that accounts for the individual aqueous species influencing dissolution rate, rather than treating seawater's effect on kinetics as an empirical, composition-specific fitting exercise. It allows us to probe, mechanistically, how specific aqueous species influence calcite dissolution kinetics in seawater.

We use this framework to examine the role of sulfate in calcite dissolution kinetics. Sulfate has been shown to inhibit calcite dissolution rates in seawater (Mucci, 1986; Sjoberg, 1978) but these studies have focused almost exclusively on far-from-equilibrium conditions. To date, there are no direct constraints on how sulfate influences calcite dissolution rates near calcite saturation, where much of the modern ocean actually resides.

In the modern ocean, microbial sulfate reduction in anoxic basins and porewaters can locally deplete sulfate concentrations, and over Earth’s history sulfate concentration have varied from 0 to 28mM (Canfield and Farquhar, 2009; Fakhraee et al., 2024). Under these conditions and past

environments, applying rate laws calibrated to seawater with modern sulfate concentration could give a biased picture of carbonate dissolution and preservation.

Sulfate depletion may also be relevant to dolomitization. Dolomite formation has been associated with fluids of elevated Ca/SO_4 ratios (Qiu et al., 2019; Rivers, 2023). However, the dissolution kinetics of the precursor calcite, which must dissolve for dolomitization to proceed, are an often overlooked and poorly constrained part of dolomitization models (Al-Helal et al., 2012). A rate law for calcite dissolution under low- or zero-sulfate conditions, such as we present here, provides a needed kinetic constraint for models of this process.

We performed calcite dissolution experiments in sulfate-free artificial seawater across a range of undersaturations. Using the speciation model of Humphreys et al. (2022), we calculate Ω values that can be used to compare dissolution experiments in varying composition seawater solutions. We define a calcite dissolution rate law for sulfate-free seawater and use a surface-energetic framework (Dove et al., 2008) to examine how the presence or absence of sulfate alters the mechanistic processes that control calcite dissolution rate across the full range of undersaturation.

2. Methods

2.1 Dissolution experiments and materials

The experiments presented here follow the same method described first in Subhas et al. (2015), in which ^{13}C labeled calcite grains (Sigma Aldrich, SKU 492027, >99 atom%) were dissolved in seawater with a defined undersaturation. The grains used were wet sieved to 20-53u size fraction. The average BET surface area for this range of grain sizes was measured to be 1520 +/- 60 cm^2/g (Naviaux et al. 2029a).

Each experiment consists of 1-5mg of labeled calcites grains placed in an airtight 1L Supelco bag (SKU 30336-U). The seawater used in each experiment is prepared by acidifying with 0.1M HCl to a known undersaturation value. Approximately 300g of the acidified seawater is added to the experiment bag containing the labeled grains. When all 300g are added, the experiment is considered "started" (t= 0). The experiment bags sit on a shaker table and are considered well mixed over the duration of an experiment.

The undersaturation of seawater dictates how long an experiment is run, which can range from hours to one week. For each experiment, eight samples are collected, evenly spaced in time over the duration of the experiment. At the end of the experiment, the alkalinity is measured on the remaining seawater. The samples collected over the course of an experiment are analyzed for DIC and $\delta^{13}C$ of DIC on a Picarro cavity ringdown spectrometer.

2.1.1 Artificial seawater solutions

The seawater used in the experiments is either Dickson standard seawater (Dickson, 2010) or modified Aquil - artificial seawater (Morel et al. 1979) with varying sulfate concentrations. The Morel et al. (1979) "recipe" is listed in the first column of **Table 1**. A reservoir of Aquil is made by adding individual salts of the species listed in **Table 1**, column 1 to MilliQ water and poisoning it with $HgCl_2$. To make sulfate-free Aquil – no sulfate salt (Na_2SO_4) was added to the solution. The total salinity of the solution is maintained by addition of either KCl or NaCl salt in the proportion that Na_2SO_4 was removed. In the case of the KCl compensated solutions – the addition amount was overshot, resulting in higher overall salinities than the NaCl compensated solution and Dickson seawater.

Table 1. Concentrations (mol/kg) of species in Morel et al. (1979) sweater recipe, estimates for Dickson seawater and estimates for Aquil solutions used in experiments (calcium corrected, see text).

Species	Morel Base Recipe	Average Dickson Seawater***	Aquil HB1	Aquil HB2	Aquil HB3	Aquil HB4	Aquil HB5	Aquil - JN
Salinity		33.42	36.66	36.64	36.65	33.44	36.46	33.46
Na	440.3	447.7	440.3	440.3	440.3	458.3	440.3	458.3
Mg	52.88	50.42	52.20	52.44	52.45	52.48	52.15	52.88
Ca*	10.29	9.79	10.11	9.89	9.97	9.98	9.99	10.29
K	9.98	9.74	67.14	67.14	67.14	9.98	67.14	9.98
Sr	0.06	0.09	0.06	0.06	0.06	0.06	0.06	0.06
Cl**	418.9	** charge balance	** charge balance	** charge balance	** charge balance	** charge balance	** charge balance	** charge balance
SO_4	28.1	26.95	0	0	0	0	0	0
Br	0.82	0.80	0.82	0.82	0.82	0.82	0.82	0.82
F	0.07	0.04	0.07	0.07	0.07	0.07	0.07	0.07
B	0.47	0.39	0.47	0.47	0.47	0.47	0.47	0.47

To identify major changes to Ca^{2+} between batches of sulfate-free Aquil, we measured our artificial seawater solutions on Shimadzu Nexera IC. We report the peak areas of Ca^{2+} and Mg^{2+} relative to the first batch of Aquil prepared for this suite of experiments, denoted Aquil-JN. These values are noted in Table 2. Where the relative differences between a given batch of Aquil and the reference Aquil exceeded 1%, we made a correction in our reported solution composition in Table 1 following:

Eq 1) $[i]^j_{corr} = [i]_{ref}\ (1- CF_i^j/100)$

where $[i]_{ref}$ is the concentration of species *i* in the reference Aquil, CF_i^j is the correction factor for species *i* in an Aquil reservoir *j* and $[i]_{corr}$ is the corrected concentration reported in Table 1. For calcium in particular, this correction matters first order for the calculation of Ω.

To calculate an Ω value from MarChemSpec at a given alkalinity and pH, all other major species in solution must be defined. The values are not reported for the Dickson standard seawater. We use an alternate mode of the MarChemSpec model that calculates the full speciation of seawater under for a given salinity and temperature (atmospheric pressure). We input our experiment temperatures and the salinities reported for each batch of Dickson to output the full speciation of these waters. This speciation calculation was used to define the unknown species in the subsequent use of these waters to calculate Ω.

Table 2. Correction factors for Aquil batches, denoted as percent concentrations relative to the Aquil-JN solution.

	CF – Ca %	CR – Mg %
Aq - HB1	1.71	1.25
Aq - HB2	3.80	0.83

Aq - HB3	3.14	0.82
Aq - HB4	3.00	2.65
Aq - HB5	2.90	1.39

2.2 Rate calculation

The dissolution rate is quantified following the approach taken by Subhas et al. (2015) and Naviaux et al. (2019a). This involves translating the $\delta^{13}C$ of each sample into a "moles of ^{13}C added" to the solution and fits a linear regression through the linear portion of the ^{13}C added v time trace.

Eq. 1) $${}^{i+1}_{i}n_{13C} = m_i * \left[{}^{12}C\right]_{init} * \left(R^{13}_{i+1} + R^{13}_{i} \right)$$

Eq. 2) $$R^{13}_{i} = \left(\frac{\delta^{13}C_i}{1000} + 1\right) * \quad R^{13}_{PDB}$$

Here, the subscript i denotes the timepoint, m_i is the mass of seawater at timepoint i, $[^{12}C]_{init}$ is the initial concentration of ^{12}C, and R^{13}_i is the ratio of $^{13}C/^{12}C$ at timepoint i. Cumulative moles of calcite dissolved at each sampling time were obtained by summing incremental dissolution from the start of the experiment to time t_i. Net dissolution rates were calculated by fitting a linear regression to the portion of the cumulative dissolution versus time curve that exhibited linear behavior, where it is assumed that the dissolving surface attained isotopic steady state. The slope of this regression yields the net dissolution rate in units of moles per unit time, which are reported normalized to surface area. This approach makes a key assumption that, in the first ~24 hours of an experiment, the mineral surface evolves its isotopic composition.

2.3 Modelling of $\delta^{13}C$ vs time

A numerical model was defined to describe the time evolution of the $\delta^{13}C$ during an induvial dissolution experiment of the type performed here (see Chapter 2). In short, the model tracks the movement of ^{13}C and ^{12}C on and off the mineral surface. The size of the surface reactive reservoir, the magnitude of the gross dissolution rate, and the ratio of the gross rates are free parameters in the model.

The model produces $\delta^{13}C$ vs. time traces and tunes the free parameters following a least-squares non-linear optimization function in Matlab (*lssqnonlin)*. The $\delta^{13}C$ profiles are fitted to measured $\delta^{13}C$ vs. time data collected from the experiments.

2.4 Ω critical calculation

We use changes in the slope of the rate vs. 1- Ω relationship to define transition in the mechanism controlling dissolution. We use the approach of Muggeo (2003) to find statistically meaningful changes in slope given unknown breakpoints. The approach consists of testing all known measurements as candidate breakpoints and comparing the resulting regressions against the fit of a single regression through the data. We enforce the condition that the regression lines must intersect. We propagate error though the calculation following a Monte Carlo strategy: each time the breakpoint test is run, the rate and Ω data are perturbed within their measured standard deviations.

3. Results

3.1 Undersaturation calculations

Small differences in Ω values that may arise from different models like CO2SYS or MarChemSpec can have important implications for how we interpret dissolution rates and define rate laws. The saturation state of calcite is defined by the solubility product of calcite, K_{sp}, the total calcium concentration, and the total carbonate concentration. We step through the treatment of each of these values in the two models.

In CO2SYS, the default K_{sp} is a constant value that may vary as a function of temperature, pressure and salinity following Mucci, (1983). For the experiments presented here we are concerned only with the salinity dependence. For each experiment with a defined salinity, a K_{sp} is determined. We use this same, salinity-specific K_{sp} to calculate Ω from MarChemSpec, which outputs an ion activity product (IAP = $[Ca^{2+}][CO_3^{2-}]$) from which we can calculate Ω.

In CO2SYS the calcium concentration is calculated as a function of solution salinity, following Riley and Tongudai (1967). No speciation calculations are preformed, meaning this value represents total dissolved calcium. In MarChemSpec, the value of total calcium is user-defined. The calcium concentration used in the IAP calculation uses total calcium.

The calculation of $[CO_3^{2-}]$ is dependent on the treatment of pH and the acid dissociation constants, primarily pK_{a2}. In CO2SYS the pK_{a2} for the carbonic acid system are assigned by the user and modified for temperature, pressure and salinity. We use the Lueker et al. (2000) refit to Mehrbach et al.'s (1973) data. These values are 5.888 and 9.046 for pK_{a1} and pK_{a2}, respectively (at 21ºC and 33.28 Sal). In MarChemSpec, the carbonic acid equilibrium constants are from Dickson and Millero, 1987 and are 5.844 and 8.987 for pK_{a1} and pK_{a2}, respectively at 21ºC. The pK_a values do not change in a meaningful way with changing alkalinity and DIC in MarChemSpec.

Note the offset in pK_{a2} between the two models. The pK_{a2} for MarChemSpec is ~0.06 log units lower than the pK_{a2} in CO2SYS. This value has strong influence on the calculated concentration of carbonate ion and therefore the Ω calculation. The direction of the offset indicates that for a given pH in the range of seawater, MarChemSpec will predict a higher $[CO_3^{2-}]$ than CO2SYS.

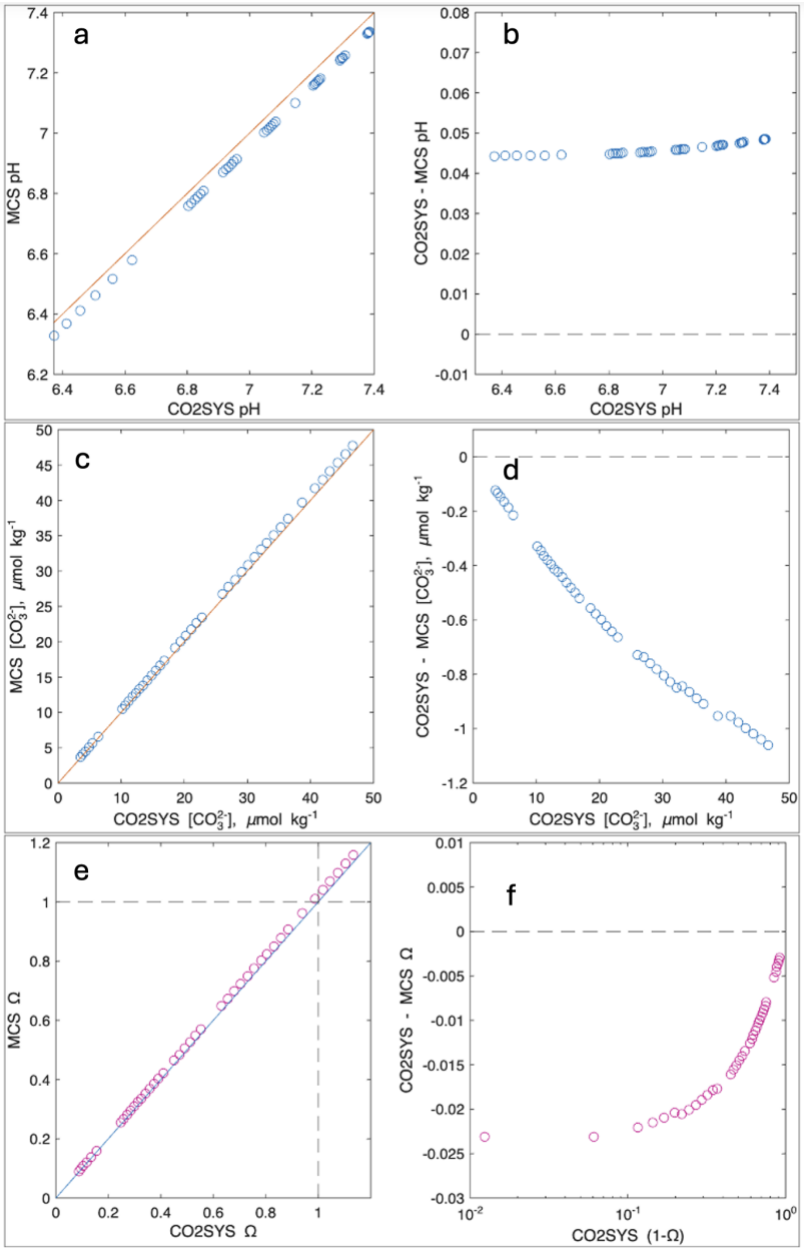


Figure 1. Comparison of CO2SYS and MarChemSpec models for pH (a,b), carbonate ion concentration (c,d) and saturation state (e,f). All test solutions were assigned a temperature of 21C and atmospheric pressure. Calcium concentration is 9.78 mmol/kg-SW in both models. Salinity is 33.275 +/- 0.005 for both models.

We compare the pH, $[CO_3^{2-}]$ and Ω between the two models for seawater solutions with varying alkalinity and DIC (1700-2250 umol/kg and 2000-2250 umol/kg, respectively) in **Figure 1**. Varying these two carbonate system parameters parallels the way we vary our experimental solutions in order capture a range of undersaturations. The temperature and pressure are constant between models. We assign a salinity of the solutions in CO2SYS to be 33.28, resulting in a calcium concentration 9.78 mmol/kg-SW and the solubility product, K_{sp} is $10^{-6.395}$.

For the temperature and salinities of the test natural seawater, we plug these values into MarChemSpec to get concentrations of the major ions in solution. We modify the calcium

concentration to that it is exactly equal to the value calculated by CO2SYS for a given salinity (Sal 33.275, 9.78 mmol/kg-SW).

In MarChemSpec, changing the calcium concentration to match CO2SYS and changing alkalinity necessitates rebalancing the solution charge balance, which we do by modifying the Cl^- concentration (one of the more inert species in seawater). This results in small changes of the overall salinity of the solution input into MarChemSpec, but that value is still 33.275 +/- 0.005, close to the input value for CO2Sys

Given this set up, we calculated a constant offset in pK_{a2}, in which the value calculated by MarChemSpec is smaller than CO2SYS. This difference is from the treatment of the activity coefficients in the calculation of the equilibrium constant. The implication of a lower pK_{a2} in MarChemSpec is that for a given pH, more of the carbon system will be speciated as bicarbonate relative to carbonate ions compared to the same pH in CO2SYS.

The estimated pH also differs between the two approaches. The pH predicted by CO2SYS is higher than that predicted by MCS for the same conditions, with a slight increase in the offset as pH increases. This likely derives from the different treatments of sulfate in either model, which matter when using the total pH scale.

Humphreys et al. (2022) note that a large fraction of the overall uncertainties in the comparison between the MarChemSpec model and measurements comes from the value of the dissociation constant of HSO_4^-. They use a value of 0.0105 (from Clegg et al., 2022), but experiment values can range from 0.01017 (Young et al. 1978) to 0.01086 Dickson et al. (1990). CO2SYS uses the Dickson value, resulting in reduced HSO_4^- and lower pH_T values.

The differences in $[CO_3^{2-}]$ are illustrated in **Figure 1c,d**. MarChemSpec predicts a larger value for $[CO_3^{2-}]$ compared to CO2SYS, meaning that the effect of decreasing the pK_{a2} has a larger influence than the decreasing pH on the amount of carbon speciated as carbonate ion in MarChemSpec. The overall result is that the Ω values in MarChemSpec can sit up to ~0.025 units higher than those calculated for the same solution conditions in CO2SYS. The offset is most dramatic near equilibrium and has a negligible influence below Ω ~0.5 (offset ~0.01, within our measurement error).

3.2 Influence of sulfate on MarChemSpec Ω

The MarChemSpec program allows us to calculate the Ω value of our seawater solutions with no sulfate. Figure 2 shows the sensitivity of carbon system parameters to the amount of sulfate in seawater. We stepped through combinations of alkalinity and DIC values ranging from 1700-2250 umol/kg and 2000-2250 umol/kg, respectively. We ran these combinations 5 times, varying $[SO_4^{2-}]$ each time, from 100% of the modern seawater (MSW) value to <0.1% of this value.

As noted above, the pK_{a2} in MarChemSpec is constant for seawater solutions in which only alkalinity and DIC change. However, when the sulfate concentration in seawater changes, the pK_{a2} does shift. As sulfate decreases from MSW values, the pK_{a2} increases. There are two possibilities for the change in pK_{a2} with sulfate, and it is likely that both are occurring to some degree. For a constant pH solution, if sulfate is removed, a larger fraction of the H+ will be free and available to interact with other species in solution. The balance of free carbonate ion to free bicarbonate will shift such that more of carbonate is titrated against the free protons, shifting the pK_{a2} to higher pH values.

Sulfate may also speciate with other ions in solution. In particular $MgSO_4^0$ ion pairs are thought to be important in seawater: ~10% of the Mg^{2+} in seawater is complexed with SO_4^{2-} (Fisher, 1967; Garrels and Thompson, 1962; Siebert and Hostetler, 1977). $MgCO_3^0$ pairs are thought to make up 45-65% of the total carbonate in solution, exerting a strong control on the pK_{a2}. If sulfate is removed, 10% of the total Mg that was previously bound to it may be available to further increase the $MgCO_3^0$ pool and shift the pK_{a2} to higher values. It is likely that a combination of these two processes is responsible for the observed shift in pK_{a2} in MarChemSpec noted in Figure2.

The pH of the solution increases when sulfate is removed (**Figure 2b**). ASW with no sulfate can be as much as 0.12 pH units higher than in the same seawater solution with modern sulfate concentrations. This is consistent with the definition of the total pH scale. As the concentration of total sulfur in the system decreases, the $[HSO_4^-]$ component of the total $[H^+]$ decreases and pH increases.

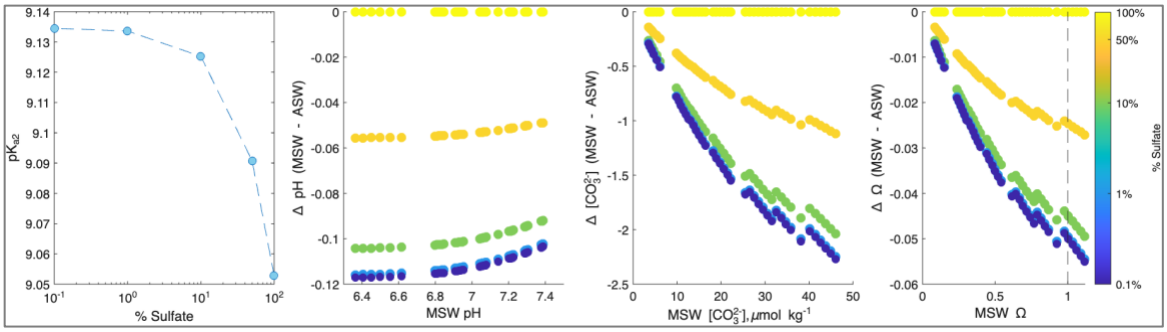


Figure 2. Summary of MCS carbon system parameters sensitivity to sulfate concentration. (A) pKa2 as a function of the % sulfate in solution relative to modern seawater sulfate concentrations (28mM). (B) The difference between modern seawater (MSW) pH and artificial seawater (ASW) pH, where the % sulfate of the artificial seawater varies between 0.1% and 100%. Cooler colors represent lower amounts of sulfate. (C) The difference in carbonate ion between MSW and ASW. (D) The difference in Ω between MSW and ASW. All panels are shown as a function of their respective value in MSW .

The modification of pH and pK_{a2} with changing sulfate act in opposite directions to influence the carbonate ion concentration, but as **Figure 2c** shows, the net effect of decreasing sulfate is to increase in the carbonate ion concentration. This means that the effect of changing the pK_{a2} has a larger influence than the change in pH when sulfate is removed. It follows that if carbonate ion increases in the absence of sulfate, then Ω will increase in the absence of sulfate, which is shown in Figure 2d. The effect of changing sulfate is most pronounced close to equilibrium, where the offset can be as much as 0.06 Ω units.

3.3 Calcite dissolution rates in sulfate free seawater

We calculated the dissolution rate for calcite in sulfate-free seawater solutions following the linear regression method described in Section 2.2 and originally in Subhas et al., 2015. The results are plotted in **Figure 3** with rates from dissolution experiments performed in Dickson standard seawater, with typical seawater sulfate concentrations (Naviaux et al., 2019a). Experiments performed in both types of seawater exhibit a strong, nonlinear dependence on solution undersaturation.

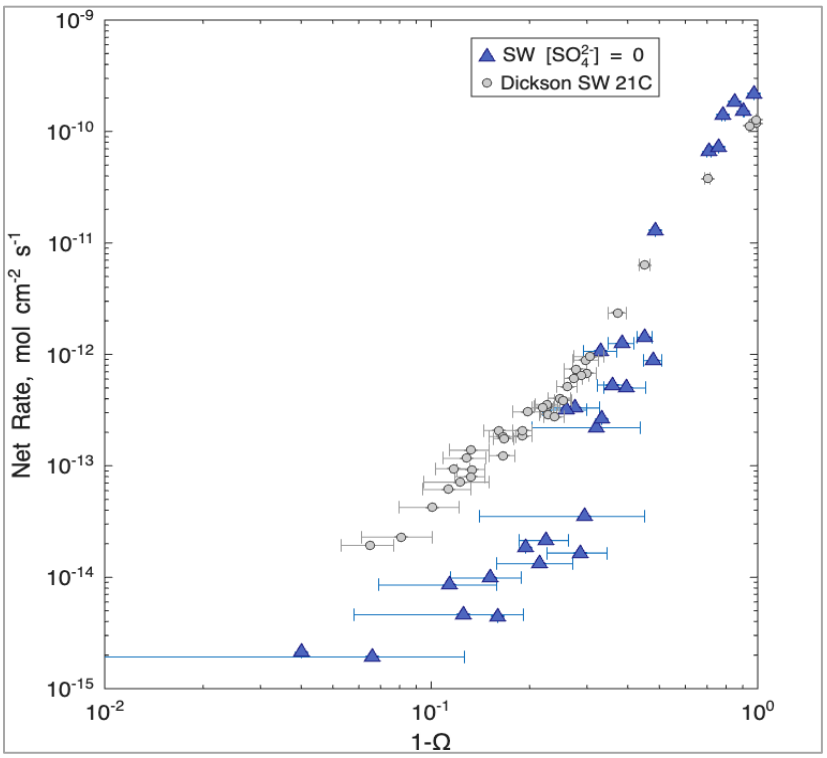


Figure 3. Net dissolution rate of labeled calcite grains in Dickson seawater (grey circles) and artificial seawater with $[SO_4^{2-}] = 0$ (blue triangles), both at 21°C. The Ω values for both seawater datasets are calculated using MarChemSpec.

The two sets of experiments differ in the magnitude of their rates and the degree of the undersaturation dependence. Near equilibrium, dissolution proceeds faster in "regular" seawater and is depressed in sulfate-free seawater. Around (1-Ω) = 0.3, the rate in both sets of experiments notably increases, but with a steeper slope for the sulfate-free experiments. As a result, far from equilibrium, the dissolution rate in the sulfate-free seawater exceeds the rate in Dickson seawater. Very far from equilibrium, (1-Ω) > ~0.7, the rates of sulfate free seawater are on the same order as the freshwater experiments of Cubillas et al. (2005).

3.4 Model verification of isotopic steady state

In the case of a subset of the Naviaux et al. (2019a) dissolution experiments, it was discovered that the experiments were not run for sufficient duration to reach isotopic steady state. As a result, they either could not predict or required the model to predict the net dissolution rate (Chapter 2). We ran the model for the close to equilibrium sulfate-free experiments to test if these experiments reached isotopic steady state. In **Figure** 4 we show that the model net rate for these experiments agrees with the net rate calculated by the linear regression method. This agreement indicates that the experiments all reached isotopic steady state.

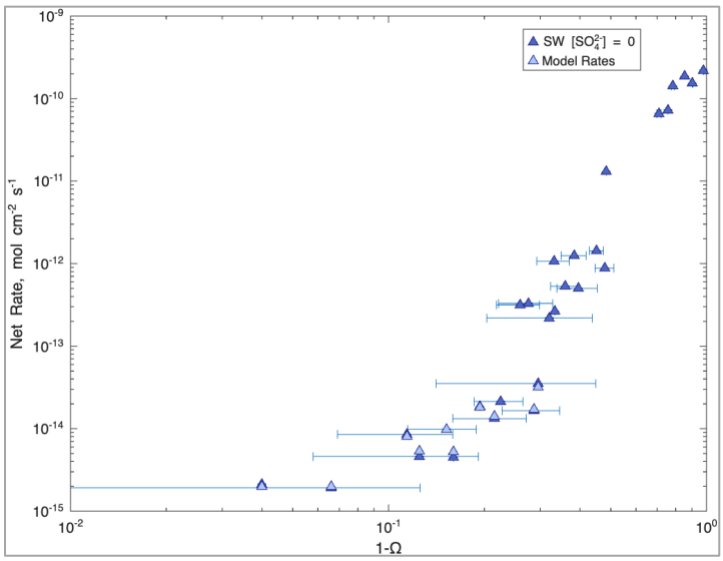


Figure 4. Net dissolution rate comparison between the model approach (light blue) and the regression approach (dark blue). Good agreement indicates that the linear regression approach to calculating net rates was applied after the mineral surface achieved isotopic steady state.

4. Discussion

4.1 Rate law for calcite dissolution in sulfate-free seawater

In chemical oceanography, the calcite dissolution rate law is often expressed as:

Eq 1) $\text{Rate} = k(1-\Omega)^n$

where k is the rate constant (mol/cm^2/s) and n is the reaction order (unitless). Historically, data is fit with a single k and n value, but Naviaux et al. (2019a) found that the nonlinearity of the rate is best captured by three fits to k and n at 21C, an interpretation supported by their mechanistic description of calcite dissolution. They describe a transition in the surface energetic mechanism controlling the dissolution rate at a critical Ω values, Ω_{crit} that corresponds to the breaks in rate law fits (see section 4.2). Limited data density in the very close to equilibrium ranges typically precludes a three-part fit in log-log space, as is the case for the York fits reported by Naviaux et al. (2019a). In fitting our sulfate free data, we identify only one statistically significant break is slope at Ω = 0.75-0.8 (Section 2.4). We report the fits to the k and n values for each segment in **Table 3**.

Following the framework of Naviaux et al. (2019a) the change in slope suggests a change in surface energetic mechanism. The Ω_{crit} we estimate in sulfate-free seawater is roughly the same value observed by Naviaux et al. 2019a, for Dickson seawater, with modern sulfate concentrations. This suggests that although the magnitude of the rates differ, calcite experiences a shift in the mechanism controlling the dissolution rate at the same solution thermodynamic driving force, regardless of the details of the major ion composition of the seawater in which it dissolves.

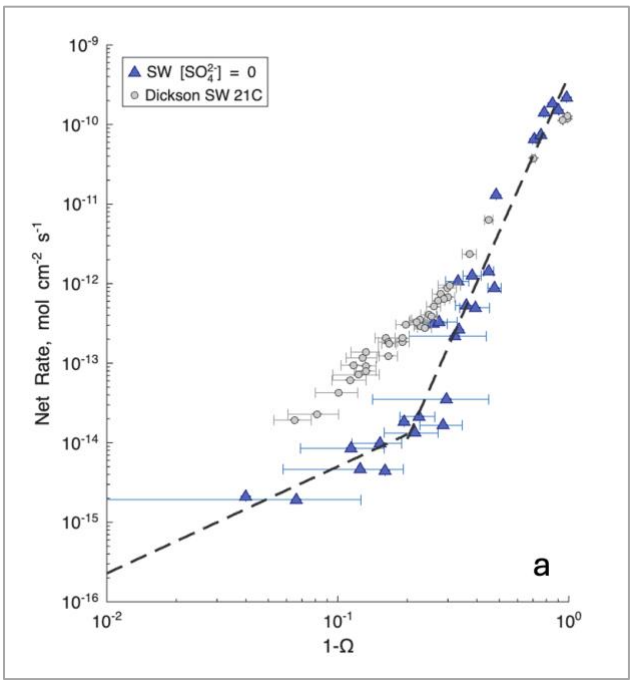


Figure 5. Identification of Ω_{crit} and York fits to data for ASW with $[SO_4^{2-}] = 0$, with Ω values calculated in MarChemSpec. $\Omega_{crit} = 0.8 \pm 0.05$.

This empirical, two-segment description captures the overall nonlinearity in the rate–Ω relationship, but the k and n parameters themselves carry no direct physical meaning. To rigorously interpret the mechanistic origin of the break at Ω_{crit} and to understand why sulfate-free seawater departs from Dickson seawater in both magnitude and slope, we turn to the surface-energetic framework of Dove et al. (2008).

Table 3. York fit parameters for sulfate free experiments, Dickson seawater experiments at 21C determined using MarChemSpec Ω values and with CO2SYS Ω values.

		$\Omega > \Omega_{crit}$		$\Omega < \Omega_{crit}$	
Experiments	**Ω_{crit}**	**$\log_{10}(k)$**	**n**	**$\log_{10}(k)$**	**n**
ASW, $[SO_4^{2-}] = 0$	0.8 ± 0.05	-12.96 ± 0.32	1.34 ± 0.35	-9.38 ± 0.06	6.54 ± 0.17
Dickson Seawater from Naviaux et al. 2019a, MCS Ω	0.779 ± 0.04	-10.95 ± 0.09	2.33 ± 0.11	-9.86 ± 0.04	4.02 ± 0.20
Dickson Seawater from Naviaux et al. 2019a, CO2SYS Ω	0.75	-11.06 ± 0.1	2.15 ± 0.05	-9.82 ± 0.12	4.18 ± 0.07

4.2 Surface energetics during dissolution

In MSW solutions at 21C, three distinct surface energetic mechanisms operate over defined undersaturation ranges. These mechanisms describe changes in the dominant "source" of reactive steps at which dissolution may proceed. At 21C, for Ω > 0.9, dissolution proceeds at existing

steps on the mineral surface (e.g. edges and screw dislocations). As undersaturation increases, in the range of $0.75 < \Omega < 0.9$, dissolution proceeds via the formation of etch pits at defects on the mineral surface. At very high undersaturations, $\Omega < 0.75$, dissolution proceeds by the formation of etch pits homogeneously across the mineral surface.

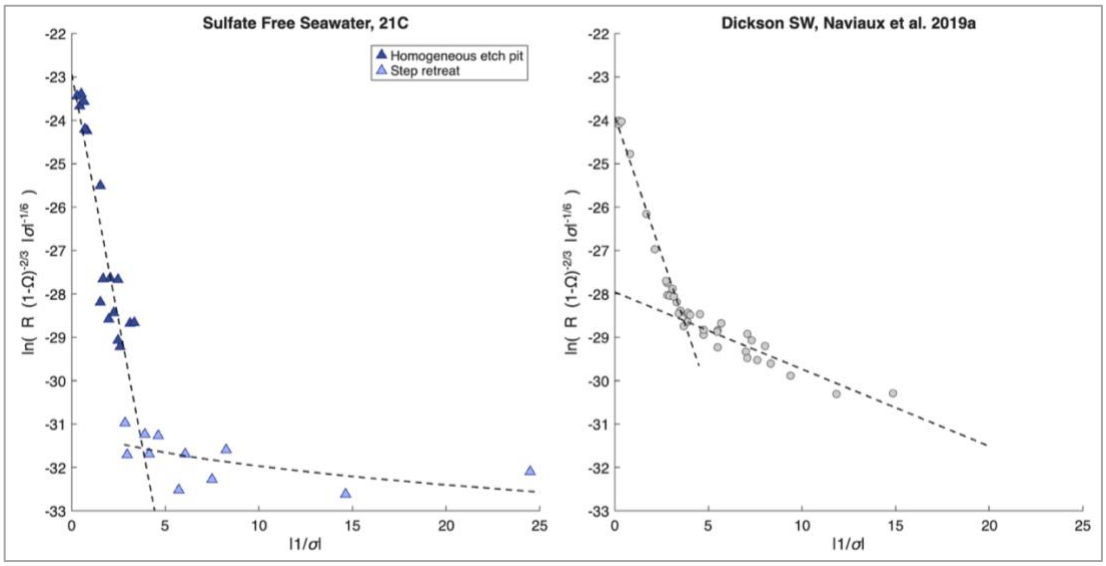


Figure 6. Dissolution rates and undersaturations recast in the Dove framework for (a) sulfate free the light blue triangles are the data used to fit α and β in the step-retreat regime, Equation 5, and the dark blue triangles are fit to the etch pit regime, Equation 4. (b) Dickson seawater experiments, both fit to Equation 4.

These transitions become clear when the dissolution rate and undersaturation are reformulated following the Dove et al (2005) framework, derived from classical crystal growth theory and applied to quartz dissolution rates. We recast Ω as σ, following:

Eq. 2) $\sigma = \ln(\Omega)$

And recast the bulk dissolution in terms of a surface normalized dissolution rate in m/s following:

Eq. 3) Surface normal rate = $\ln\left(\frac{R_D}{(1-\Omega)^{\frac{2}{3}} * |\sigma|^{\frac{1}{6}}}\right)$

For dissolution proceeding via the formation of etch pits, (at lattice defects or homogeneously from flat surfaces), the overall dissolution rate dependence on saturation state is given by:

Eq. 4) $\ln\left(\frac{R_{2D}}{(1-\Omega)^{\frac{2}{3}}\,|\sigma|^{\frac{1}{6}}}\right) = \ln\left(h\beta C_e(\omega^2 h n_s a)^{\frac{1}{3}}\right) - \frac{\pi\alpha^2\omega h}{3(k_b T)^2}\left|\frac{1}{\sigma}\right|$

Where h is the step height (m), β is the step kinetic coefficient (m/2), ω is the molecular volume (m3), n_s is the density of active nucleation sites (sites/m2), a is the lattice spacing (m), α is the step edge free energy (mJ/m2), k_b is Boltzmann's constant, T is the temperature in Kelvin and C_e is the mineral solubility.

Dissolution that proceeds by the retreat of existing steps on the mineral surface (near equilibrium mechanism), follows a different formulation, show as:

Eq. 5) $$\ln\left(\frac{R_{2D}}{(1-\Omega)^{\frac{2}{3}}|\sigma|^{\frac{1}{6}}}\right) = \ln\left(\frac{\omega\beta mh}{P}\right) + ln\left((1-\Omega)^{\frac{1}{3}}\left|\frac{1}{\sigma}\right|^{\frac{1}{6}}\right) - \ln\left(1+8\left(\frac{\omega\alpha}{Pk_bT}\right)\left|\frac{1}{\sigma}\right|\right)$$

Where, *P* is the perimeter of the screw dislocation that is the source of the existing steps and m is the number of elementary steps (equal to 1). The values *h, ω, a, P,* and *m* are all assumed constants, specific to the calcite crystal structure. The terms C_e, T, Ω and sigma are all defined relative to a given experiment. This leaves the fundamental unknowns: β, n_s and α.

When plotted in terms of the surface energetic parameters (i.e. surface normal dissolution rate vs. |1/ σ |), the discontinuities and therefore transitions in mechanisms are clearer than in log-log space (**Figure 6 vs. Figure 7**). Likewise, regressions through the data in Dove space hold mechanistic information in their slope and intersect values. The intercept and slope of each fitted segment in **Figure 6** can be used to solve for the thermodynamic unknowns: β, n_s and α.

Eq. 6) $$Intercept = ln\left(h\beta C_e(\omega^2 h n_s a)^{\frac{1}{3}}\right)$$

Eq. 7) $$Slope = -\frac{\pi\alpha^2\omega h}{3(k_bT)^2}$$

Very far from equilibrium, where dissolution proceeds by homogenous etch pit formation, the data for both sulfate-free and MSW are fit well in Dove space by very steep slopes and large intercepts (**Figure** 7). The intercept of the regression through this data can be used to quantify the step kinetic coefficient in this regime, given the assumptions that (1) β does not vary with Ω within this regime and (2) the nucleation site density value, ns, is ~5 x 10^{12} sites/m^2. The latter assumption comes from direct AFM measurements of homogenous etch pit formation on calcite surfaces in very undersaturated freshwater solutions (Teng, 2004; Ruiz-Agudo et al., 2009). These authors found a maximum ns value of 10^{12} and 10^{13} sites/m^2, respectively. The results of Dong et al. (2020) support this assumption: they calculated the same order of magnitude etch pit densities in this Ω regime in AFM measurements of calcite dissolution in seawater.

Table 4. Summary of calculated surface energetic parameters for sulfate-free seawater (this study, 21ºC), Dickson seawater at 21ºC and 5ºC (from Naviaux et al. 2019a, with Ω values recalculated in MarChemSpec).

	Step Retreat			**Defect Assisted Etch Pit**			**Homogeneous Etch Pit**		
Study	**β, cm/s**	**n_s, 1/m^2**	**α, mJ/m^2**	**β, cm/s**	**n_s, 1/m^2**	**α, mJ/m^2**	**β, cm/s**	**n_s, 1/m^2**	**α, mJ/m^2**
This study, ASW SO4 =0	1.3 10^{-5}	n/a	-0.98	n/a	n/a	n/a	1.36	$5{\cdot}10^{12}$	-44.71

Dickson 21C	Low data	n/a	Low data	0.50	$2.6 \cdot 10^{7}$	-12.43	0.50	$5 \cdot 10^{12}$	-34.41
Dickson 5C	$3 \cdot 10^{-5}$	n/a	-0.50	n/a	n/a	n/a	4	$5 \cdot 10^{12}$	-37.6

The trends in **Figure 6a** for sulfate-free seawater do not unambiguously determine if there are one or two Ω_{crit} values across the saturation range studied. In other words, it is unclear whether the defect assisted etch pit mechanism or the step retreat mechanism or both are operating for $\Omega > \Omega_{crit}$. In Naviaux et al. (2019a) the coldest experiments clearly showed the elimination of the defect-assisted etch pit regime and the same might be true for our new sulfate-free data. We first test the fit of the close to equilibrium data (light blue triangles in **Figure** 6a) to the defect assisted equation (Equation 4). When this equation is used, site density term is calculated to be only ~ 10 sites/cm^2, assuming that β in this regime is the same as in the homogeneous regime. As we use calcite with grain sizes on the order of 100um, an etch pit density of 10 sites/cm^2 means there are effectively no etch pits on the mineral surface.

This leads us to the interpretation that the sulfate-free experiments are operating primarily in the step retreat mode from $\Omega = 1$ to Ω_{crit} and hand off to homogeneous etch pit formation for $\Omega < \Omega_{crit}$. This is supported by the slight upward curvature of the measured date as $|1/\sigma|$ increases, a feature diagnostic of the step retreat mechanism in this numerical formulation (Dove et al. 2005, Naviaux et al. 2019a). Given this interpretation, we can fit the measured sulfate-free data in this regime to β and α in **Equation 5**.

All calculated surface energetic parameters are summarized in **Table 4.** In the homogeneous etch pit regime, where the etch pit density is considered constant across all condition, the step kinetic coefficient, is roughly 3 times larger in sulfate-free seawater than in MSW. The step kinetic coefficient is proportional to the step velocity, meaning the rate at which the etch pits are spreading is much faster when there is no sulfate present in seawater. In this regime, α represents the free energy for the formation of an etch pit. The value of α is 30% larger for sulfate free seawater than for MSW. This means that, for the same solution driving force, it is more difficult to nucleate an etch pit on the surface in sulfate free seawater.

The large value here corresponds to the steep slope of the rate data far from equilibrium and indicates that the sulfate free experiments are more sensitive to the undersaturation in this regime. This difference in slopes between sulfate-free and MSW is the mathematical origin for the change in sign of the rate difference between these two solutions.

Close to equilibrium, there is not sufficient data in the Naviaux et al. (2019a) experiments to calculate the surface energetic parameters. Instead, we can compare our sulfate-free results to the 5ºC experiments where parameters α and β were able to be calculated. In this regime, where dissolution proceeds via the retreat of existing steps on the mineral surface, the β values are many orders of magnitude slower than in the homogeneous regime. The rate of retreat is about 3 times slower in sulfate free seawater compared to 5ºC seawater. The α values here are distinct from those in homogeneous etch pit regime. For step edge retreat, α represents the step edge free energy, or the free energy to remove a unit of calcite from a step. The values for α are on the same order of magnitude between sulfate-free seawater and 5ºC seawater in this regime.

While we don't have a direct comparison to seawater at the same temperate, the similarity of surface energetic parameters in step retreat regime suggests that the mechanism that depresses rates when sulfate is removed from seawater has a similar influence on surface properties a decreasing temperature.

4.3 Calcite surface reactivity with and without sulfate

Thus far, we have not considered the role that sulfate plays on the specific chemical reactions occurring at the mineral surface during dissolution, just the role that sulfate plays in shaping energetic landscape of the surface. By removing the seawater sulfate concentration, we change the chemical speciation of the mineral surface. Using the equilibrium constants reported in surface complexation model studies (Ding and Rahman, 2018; Pokrovsky and Schott, 1999; van Cappellen et al., 1993) we assess how the reactivity of the mineral surface changes as a result of this corresponding change in solution.

The "free" sites on the calcite surface are >CaOH and $>CO_3H$, the hydroxylated calcium site and the protonated carbonates sites. The mineral surface interacts with all other species in solution via these sites. The reactions in Table 5, are all written in terms of the free surface species participating in reaction. This allows direct comparison of the equilibrium constant between the reactions.

One interpretation of the behavior of calcite dissolution in seawater related to speciation of the mineral surface and its changing reactivity as Ω and solution change. Close to equilibrium, where carbonate ion is relatively high, sulfate and carbonate compete for the free calcium sites (Reaction 3 and 7). Based on the equilibrium constants estimated for these surface reactions by Ding and Rhaman (2018), the $>CaCO_3^-$ is much more stable than the $>CaSO_4^-$ site. In regular seawater, these sulfate and carbonate are in competition for the free calcium site, and the overall stability of the mineral surface is based on the relative proportions of each. Even though the sulfate site is less stable, there is orders of magnitude more sulfate in seawater than carbonate, so it can sufficiently compete to occupy the surface. In the absence of sulfate, the free calcium sites are largely speciated with carbonate and the overall stability of the surface increases. This would result in slower dissolution rates than in MSW.

Far from equilibrium the chemical picture of the mineral surface changes. At low Ω there is relatively little carbonate in solution, such that Reactions 2 and 4 are negligible. The competition in this regime between sulfate and the free carbonate site. In all the reactions involving the free calcium site, the forward reaction, of complexing the free site, is thermodynamically favored based on the equilibrium constants in Table 4. The mineral surface is overall more stable when there is more sulfate associated with it. When sulfate is removed, the surface is destabilized and dissolution rate may increase.

Collectively the observations of the change in rate both near and far from equilibrium can be described consistently in the surface speciation framework. An avenue of future work is to apply the new chemical speciation model of seawater, MarChemSpec, to more rigorously quantify the surface chemical speciation in seawater. Quantification of both the proportions of specific surface sites and the concentrations of aqueous species can be used together to define the kinetic descriptions of calcite dissolution following in the vein of Arakaki and Mucci (1995).

It is not immediately clear how the surface energetic parameters map onto the chemical description of the mineral surface. Whether the stability of specific surface sites should be considered in terms of the energy term, α or the kinetic term, β is an avenue for future work.

Table 5. Description of surface binding reactions and their respective binding constants for the surface complexation models of Van Capellen et al. (1993), Pokrovsky and Schott (2002) and Ding and Rhaman (2018).

Reaction Number	Surface Reaction	Van Cappellen et al. (1993) I = 0	Pokrovsky and Schott (2002) I =0	Ding and Rhaman (2018) 0.06<I<1.1
1	$> CaOH + H^+ \Leftrightarrow > CaOH_2^+$	12.2	11.85	11.8
2	$> CaOH + CO_3^{2-} + 2H^+ \Leftrightarrow > CaHCO_3^0 + H_2O$	24.15	23.5	n/a
3	$> CaOH + SO_4^{2-} + H^+ \Leftrightarrow > CaSO_4^- + H_2O$	n/a	n/a	9.7
4	$> CaOH + CO_3^{2-} + H^+ \Leftrightarrow > CaCO_3^- + H_2O$	15.55	17.1	17.8
5	$> CO_3H \Leftrightarrow > CO_3^- + H^+$	-4.9	-5.1	-5.1
6	$> CO_3H + Ca^{2+} \Leftrightarrow > CO_3Ca^+ + H^+$	-2.8	-1.7	-2.25
7	$> CO_3H + Mg^{2+} \Leftrightarrow > CO_3Mg^+ + H^+$	n/a	n/a	-4.42

4.4 Insights from AFM studies

Differences in bulk experiments and AFM measurements, including differences in surface preparation and reactive surface area, make direct comparison between the two challenging. We can more effectively compare across these methods by invoking changes to a system. For example, if altering solution composition shifts surface energetic parameters, how will AFM record a corresponding shift? This approach does not require the two techniques to agree in absolute terms, but lets us test if the same perturbation to each system produce that same result.

With the exception of Dong et al. (2020), AFM studies are generally not performed in seawater. Instead, AFM measurements of surface processes typically performed in freshwater or simple ionic solutions. Likewise, calcite dissolution is typically studied very far from equilibrium. This is partly due to experimental challenges in maintaining a pCO_2 headspace in an AFM fluid cell in order to maintain a constant saturation state. This means that most AFM studies are necessarily limited to probing far from equilibrium regimes of dissolution: defect-assisted etch pit formation and homogeneous etch pit formation.

Given these limitations, we can still draw parallels between our experiments and the AFM measurements by Ruiz-Agudo et al. (2009). They reported the etch pit densities, spreading rates and overall rates in different salts containing sulfate and/or magnesium at very high undersaturations. A subset of their results is reproduced in Table 6. While they don't reproduce the same overall chemical complexity of seawater, they performed experiments with Mg and SO_4^{2-} salts that are on the order of their respective concentrations in seawater. If we consider their ~ 50mM $MgSO_4$ experiments to be the most comparable to seawater, then the $MgCl_2$ experiments can be considered an approximate analogue to our sulfate-free seawater experiments.

Table 6. Subset of the results from the AFM study by Ruiz-Agudo et al. (2019). Calcite was exposed to very undersaturated water with varying concentrations of the following salts. We select the experiments performed ~50mM +/- 5mM for a given salt – the approximate concentration and approaching the IS of seawater.

Salt used in experiment	Etch pit density, $1/m^2$	Etch pit spreading rate, nm/s	Overall AFM rate (logR), $mol/cm^2/s$
NaCl	$1.28 \cdot 10^{12}$	1.95	-11.04
$Na2SO_4$	$2.42 \cdot 10^{12}$	2.98	-11.14
$MgCl_2$	$3.74 \cdot 10^{12}$	1.43	-10.98
$MgSO_4$	$6.38 \cdot 10^{12}$	1.00	-11.53

The overall rate measurements made by Ruiz-Agudo et al. (2009) tell a complicated story in which the calcite dissolution rates change with both changing concentrations of individual salts and with the use of different salts. Overall, the rate of dissolution estimated from AFM measurements show that the rate of dissolution in various salts follows: $MgCl_2$ > NaCl > Na_2SO_4 > $MgSO_4$. Interestingly, the behavior of individual surface measurements (etch pit density and spreading rates) does not necessarily follow this same trend.

They found that more etch pits formed in $MgSO_4$ solutions than $MgCl_2$ solutions and both at greater densities in NaCl and Na_2SO_4 solutions. The etch pit spreading rates were faster in $MgCl_2$ solutions than in $MgSO_4$ solutions, but both were slower than in NaCl and Na_2SO_4. We can compare these to our estimates of surface energetic parameters in the homogeneous etch pit regime. Our β term maps the most cleanly onto their measured etch pit spreading rate. The step kinetic coefficient is related to the overall step velocity following:

Eq. 8) $v = \omega \beta C_e (1- \Omega)$

In extrapolating to $\Omega = 0$, we estimate step velocities in our experiments to be ~21.6 nm/s for sulfate free and 7.9nm/s in regular seawater. These rates are fast relative to typically observed AFM estimates of rates, on the order of 0.5-4 nm/s (R. S. Arvidson et al., 2006; Lea et al., 2001). Some studies have noted faster velocities very far from equilibrium, on the order of 7.9-14.3 nm/s (Vinson and Luttge, 2005), which sit closer to our estimates. While our step velocities are notably faster than those reported in Ruiz-Agudo et al. (2009) but their relative change is consistent for removing sulfate from solution. This agreement is nontrivial: it validates that measurements made from bulk dissolution experiments, when processed through the energetic equation in Section 4.2, contain some of the same information as direct measurements of the mineral surface.

The relative importance of the etch pit density vs. the step retreat parameter can be seen in Equation 4. The overall normalized rate is a function of β to the 1 power and n_s to the 1/3 power. This explains how the overall estimated AFM rate in the Ruiz Agudo study can be larger for $MgCl_2$ relative to $MgSO_4$: the faster step velocity (a first order function of β) matters more than the lower etch pit density.

The Ruiz-Agudo et al. (2009) AFM measurements, made in the homogenous etch pit regime, cannot be used to predict the behavior of the surface near equilibrium. Future work in the vein of the Teng (2004) and Dong et al. (2020) studies, which include AFM measurements over a range

of saturation states, are necessary to test if the surface parameters calculated in Section 4.2 are valid across all undersaturations.

5. Conclusions

The dissolution rate of calcite in sulfate free seawater is faster than MSW far from equilibrium and slower than MSW close to equilibrium. The task of comparing these experiments on the same Ω scale is not trivial. A new chemical speciation model, MarChemSpec, allowed us to account for the effect of changing aqueous sulfate concentrations on Ω. This approach resolves a longstanding limitation in the literature, where the lack of a robust speciation model for altered major-ion seawater made it difficult to disentangle compositional effects from apparent kinetic differences driven by inconsistent Ω calculations.

We found that calcite dissolution in sulfate-free seawater can be described by a rate law with two fits to k and n. A statistically significant break in slope occurs at $\Omega_{crit} \sim 0.8$, comparable to the value reported for Dickson seawater at 21°C (Naviaux et al., 2019a). When considered in the Dove et al. (2005) surface energetic framework, our bulk dissolution rates were used to calculate mechanistic parameters (step kinetic coefficient, β, step edge free energy, α, and nucleation site density, n_s) that describe how dissolution actually proceeds on the mineral surface. This analysis indicates that sulfate-free seawater dissolves via step retreat at existing surface features close to equilibrium ($\Omega > \Omega_{crit}$), and transitions directly to homogeneous etch pit formation far from equilibrium ($\Omega < \Omega_{crit}$), skipping the defect-assisted regime identified in MSW at 21°C. The resulting β and α values allow us to directly compare the energetics of dissolution across solution compositions in a way that the purely empirical York fit cannot.

We find that the behavior in which the sulfate free rate changes sign relative to MSW can be explained by a change in the free energy for nucleating an etch pit, α. This term controls the steepness of the slope in the homogeneous etch pit regime and its larger value for sulfate free seawater indicates that the surface is more sensitive to changing Ω relative to MSW.

This change in sign can also be separately explained by using a chemical description of the mineral surface during dissolution. The reactivity of the mineral surface framed in terms of the stability of specific surface complexes changes as a function of undersaturation and solution composition. Near equilibrium in seawater, calcium sites on the surface form primarily carbonate complexes or less stable sulfate complexes. Removing sulfate from solution increases the proportion of stable carbonate sites and slows the dissolution rate. Far from equilibrium, where carbonate concentrations are low by definition, the calcium sites for sulfate complexes or are free. The free calcium site is unstable relative to the sulfate complexed carbonate site. When sulfate is removed from solution the surface becomes more unstable and dissolves faster.

AFM studies may prove to be useful tools in probing the role of individual species on surface processes. These measurements can validate the surface energetic parameters estimated from the bulk rate measurements. We find evidence from other AFM studies that the change in step velocity between seawater and sulfate seawater parallels the change noted in AFM measured etch pit spreading rates for a seawater-like solution ($MgSO_4$) and a sulfate-free $MgCl_2$ solutions.

Overall, the implications of this work extend beyond the mechanistic description of calcite dissolution kinetics and their modification by specific aqueous species. We note that the fundamental difference in calcite dissolution rates in the absence of sulfate requires wholly different fits to the rate vs. undersaturation relationship. When considering calcite dissolution in

sulfate free environments, the rate law for calcite dissolution in MSW may fundamentally mischaracterize dissolution fluxes.

This matters most where sulfate concentrations vary from modern values. Archean and other early ocean environments, where seawater sulfate is thought to have been orders of magnitude lower than today, are an obvious case. Applying a modern rate law would misrepresent both the absolute rate and undersaturation relationship to the rate. Likewise, in the modern ocean, porewaters and marine particle microenvironments where anoxic condition are prevalent and sulfate reduction operates can locally drive sulfate to low concentrations. In these settings, the sulfate-free rate law and should be considered the appropriate framework.

Chapter 5. Conclusions and future work

The work in this thesis advances in the mechanistic description of calcite dissolution in seawater. I present a model for the dissolution of isotopically labeled calcite in seawater that quantifies gross dissolution, gross precipitation and the size of the reactive surface reservoir on which they operate. The effectively model parses gross fluxes from net rates and serves to both validate the isotope-labeling method and provide mechanistic insights into how gross rates and mineral surface reactivity evolves with undersaturation. The model was subsequently modified and used to calculate the dissolution rates from novel in situ calcite dissolution experiments in marine porewaters. The net dissolution rates we derived from the model showed that sedimentary carbonate dissolution may proceed much faster than predicted from bottom water saturation state. Finally, using sulfate as a probe of seawater speciation, this work demonstrated that dissolution kinetics are sensitive to sulfate concentration in a saturation-state-dependent way, implicating changes in surface stability driven by surface speciation.

These results reinforce the three-regime mechanistic description of calcite dissolution summarized by Adkins et al. (2021): step retreat near equilibrium, defect-assisted etch pit formation at intermediate undersaturation, and homogeneous etch pit nucleation far from equilibrium. This thesis shows that the framework is valid in the laboratory, water column and, as demonstrated here, in marine porewaters. Within this framework, we define an updated formulation for the calcite dissolution rate law:

$$Rate = k_1(1-\Omega)^{n_1} + k_2(1-\Omega)^{n_2} + k_3(1-\Omega)^{n_3}$$

where each pair or k and n corresponds to a distinct mechanism. The single parameterization of traditional rate law cannot capture the rate behavior across the whole range of ocean undersaturations. The suggested reformulation naturally captures the transitions in surface energetic mechanisms that control the rate as a function of undersaturation.

Ocean chemistry models that depend on calcite dissolution require a rate law that is simple and accurate across the full range of oceanic undersaturation. More broadly, models of seafloor carbon and alkalinity cycling should account for the possibility that dissolution kinetics decouple significantly from bottom-water saturation state, a less intuitive but consequential implication of the porewater results in this thesis.

On a mechanistic front, the surface energetic model is effective and internally consistent, but it is far from the only approach used to describe the reactivity of calcite. A non-exhaustive list of these approaches includes: (1) direct surface measurements by AFM or VSI (e.g., Teng, 2004), (2) bulk experiments recast as surface-energetic parameters (Dove et al., 2005; Naviaux et al., 2019), (3) elementary-reaction rate laws built on surface speciation (Arakaki and Mucci, 1995; Van Cappellen et al., 1993), (4) ion-by-ion models describing attachment and detachment fluxes at kink sites (Nielsen et al., 2012, building on DePaolo, 2011) and (5) the contribution of this thesis, the recovery of gross fluxes and reactive surface area from bulk experiments.

In some ways, these seemingly disparate approaches are in communication. The surface-energetic framework of Dove et al. (2005) recovers energetic parameters analogous to those measured in AFM and VSI, but from bulk rate measurements. In both of these approaches, the measurements are of net processes and cannot resolve gross fluxes. The model developed in Chapter 2 addresses this gap by using the isotope labeling method to separate the gross fluxes and reactive surface area.

The gross rates derived from the model in Chapter 2 may provide constraints in the elementary reaction approach described by Arakaki and Mucci (1995). In this approach, the overall rate is a sum of individual elementary reaction and their rate constants.

In the ion-by-ion models of Nielsen et al. (2012) and DePaolo (2011), which describe growth and dissolution as competing attachment and detachment fluxes at kink sites, typically parameterized against isotope measurements, the gross rates recovered here provide a direct empirical constraint on their detachment term. Wolthers et al. (2012) and Mills et al. (2021) have already extended these ion-by-ion models to incorporate surface speciation but the resulting formalism, though mathematically reversible, hasn't been extensively applied to dissolution.

Changing aqueous speciation during dissolution can act as lever for testing how these frameworks relate to one another. In other words, how does a single perturbation manifest in each of the surface-energetic, elementary-reaction, and ion-by-ion models and what can we learn about calcite dissolution kinetics when they are all considered together? Bringing these approaches into contact, using the gross-flux measurements developed here as a common currency between them, is the clearest path toward a unified, predictive theory of calcite reactivity in the ocean.

Bibliography

Aller, R.C., Rude, P.D., 1988. Complete oxidation of solid phase sulfides by manganese and bacteria in anoxic marine sediments. Geochim. Cosmochim. Acta 52, 751–765.

Andersson, M.P., Stipp, S.L.S., 2012. How acidic is water on calcite? J. Phys. Chem. C 116, 18779–18787. https://doi.org/10.1021/jp304671k

Arakaki, T., Mucci, A., 1995. A continuous and mechanistic representation of calcite reaction-controlled kinetics in dilute solutions at 25°C and 1 atm total pressure. Aquat. Geochem. 1, 105–130.

Archer, D., 1991. Modeling the calcite lysocline. J. Geophys. Reserach 96, 17,037-17,050.

Archer, D., Emerson, S., Smith, C., 1989. Direct measurement of the diffusive sublayer at the deep sea floor using oxygen microelectrodes. Nature 340, 623–626.

Archer, D., Kheshgi, H., Maier-Reimer, E., 1998. Dynamics of fossil fuel CO2 neutralization by marine CaCO3. Glob. Biogeochem. Cycles 12, 259–276.

Archer, D., Maier-Reimer, E., 1994. Effect of deep-sea sedimentary calcite preservation on atmospheric CO2 concentration. Nature 367, 260–263.

Archer, D.E., 1996. A data-driven model of the global calcite lysocline. Glob. Biogeochem. Cycles 10, 511–526.

Arndt, S., Jørgensen, B.B., LaRowe, D.E., Middelburg, J.J., Pancost, R.D., Regnier, P., 2013. Quantifying the degradation of organic matter in marine sediments: A review and synthesis. Earth-Sci. Rev. 123, 53–86. https://doi.org/10.1016/j.earscirev.2013.02.008

Arvidson, Rolf S., Collier, M., Davis, K.J., Vinson, M.D., Amonette, J.E., Luttge, A., 2006. Magnesium inhibition of calcite dissolution kinetics. Geochim. Cosmochim. Acta 70, 583–594. https://doi.org/10.1016/j.gca.2005.10.005

Arvidson, R. S., Collier, M., Davis, K.J., Vinson, M.D., Amonette, J.E., Lüttge, A., 2006. Magnesium inhibition of calcite dissolution kinetics. Geochim. Cosmochim. Acta 70, 583–594.

Astilleros, J.M., Fernández-Díaz, L., Putnis, A., 2010a. The role of magnesium in the growth of calcite: An AFM study. Chem. Geol. 271, 52–58. https://doi.org/10.1016/j.chemgeo.2009.12.011

Astilleros, J.M., Fernández-Díaz, L., Putnis, A., 2010b. The role of magnesium in the growth of calcite: An AFM study. Chem. Geol. 271, 52–58. https://doi.org/10.1016/j.chemgeo.2009.12.011

Berelson, W., Hammond, D.E., McManus, J., Kilgore, T.E., 1994. Dissolution kinetics of calcium-carbonate in Equatorial Pacific sediments. Glob. Biogeochem. Cycles 8, 219–235.

Berger, W.H., 2016. Calcite Compensation Depth (CCD), in: Harff, J., Meschede, M., Petersen, S., Thiede, Jö. (Eds.), Encyclopedia of Marine Geosciences, Encyclopedia of Earth Sciences Series. Springer Netherlands, Dordrecht, pp. 71–73. https://doi.org/10.1007/978-94-007-6238-1_47

Berger, W.H., 1967. Foraminiferal Ooze: Solution at depths. Science 156, 383–385.

Boudreau, B.P., 2013. Carbonate dissolution rates at the deep ocean floor. Geophys. Res. Lett. 40, 744–748. https://doi.org/10.1029/2012GL054231

Boudreau, B.P., 2000. The mathematics of early diagenesis: From worms to waves. Rev. Geophys. 38, 389–416. https://doi.org/10.1029/2000RG000081

Boudreau, B.P., Sulpis, O., Mucci, A., 2020. Control of CaCO3 dissolution at the deep seafloor and its consequences. Geochim. Cosmochimca Acta 268, 90–106.

Broecker, W.S., Peng, T.-H., 1987. The role of CaCO3 compensation in the glacial to interglacial CO2 change. Glob. Biogeochem. Cycles 1, 15–29.

Broecker, W.S., Peng, T.-H., 1974. Gas exchange rates between air and sea. Tellus 26, 21–35.

Burton, W.K., Cabrera, N., Frank, F.C., 1951. The Growth of Crystals and the Equilibrium Structure of their Surfaces. Trans. R. Soc. A 243.
Canfield, D.E., Farquhar, J., 2009. Animal evolution, bioturbation, and the sulfate concentration of the oceans. Proc. Natl. Acad. Sci. 106, 8123–8127. https://doi.org/10.1073/pnas.0902037106
Cetiner, J., Berelson, W.B., Rollins, N., Barnhart, H., Liu, S., Byrne, R., Dong, S., Adkins, J., 2022. Novel device to collect deep-sea porewater in situ: A focus on benthic carbonate chemistry. O Methods 21, 82–97.
Cetiner, J., Berelson, W.M., Rollins, N.E., Liu, X., Pavia, F.J., Waldeck, A.R., Gray, William, Dong, S., Fleger, K., Barnhart, H.A., Quinan, M., Wani, R., Rafter, P., Jacobson, A.D., Byrne, R.H., Adkins, J.F., 2025. Carbonate dissolution fluxes in deep-sea sediments as determined from in situ porewater profiles in a transect across the saturation horizon. Geochim. Cosmochim. Acta 390, 145–159.
Chernov, A.A., 1984. Modern Crystallography III: Crystal Growth. Springer Science & Business Media.
Clegg, S.L., Humphreys, M.P., Waters, J.F., Turner, D.R., Dickson, A.G., 2022. Chemical speciation models based upon the Pitzer activity coefficient equations, including the propagation of undertainties. II. Tris buffers in artificial seawater at 25°C, and an assessment of the seawater "Total" pH scale. Mar. Chem. 244, 104096.
Cubillas, P., Kohler, S., Prieto, M., Chairat, C., Oelkers, E.H., 2005. Experimental determination of the dissolution rates of calcite, aragonite, and bivalves. Chem. Geol. 216, 59–77.
Davis, J.A., Fuller, C.C., Cook, A.D., 1987. A model for trace metal sorption processes at the calcite surface: Adsorption of Cd2+ and subsequent solid solution formation. Geochim. Cosmochim. Acta 51, 1477–1490. https://doi.org/10.1016/0016-7037(87)90330-9
DePaolo, D.J., Zhang, S., 2024. Reaction order of near equilibrium calcite dissolution: Uncertainties and ambiguities of isotopic tracer methods. Geochim. Cosmochim. Acta 379, 233–243. https://doi.org/10.1016/j.gca.2024.06.004
Dickson, R.R., Gmitrowicz, E.M., Watson, A.J., 1990. Deep-water renewal in the northern North Atlantic. Nature 344, 848–850.
Ding, H., Rahman, S.R., 2018. Investigation of the Impact of Potential Determining Ions from Surface Complexation Modeling. Energy Fuels 32, 9314–9321.
Dong, S., Berelson, W.M., Adkins, J.F., Rollins, N.E., Naviaux, J.D., Pirbadian, S., El-Naggar, M.Y., Teng, H.H., 2020. An atomic force microscopy study of calcite dissolution in seawater. Geochim. Cosmochim. Acta in review.
Dong, S., Subhas, A.V., Rollins, N.E., Naviaux, J., Adkins, J.F., Berelson, W., 2018. A Kinetic Pressure Effect on Calcite Dissolution in Seawater. Geochim. Cosmochimca Acta 238, 411–423.
Dove, P.M., Han, N., De Yoreo, J.J., 2005. Mechanisms of classical crystal growth theory explain quartz and silicate dissolution behavior. Procedings Natl. Accademy Sci. 102, 10566.
Emerson, S.R., Bender, M.L., 1981. Carbon fluxes at the sediment-water interface of the deep sea: calcium carbonate preservation. J. Mar. Res. 39, 139–162.
F. Millero, 1979. The thermodynamics of the carbonate system in seawater. Geochim Cosmochim Acta 43, 1651–1661.
Fakhraee, M., Crockford, P.W., Bauer, K.W., Pasquier, V., Sugiyama, I., Katsev, S., Raven, M.R., Gomes, M., Philippot, P., Crowe, Sean.A., Tarhan, L.G., Lyons, T.W., Planavsky, N., 2024. The history of Earth's sulfur cycle. Nat. Rev. Earth Environ. 6, 106–125. https://doi.org/10.1038/s43017-024-00615-0
Farver, J.R., 1994. Oxygen self-diffusion in calcite: Dependence on temperature and water fugacity. Earth Planet. Sci. Lett. 121, 575–587. https://doi.org/10.1016/0012-821X(94)90092-2

Farver, J.R., Yund, R.A., 1991. Measurement of oxygen grain boundary diffusion in natural, fine-grained, quartz aggregates. Geochim. Cosmochim. Acta 55, 1597–1607. https://doi.org/10.1016/0016-7037(91)90131-N
Fenter, P., Geissbühler, P., DiMasi, E., Srajer, G., Sorensen, L.B., Sturchio, N.C., 2000. Surface speciation of calcite observed in situ by high-resolution X-ray reflectivity. Geochim. Cosmochim. Acta 64, 1221–1228. https://doi.org/10.1016/S0016-7037(99)00403-2
Fisher, F.H., 1967. Ion Pairing of Magnesium Sulfate in Seawater: Determined by Ultrasonic Absorption. Science 157, 823–823. https://doi.org/10.1126/science.157.3790.823.a
Fisler, D.K., Cygan, R.T., 1999. Diffusion of Ca and Mg in calcite. Am. Mineral. 84, 1392–1399. https://doi.org/10.2138/am-1999-0917
Garrels, R.M., Thompson, M.E., 1962. A chemical model for sea water at 25 degrees C and one atmosphere total pressure. Am. J. Sci. 260, 57–66. https://doi.org/10.2475/ajs.260.1.57
Géhin, A., Gilbert, B., Chakraborty, S., Stack, A.G., Allard, L.F., Robinet, J.-C., Charlet, L., 2021. Long-Term 13C Uptake by 12C-Enriched Calcite. ACS Earth Space Chem. 5, 998–1005. https://doi.org/10.1021/acsearthspacechem.0c00122
Hales, B., Emerson, S.R., 1997. Evidence in support of first-order dissolution kinetics for calcite in seawater. Earth Planet. Sci. Lett. 148, 317–327.
Harrison, A.L., Schott, J., Oelkers, E.H., Maher, K., Mavromatis, V., 2022. Rates of carbon and oxygen isotope exchange between calcite and fluid at chemical equilibrium. Geochim. Cosmochim. Acta 335, 369–382. https://doi.org/10.1016/j.gca.2022.06.041
Honjo, S., Erez, J., 1978. Dissolution rates of calcium carbonate in the deep ocean; an in-situ experiment in the North Atlantic Ocean. Earth Planet. Sci. Lett. 40, 287–300.
Humphreys, M.P., Waters, J.F., Turner, D.R., Dickson, A.G., Clegg, S.L., 2022. Chemical speciation models based upon the Pitzer activity coefficient equations, including the propagation of uncertainties: Artificial seawater from 0 to 45 °C. Mar. Chem. 244, 104095. https://doi.org/10.1016/j.marchem.2022.104095
Jourabchi, P., 2005. Quantitative interpretation of pH distributions in aquatic sediments: A reaction-transport modeling approach. Am. J. Sci. 305, 919–956. https://doi.org/10.2475/ajs.305.9.919
Keir, R.S., 1980. The dissolution kinetics of biogenic calcium carbonates in seawater. Geochim. Cosmochim. Acta 44, 241–252.
Kendall, T.A., Martin, S.T., 2007. Water-Induced Reconstruction that Affects Mobile Ions on the Surface of Calcite. J. Phys. Chem. A 111, 505–514. https://doi.org/10.1021/jp0647129
Kwon, E.Y., Dunne, J.P., Lee, K., 2024. Biological export production controls upper ocean calcium carbonate dissolution and CO_2 buffer capacity. Sci. Adv. 10, eadl0779. https://doi.org/10.1126/sciadv.adl0779
Labotka, T.C., Cole, D.R., Riciputi, L.R., Fayek, M., 2004. Diffusion of C and O in calcite from 0.1 to 200 MPa. Am. Mineral. 89, 799–806. https://doi.org/10.2138/am-2004-5-614
Lasaga, A.C., 1998. Kinetic Theory in the Earth Sciences. Princeton University Press.
Lasaga, A.C., Luttge, A., 2001. Variation of crystal dissolution rate based on a dissolution stepwave model. Science 291, 2400–2404.
Lea, A.S., Amonette, J.E., Baer, D.R., Liang, Y., Colton, N.G., 2001. Microscopic effects of carbonate, manganese, and strontium ions on calcite dissolution. Geochim. Cosmochim. Acta 65, 369–379.
Lee, C., 1992. Controls on organic carbon preservation: The use of stratified water bodies to compare intrinsic rates of decomposition in oxic and anoxic systems. Geochem. Cosmochim. Acta 56, 3323–3335.
Lewis, E., Wallace, D., Allison, L.J., 1998. Program developed for CO{sub 2} system calculations. United States. https://doi.org/10.2172/639712
Malkin, A.I., Chernov, A.A., Alexeev, I.V., 1989. Growth of dipyramidal face of dislocation-free ADP crystals: free energy of steps. J. Cryst. Growth 97, 765–769.

Montenegro, A., Brovkin, V., Eby, M., Archer, D., Weaver, A.J., 2007. Long term fate of anthropogenic carbon. Geophys. Res. Lett. 34, doi:10.1029/2007GL030905.
Morel, F.M.M., Rueter, J.G., Anderson, D.M., Guillard, R.R.L., 1979. AQUIL: A chemically defined phytoplankton culture medium for trace metal studies. J. Phycol. 15, 135–141.
Morse, J.W., 1978. Dissolution kinetics of calcium carbonate in sea water: VI. The near equilibrium dissolution kinetics of calcium carbonate-rich deep sea sediments. Am. J. Sci. 278, 344–353.
Morse, J.W., Berner, R. A., 1972. Dissolution kinetics of calcium carbonate in sea water: II. A Kinetic origin for the lysocline. Am. J. Sci. 272, 840–851.
Mucci, A., 1986. Growth kinetics and composition of magnesian calcite overgrowths precipitated from seawater: Quantitative influence of orthophosphate ions. Geochim. Cosmochim. Acta 50, 2255–2265.
Mucci, A., 1983. The solutbility of calcite and aragonite in seawater at various salinities, temperatures, and one atmosphere total pressure. Am. J. Sci. 283, 780–799.
Naviaux, J.D., Subhas, A.V., Rollins, N.E., Dong, S., Berelson, W., Adkins, J.F., 2019. Temperature Dependence of Calcite Dissolution Kinetics in Seawater. Geochim. Cosmochimca Acta 246, 363–384.
Peterson, M.N.A., 1966. Calcite: rates of dissolution in a vertical profile in the Central Pacific. Science 154, 1542–1544.
Plummer, L.N., Wigley, T.M.L., Parkhurst, D.L., 1978. The kinetics of calcite dissolution in CO2-water systems at 5-60°C and 0.0 to 1.0 atm CO2. Am. J. Sci. 278, 179–216.
Pokrovsky, O.S., Schott, J., 1999. Processes at the magnesium-bearing carbonates/solution interface. II. kinetics and mechanism of magnesite dissolution. Geochim. Cosmochim. Acta 63, 881–897. https://doi.org/10.1016/S0016-7037(99)00013-7
Qiu, X., Yao, Y., Wang, H., Shen, A., Zhang, J., 2019. Halophilic Archaea Mediate the Formation of Proto-Dolomite in Solutions With Various Sulfate Concentrations and Salinities. Front. Microbiol. 10, 480. https://doi.org/10.3389/fmicb.2019.00480
Riley, J.P., Tongudai, M., 1967. The major cation/chlorinity ratios in sea water. Chem. Geol. 2, 263–269. https://doi.org/10.1016/0009-2541(67)90026-5
Rivers, J.M., 2023. Warm acidified seawater: a dolomite solution. J. Sediment. Res. 93, 187–201. https://doi.org/10.2110/jsr.2022.087
Ruiz-Agudo, E., Kowacz, M., Putnis, C.V., Putnis, A., 2010. The role of background electrolytes on the kinetics and mechanism of calcite dissolution. Geochim. Cosmochimca Acta 74, 1256–1267.
Santschi, P., Anderson, Robert F., Fleisher, M.Q., Bowles, Walter, 1991. Measurements of diffusive sublayer thickness in the ocean by alabaster dissolution, and their implications for the measurements of benthic fluxes. J. Geophys. Reaserch 96, 10,641-10,657.
Shiraki, R., Rock, P.A., Casey, W.H., 2000. Dissolution kinetics of calcite in 0.1 M NaCl solution at room temperature: an atomic force microscopic (AFM) study. Aquat. Geochem. 6, 87–108.
Siebert, R.M., Hostetler, P.B., 1977. The stability of the magnesium carbonate ion pair from 10 degrees to 90 degrees C. Am. J. Sci. 277, 716–734. https://doi.org/10.2475/ajs.277.6.716
Sjoberg, E.L., 1978. Kinetics and mechanism of calcite dissolution in aqueous solutions at low temperatures, in: Stockholm Contributions in Geology. pp. 1–96.
Steefel, C.I., Van Cappellen, P., 1990. A new kinetic approach to modeling water-rock interaction: The role of nucleation, precursors, and Ostwald ripening. Geochim. Cosmochim. Acta 54, 2657–2677.
Stipp, S.L.S., 1998. Surface analytical techniques applied to calcite: evidence of solid-state diffusion and implications for isotope methods. Palaeogeogr. Palaeoclimatol. Palaeoecol. 140, 441–457. https://doi.org/10.1016/S0031-0182(98)00030-3

Subhas, A.V., Adkins, J.F., Rollins, N.E., Naviaux, J., Erez, J., Berelson, W.M., 2017. Catalysis and chemical mechanisms of calcite dissolution in seawater. Procedings Natl. Accademy Sci. 114, 8175–8180.

Subhas, A.V., Dong, S., Naviaux, J.D., Rollins, N.E., Ziveri, P., Gray, W., Rae, J.W.B., Liu, X., Byrne, R.H., Chen, S., Moore, C., Martell-Bonet, L., Steiner, Z., Antler, G., Hu, H., Lunstrum, A., Hou, Y., Kemnitz, N., Stutsman, J., Pallacks, S., Dugenne, M., Quay, P.D., Berelson, W.M., Adkins, J.F., 2022. Shallow Calcium Carbonate Cycling in the North Pacific Ocean. Glob. Biogeochem. Cycles 36, e2022GB007388. https://doi.org/10.1029/2022GB007388

Subhas, A.V., Rollins, N.E., Berelson, W., Dong, S., Erez, J., Adkins, J.F., 2015. A novel determination of calcite dissoluiton kinetics in seawater. Geochim. Cosmochim. Acta 170, 51–68.

Sulpis, O., Lix, C., Mucci, A., Boudreau, B.P., 2017. Calcite dissolution kinetics at the sediment-water interface in natural seawater. Mar. Chem. 195, 70–83.

Teng, H.H., 2004. Controls by saturation state on etch pit formation during calcite dissolution. Geochim. Cosmochimca Acta 68, 253–262.

van Cappellen, P., Charlet, L., Stumm, W., Wersin, P., 1993. A surface complexation model of the carbonate mineral-aqueous solution interface. Geochim. Cosmochimca Acta 57, 3505–3518.

Vinson, M.D., Luttge, A., 2005. Multiple length-scale kinetics: an integrated study of calcite dissolution rates and strontium inhibition. Am. J. Sci. 305, 119–146.

Walter, L.M., Morse, J.W., 1985. The dissolution kinetics of shallow marine carbonates in seawater: A laboratory study. Geochim. Cosmochimca Acta 49, 1503–1513.

Wolthers, M., Charlet, L., Cappellen, P.V., 2008. The surface chemistry of divalent metal carbonate minerals; a critical assessment of surface charge and potential data using the charge distribution multi-site ion complexation model. Am. J. Sci. 308. https://doi.org/10.2475/08.2008.02

Zeebe, R.E., Zachos, J.C., 2013. Long-term legacy of massive carbon input to the Earth system: Anthropocene versus Eocene. Philos. Trans. R. Soc. Math. Phys. Eng. Sci. 371, 20120006. https://doi.org/10.1098/rsta.2012.0006

Zhang, J., Nancollas, G., 1998. Kink Density and Rate of Step Movement during Growth and Dissolution of an AB Crystal in a Nonstoichiometric Solution. J. Colloid Interface Sci. 200, 131–145.

Zhang, J., Nancollas, G.H., 1990. Kink densities along a crystal surface step at low temperatures and under nonequilibrium conditions. J. Cryst. Growth 106, 181–190.

Ziveri, P., Gray, W.R., Anglada-Ortiz, G., Manno, C., Grelaud, M., Incarbona, A., Rae, J.W.B., Subhas, A.V., Pallacks, S., White, A., Adkins, J.F., Berelson, W., 2023. Pelagic calcium carbonate production and shallow dissolution in the North Pacific Ocean. Nat. Commun. 14, 805. https://doi.org/10.1038/s41467-023-36177-w